University of Alberta

Synthesis and Application of Iron-containing Nanoparticles

by

Janet Elizabeth Macdonald ©

A thesis submitted to the Faculty of Graduate Studies and Research in partial fulfillment
of the requirements for the degree of

Doctor of Philosophy

Department of Chemistry

Edmonton, Alberta
Fall 2008

Library and
Archives Canada

Published Heritage
Branch

395 Wellington Street
Ottawa ON K1A 0N4
Canada

Bibliothèque et
Archives Canada

Direction du
Patrimoine de l'édition

395, rue Wellington
Ottawa ON K1A 0N4
Canada

Your file Votre référence
ISBN: 978-0-494-46371-0
Our file Notre référence
ISBN: 978-0-494-46371-0

NOTICE:
The author has granted a non-exclusive license allowing Library and Archives Canada to reproduce, publish, archive, preserve, conserve, communicate to the public by telecommunication or on the Internet, loan, distribute and sell theses worldwide, for commercial or non-commercial purposes, in microform, paper, electronic and/or any other formats.

The author retains copyright ownership and moral rights in this thesis. Neither the thesis nor substantial extracts from it may be printed or otherwise reproduced without the author's permission.

AVIS:
L'auteur a accordé une licence non exclusive permettant à la Bibliothèque et Archives Canada de reproduire, publier, archiver, sauvegarder, conserver, transmettre au public par télécommunication ou par l'Internet, prêter, distribuer et vendre des thèses partout dans le monde, à des fins commerciales ou autres, sur support microforme, papier, électronique et/ou autres formats.

L'auteur conserve la propriété du droit d'auteur et des droits moraux qui protège cette thèse. Ni la thèse ni des extraits substantiels de celle-ci ne doivent être imprimés ou autrement reproduits sans son autorisation.

In compliance with the Canadian Privacy Act some supporting forms may have been removed from this thesis.

While these forms may be included in the document page count, their removal does not represent any loss of content from the thesis.

Conformément à la loi canadienne sur la protection de la vie privée, quelques formulaires secondaires ont été enlevés de cette thèse.

Bien que ces formulaires aient inclus dans la pagination, il n'y aura aucun contenu manquant.

Canada

Abstract

The synthesis and application of iron containing nanoparticles were studied with three major research foci.

The synthesis of FeTi intermetallic nanoparticles was attempted by reduction of iron(III) and titanium(IV) chlorides and the thermal decomposition of $Fe(CO)_5$ and $Cp_2Ti(CO)_2$. These syntheses were unsuccessful often producing phase segregated iron and titanium materials instead of the desired intermetallic nanoparticles. The phase mismatch between the individual metals is indicated as a potential key factor which inhibits epitaxial growth and the formation of nanoparticles.

The size control of iron and iron oxide nanoparticles was studied for the decomposition of $Fe(CO)_5$ with the particular interest of achieving particle diameters below 4 nm. Surfactant choice alone was found to be inadequate for achieving such sizes as the surfactant inhibits particle growth but also prevents particle nucleation. Trace water in reaction mixtures was found to influence particle size by promotion the decomposition of $Fe(CO)_5$ through water-gas-shift chemistry. Particle size was varied from 2.2 nm to 5.6 nm by changing the water concentration. Hot introduction of reagents and sonication techniques were also explored and found to be effective for achieving particles of sizes below 4 nm. These techniques were limited by safety concerns, irreproducibility and/or low yields.

Iron oxide-capped iron nanoparticles ($Fe@Fe_xO_y$) can be used to sequester trace catalytic metals from reaction products in aqueous and polar organic solvents. When strongly coordinating ligands are not present, the mechanisms of remediation are both the coordination of metal ions and also the reduction of metals onto particle surfaces by the iron metal core. A trend between electrochemical potential remediation capacity was observed; metal ions with much higher electrochemical potentials than that of iron are sequestered more effectively. The presence of coordinating phosphines hinders straightforward sequestration of catalytic metals by Fe@Fe_xO_y. Sequestration can be efficient when it is performed in the presence of 3-mercaptopropionic acid. Under these situations, sequestration is dominated by the adsorption mechanism rather than the reduction. These techniques were successfully applied to synthetically important reactions with catalysts of Ni, Cu, Pd, Rh and Ru.

Table of Contents

Chapter 1: Introduction 1

1.1 A brief introduction to iron and the iron oxides 2

1.2 The lure of the nano size regime and the science of small 4

1.3 Particle synthesis and nucleation and growth theories 6

1.4 Transmission Electron Microscopy (TEM) 13

1.5 X-Ray Photoelectron Spectroscopy (XPS) 18

1.6 Scope of the thesis 22

1.7 References 24

Chapter 2: The Synthesis of FeTi intermetallic nanoparticles 27

3.1 Introduction 27

3.2 Experimental Procedures 30

3.3 Results and Discussion 34

3.4 Conclusions 43

3.5 References 44

Chapter 3: Size control of iron and iron oxide nanoparticles from the decomposition of $Fe(CO)_5$ 46

3.1 Introduction 46

3.2 Experimental Procedures 50

3.3 Results and Discussion 57

3.4 Conclusions 80

3.5 References 82

Chapter 4: Iron/Iron oxide nanoparticle sequestration of catalytic metal impurities from aqueous media and organic reaction products 85
4.1 Introduction 85
4.2 Experimental Procedures 86
4.3 Results and Discussion 92
4.4 Conclusions 97
4.5 References 98

Chapter 5: Removal of residual metal catalysts with iron/iron oxide nanoparticles from coordinating environments 99
5.1 Introduction 99
5.2 Experimental Procedures 101
5.3 Results and Discussion 109
5.4 Conclusions 132
5.5 References 134

Chapter 6: Conclusions and Future Work 137
6.1 Preparation of FeTi nanoparticles 137
6.2 Size control of iron and iron oxide nanopartilces 139
6.3 The use of iron oxide capped iron nanoparticles for the removal of catalytic metals 140
6.4 Answering questions and discovering more questions 141
6.5 References 145

Appendices 146
Appendix A: EDS spectra 146
Appendix B: Promotion of decomposition by water- Statistical analysis 150
Appendix C: XPS of Fe@Fe_xO_y after sequestration 153
Appendix D: Small molecule additive screening experiments 162
for metal sequestration using Fe@Fe_xO_y 161

List of Tables

Table 4-1 Sequestration of metal ions from basic aqueous solutions using $Fe@Fe_xO_y$. 95

Table 5-1 Sequestration of metal ions from non-coordinating environments 113

Table 5-2 Sequestration of 40-150 ppm solutions of metal-phosphine catalysts using $Fe@Fe_xO_y$ and aided by small molecules 117

Table 5-3 Percent removal of phosphine-coordinated metals using common filtering agents and small molecule additives 119

Table 5-4 Effect of pH on percent removal of phosphine-coordinated metals using $Fe@Fe_xO_y$ and small molecule additives. 120

Table App. B-1: Statistical analysis of particle diameter. 151

Table App. B-2: Analysis between concentration groups 152

Table App. D- 1: Qualitative tests into the sequestration of phosphine inhibited metals by $Fe@Fe_xO_y$ 162

Table App. D-2: The effect of amino acids and trithiocyanuric acid (TUA) on sequestration 163

Table App. D-3: A closer look at the additive cysteine and the roles of functional groups 164

Table App. D-4: The roles of pH and functional groups 165

Table App. D-5: The role of base and functional groups with Rh and Ru catalysts 166

Table App. D-6: Sequestration with filtering agents 167

List of Figures

Figure 1-1 Crystal structures of a) magnetite and b) maghemite 3

Figure 1-2 A general and ideal solution synthesis for the formation of iron particles. 7

Figure 1-3 Classical nucleation theory description of the dependence of the thermodynamic barrier for nucleation with respect to radius. 9

Figure 1-4 The LaMer model for burst nucleation. 11

Figure 1-5 Schematic of the optics of a Transmission Electron Microscope. 14

Figure 1-6 The origin of characteristic K_α and K_β X-rays for iron in the electron microscope which are collected for EDS. 17

Figure 1-7 An example high resolution XPS of a Ni containing sample. 19

Figure 1-8 Source of XPS multiplet splitting in Ni(0). 21

Figure 2-1 The binary phase diagram for iron and titanium. 29

Figure 2-2 Relevant crystallographic structures a) hexagonally close packed b) body centred cubic c) CsCl 29

Figure 2-3 a) Representative TEM of the product of a co-reduction of iron(III) and titanium(IV) chlorides b) Example SAED of the product indexed to reflections characteristic of KCl. 37

Figure 2-4 a) TEM of particles isolated from the high temperature reduction of iron and titanium chlorides 38

Figure 2-5 a) TEM of the material formed from the thermal decomposition of $Fe(CO)_5$ and $Cp_2Ti(CO)_2$ 39

Figure 2-6 a) TEM of materials formed by the thermal decomposition of $Fe(CO)_5$ in the presence of titanium clusters 40

Figure 3-1 Example heating curve of sand bath. 53

Figure 3-2 Iron oxide nanoparticles from the thermal decomposition of $Fe(CO)_5$ in benzyl ether and a) no surfactant b) oleic acid c) oleyl amine 59

Figure 3-3 Representative Selected Area Electron Diffraction (SAED) of particles showing characteristic reflections of γ-Fe_2O_3. 59

Figure 3-4 Particles formed from the decomposition of $Fe(CO)_5$ in the presence of TOPO 60

Figure 3-5 Particles from the decomposition of $Fe(CO)_5$ in the presence of a) oleic acid and triethylamine b) *N*-lauroyl aspartic acid 62

Figure 3-6 Brightfield TEM images of iron oxide nanoparticles synthesized from the thermal decomposition of $Fe(CO)_5$ in benzyl ether and oleic acid a) 101 ppm H_2O b) 181 ppm H_2O c) 657 ppm H_2O d) 1590 ppm H_2O 66

Figure 3-7 The affect of water concentration on the average particle size diameter in the thermal decomposition of $Fe(CO)_5$ to give iron oxide nanoparticles 66

Figure 3-8 Log-log plot of water concentration and particle size giving a linear trend with the equation $\log d = -0.30\log[H_2O] + 1.3$ $R^2 = 0.8013$. 68

Figure 3-9 FT-IR of the gas released from the thermal decomposition of $Fe(CO)_5$ in benzyl ether and oleic acid. Peaks indicative of $Fe(CO)_5$ are off scale to allow for visualization of the other components. 70

Figure 3-10 Particles achieved by introduction of liquid phase $Fe(CO)_5$ into octyl ether and a) and b) 1.5 eq oleyl amine at ~290°C c) 4 eq oleyl amine at 200°C. 73

Figure 3-11 Iron oxide particle achieved from the bubbling of gaseous $Fe(CO)_5$ into hot solvents and surfactants a) octly ether at 286°C b) TOPO at 280°C c) TOPO at 280°C, cooled, reheated and introduction restarted 74

Figure 3-12 Sonochemical decomposition of $Fe(CO)_5$ in a) benzyl ether and oleic acid b) neat oleic acid c) benzyl ether and oleyl amine 77

Figure 3-13 Sonochemical decomposition of $Fe(CO)_5$ in TOPO for a) 20s b) and c) 2.5 min 78

Figure 4-1 Brightfield TEM image of $Fe@Fe_xO_y$, bar = 200 nm. Inset: SAED showing characteristic reflections indexed to Fe_3O_4 94

Figure 5-1 High resolution XPS of metals on $Fe@Fe_xO_y$ after being sequestered. Sequestration was of simple metal salts from aqueous solution. 112

Figure 5-2 a) XPS Ni 2p region of Fe@Fe$_x$O$_y$ after sequestering nickel leached from a hydrogenation over Raney nickel. b) XPS Cu 2p region of Fe@Fe$_x$O$_y$ after sequestering copper from a "click" cycloaddition. 115

Figure 5-3 Representative XPS Fe 2p region of Fe@Fe$_x$O$_y$ a) before sequestration (with 0 oxidation fitting highlighted in red) and b) after sequestration. 125

Figure 5-4 Representative XPS O 1s region of Fe@Fe$_x$O$_y$ following sequestration of catalytic metals aided by a) 3-mercaptopropionic acid and b) cysteamine. The sum of the fittings are highlighted in blue. 126

Figure 5-5 Representative XPS N 1s region of Fe@Fe$_x$O$_y$ following sequestration of catalytic metals aided by cysteamine at a) near neutral conditions b) 1 equivalent added KOH. The sum of the fittings are highlighted in blue. 128

Figure 5-6 Representative XPS S 2p region of Fe@Fe$_x$O$_y$ following sequestration of catalytic metals aided by a) 3-mercaptopropionic acid and b) cysteamine. Spin-orbit couples are fitted and indicated by matching colour. Sums of the fittings are highlighted in blue. 129

Figure 5-7 Example XPS Rh 3d region of Fe@Fe$_x$O$_y$ after sequestration of Wilkinson's Catalyst aided by small thiol containing molecules a) by sonication b) by stirring. The sum of the fittingsa are in blue and the 0 oxidation sate fitting in a) is highlighted in red. 131

Figure 5-8 Example XPS Pd 3d region of Fe@Fe$_x$O$_y$ after sequestration of Pd(PPh$_3$)$_4$ catalyst aided by small thiol containing molecules. The sum of the fittings are highlighted in blue. 131

Figure App. A-1: Example EDS spectrum of a reduction of iron(III) and titanium(IV) chlorides* 146

Figure App. A-2: Example EDS spectrum of a reduction of iron(III) and titanium(IV) chlorides 146

Figure App. A-3: EDS spectrum of particles resultant from the high temperature reduction of iron(III) and titanium(IV) chlorides 147

Figure App. A-4: EDS spectrum of amorphous material from the thermal decomposition of Fe(CO)$_5$ and Cp$_2$Ti(CO)$_2$ 148

Figure App. A-5: EDS spectrum of cube-like structures resultant from the thermal decomposition of Fe(CO)$_5$ and Cp$_2$Ti(CO)$_2$ 148

Figure App. A-6: EDS spectrum of material resultant from the decomposition of $Fe(CO)_5$ in the presence of Ti clusters (formed *in situ*) 149

Size distribution of oleic acid capped particles 150

Size distribution of oleyl amine capped particles 150

Size distributions of TOPO capped particles 150

XPS $Fe@Fe_xO_y$ - Co 153

XPS $Fe@Fe_xO_y$ - Ni 154

XPS $Fe@Fe_xO_y$ - Cu 155

XPS $Fe@Fe_xO_y$ - Ru 156

XPS $Fe@Fe_xO_y$ - Rh 157

XPS $Fe@Fe_xO_y$ - Pd 158

XPS $Fe@Fe_xO_y$ - Pt 159

XPS $Fe@Fe_xO_y$ - Ag 160

List of Schemes

Scheme 3-1 Surfactants employed for study of size controlled synthesis of iron/iron oxide nanoparticles: oleic acid, oleylamine, and trioctylphosphine oxide (TOPO) 58

Scheme 3-2 Synthesis of *N*-lauroylaspartic acid 62

Scheme 4-1 Application of $Fe@Fe_xO_y$ sequestering to a "Click" copper catalyzed cycloaddition. Copper concentrations are provided in ppm of the organic product. 96

Scheme 4-2 Application of $Fe@Fe_xO_y$ sequestering to a Pd catalyzed Heck coupling. Pd concentrations are provided in ppm of the organic product. 96

Scheme 5-1 Hydrogenation of cinnamic acid over Raney nickel followed by the sequestration of leached nickel by $Fe@Fe_xO_y$ 115

Scheme 5-2 Small molecule additives screened for aiding $Fe@Fe_xO_y$ sequestration of phosphine containing metal catalysts 117

Scheme 5-3 Phosphine-Metal catalyst sequestration by $Fe@Fe_xO_y$ and 3-mercaptopropionic acid or cysteamine 122

Scheme 5-4 Application of $Fe@Fe_xO_y$ to the sequestration of Pd from Suzuki couplings. 124

List of Abbreviations

acac	acetylacetonate
ANOVA	analysis of variation
aq	aqueous
ASP	aspartic acid
atm	atmosphere
a.u.	arbitrary units
bcc	body centred cubic
bp.	boiling point
Bu	butyl
^{o}C	degree Celsius
CCD	charge coupled device
cm	centimetre
cm^{-1}	inverse centimeter
CNT	carbon nanotube
COD	cyclooctadiene
Cp	cyclopentadienyl
Cy	cyclohexyl
CYA	cysteamine
CYS	cysteine
d	doublet
d	(average) diameter
D	deuterium
δ	chemical shift (in units of ppm)
dba	dibenzylideneacetone
DME	dimethoxyethane

DMF	dimethylformamide
DMSO	dimethylsulfoxide
E	electrochemical potential
E^{o}	standard electrochemical potential
EDS	energy dispersive spectroscopy
EDTA	ethylenediaminetetraaceticacid
eq	equivalent
Et	ethyl
eV	electronVolt
$\mathrm{Fe@Fe_xO_y}$	core-shell iron oxide capped iron nanoparticles
FT-IR	Fourier transform- infrared spectroscopy
g	gram
G	Gibbs free energy
h	hour
IR	infrared (spectrocscopy)
fcc	face centred cubic
GC-MS	gas chromatography- mass spectroscopy
GLY	glycine
hcp	hexagonal close packed
ICP-MS	inductively coupled plasma- mass spectroscopy
λ	wavelength
L	ligand
LYS	lysine
MEA	3-mercaptopropionic acid
m	mass
m	metre
m	multiplet
M	molar
M	metal atom (general)
mg	milligram
MHz	megaHertz

min	minute
mL	mililitre
mm	milimitre
mM	milimolar
mmol	milimole
mol	mole
MΩ·cm	mega-Ohms-centimetre
mp	melting point
MRI	magnetic resonance imaging
MW-CNT	multiwalled- carbon nanotubes
m/z	mass to charge ratio
n	integer number (of something)
n	number of measurements
nm	nanometre
NMR	nuclear magnetic resonance
OAc	acetate
Pa	Pascal
Ph	phenyl
ppb	parts per billion
ppm	parts per million
PTFE	polytetrafluoroethylene
q	quartet
Quad-ICP-MS	quadrupole-inductively coupled plasma- mass spectroscopy
r	radius
R	alkyl
s	second
s	singlet
SAED	selected area electron diffraction
SW-CNT	single walled- carbon nanotubes
t	triplet
TEM	transmission electron microscope/microscopy

THF	tetrahydrofuran
TOPO	trioctylphospineoxide
TUA	trithiocyanuric acid
μL	microlitre
μm	micrometre
W	Watt
XANES	X-ray absorption near edge spectroscopy
x	integer number (of something)
x	number (general)
XPS	X-ray photoelectron spectroscopy
y	number (general)
z	charge
Z	nuclear charge

Chapter 1: Introduction

Since the birth of the iron age nearly four thousand years ago, humans have been smelting and hammering iron metal into useful products.[1] Nature has been harnessing the properties of iron oxides even longer. Pigeons and honey bees biosynthesize magnetic iron oxide particles to aid navigation.[2] The understanding of the chemical properties of iron metal and iron oxides has come much later. The alchemists of the middle ages learned much of the reactivity of iron,[3] but their interpretations of the experimental results were dubious by modern scientific standards. The study of the reactivity of iron in a modern context perhaps did not start in earnest until the latter half of the 19th century and has intensified in application in the 20th century.[4-7]

Iron-containing nanoparticles and colloids, although present in the environment[2, 8] and having long been used as catalysts,[9] have undergone extensive exploratory development in the last three decades. Research of the 1980s and early 1990s focused on the magnetic properties of "ultra-fine" powders[10-14] whereas the "nano-revolution" of the 1990s saw pioneering development of size controlled solution syntheses[10, 15, 16] which opened new avenues for research. Despite humanity's millennia of experience with manipulating iron,[1] our chemical knowledge of iron-containing nanoparticles is still relatively uninformed. This thesis will tackle aspects of three under-explored and intriguing areas:

1. How does one control the composition of particles?

2. What controls the of size of particles?

3. What are the chemical properties of the particles and how can they be exploited?

In Chapter 2, attempts are made to push the nanoparticle synthetic boundaries and prepare FeTi alloy particles for the ultimate goal of hydrogen storage application. Chapter 3 is a discussion of experiments with the aim of achieving very small iron oxide particles below 4 nm in diameter. This research pushes the understanding of the growth and nucleation processes and how they affect particle size in this system. From there, in Chapters 4 and 5, the chemical properties of iron particles are applied to problems in other fields of chemistry. High surface area iron materials and the electrochemical reduction potential of iron are exploited for the sequestration of late transition metals from reaction media.

Within the underlying theme of iron-containing nanoparticles, the chapters within this thesis are quite varied in focus. Therefore, instead of a comprehensive literature review to the different topics (which will be provided in the individual chapters), this introduction will provide a preamble to studying iron, nanoparticles, and brief descriptions of some of the characterization techniques used throughout this research.

1.1 A brief introduction to iron and the relevant oxides

The chemistry of iron is quite rich as a result of several readily accessible oxidation states, the most common being 0, II, and III. More obscure oxidation states have been observed,[17] the most prevalent case being the formal Fe(V) seen in the active sites of Cytochrome P450 enzymes which act as powerful biological oxidants.[18] In iron oxides, the oxidation states commonly observed are II and III.[19]

The most common form of metallic iron, α-Fe, exhibits a body centered cubic crystal structure. At higher temperatures, a face centered cubic phase has also been identified.[20] There are many oxides and oxide-hydroxides of iron – both synthetic and naturally forming;[19] however, within this research only crystalline maghemite, γ-Fe_2O_3 and/or magnetite, Fe_3O_4 were identified. These two oxides have very similar inverse-spinel structures, with 32 O^{2-} anions cubic close packed in the unit cell. This provides tetrahedral and octahedral coordination sites for the iron cations. In magnetite, Fe^{2+} cations occupy tetrahedral sites and Fe^{3+} cations can be found in both octahedral and tetrahedral sites (Figure 1-1a). Maghemite has only Fe^{3+} cations which are found in both octahedral and tetrahedral coordination. Additional cation vacancies accommodate for this oxidation (Figure 1-1b).[19] Because of this structural similarity, the two X-ray diffraction patterns are nearly identical[21] and should not be used alone for routine discrimination of the two oxides. Raman spectroscopy[22] or X-ray photoelectron spectroscopy[23, 24] can be used as additional characterization to identify which oxide is present.

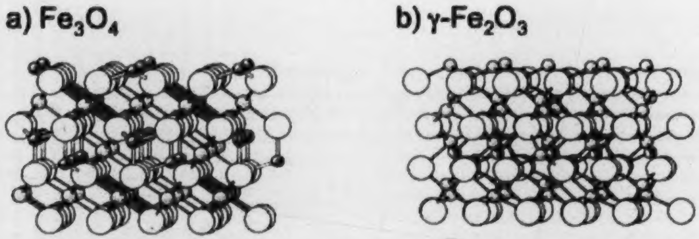

Figure 1-1 Crystal structures of a) magnetite and b) maghemite. [25]

In iron metal and the iron oxides, the 0, II and III oxidation states are paramagnetic, as a result of unpaired electrons within the d shell. α-Fe is quintessentially ferromagnetic; the nuclear spins align in the same direction to give an overall magnetic moment.[26] However, in other materials alternating alignment of the nuclear spins at the crystallographic level can cause a cancellation of the overall magnetic moment. Both maghemite and magnetite are ferrimagnetic in which there is some alternating alignment of the nuclear spins but they do not completely cancel, resulting in an overall non-zero net magnetic moment. [8]

Since magnetic properties are not a major focus of this report, in the context of this research, it suffices to note that the iron and iron oxide particles synthesized here are attracted to external magnetic fields from sources such as magnetic stir bars and each other. This property also makes them amenable to magnetic filtration for possible application.

1.2 The lure of the nano size regime and the science of small

Materials with dimensions confined to the nano-size regime (< 100 nm) can have fascinating size-dependant characteristics such as opto-electronic,[27] magnetic,[28] biological,[29, 30] physical,[31] and chemical properties.[32] This report directly and indirectly focuses on the latter two.

Many chemical reactions occur at the surfaces of particles. As particle size decreases, the surface area to volume ratio increases in an inverse relationship with radius. Consequently, smaller particles have a greater proportion of their atoms on their surfaces. For example, a 20 nm iron particle has fewer than 10% of its atoms at the surface, yet a 3 nm particle has more than 50%.[33] At this size, surface-catalyzed reactions are faster and stoichiometric reactions become atom economic.[32]

There are other, more subtle, size-dependent changes in chemical reactivity. If a reaction occurs at the step edges and corners of crystals, a reactant made of smaller particles will have increased reactivity as there are more of these present. However, if the active site is large and requires several atoms on a surface, very small particles will not provide such sites. Consequently, in some catalytic systems optimal particles sizes are observed.[32]

Overall, the provision of high surface area materials are usually advantageous for surface-mediated reactions. This concept largely provides the incentive for the study of the materials within this thesis. In Chapter 3, FeTi nanoparticles are the goal because absorption of H_2 gas is slow in the bulk material. The possible synthesis of single walled carbon nanotubes from very small iron particles incites the size-controlled synthesis of iron and iron oxide nanoparticles in Chapter 3. This concept also underpins the exploration of employing iron oxide-capped iron nanoparticles for metal ion remediation in Chapters 4 and 5.

Also of importance to this report, small particles have a depressed melting point from their bulk counterparts. Experimentally, the depression in melting point is approximately inversely proportional to the radius of the particle.[31] More complex theoretical relationships have been derived to help explain and describe the deviations from this approximate relationship of which there have been many attempts. Some use strict thermodynamic arguments,[31, 34] while others evoke vibronic arguments.[31, 35, 36]

Molecular dynamic calculations are also seen in the literature.[35, 36] All cases stem from the argument that surface atoms are not as tightly bound as their core neighbours. This has been manifested in the different theories as surface tension terms,[31] or as bonds more easily broken by thermal vibrations.[31, 35, 36]

The degree to which melting point is suppressed varies with material. For instance, 2 nm gold particles have over a 1000 °C depression in melting point from the bulk. Even 7 nm particles observe over a 200 °C depression in melting point.[31] However, lead particles only see a ~150 °C depression in melting point for ~4 nm particles.[34] For ~7 nm tin particles, the depression is only 20 °C.[34]

In Chapter 2, the synthesis of FeTi nanoparticles is hindered by the inhibition of dissolution of one metal into the other. We rely on melting point depression of nanoparticles to allow for the formation of the intermetallic (melting point of the bulk material is 1317 °C [20]) at temperatures readily available to the synthetic chemist in the solution phase (< 500 °C).

1.3 Particle synthesis and nucleation and growth theories

To begin an exploration of the synthesis of iron-containing nanoparticles, it is useful to become familiar with some of the governing theories that dictate particle nucleation and growth. These classic theories will be the context in which our experimental results will be discussed, especially in Chapter 3. There are three major concepts which describe different aspects of particle nucleation and growth: classical nucleation theory, the LaMer model of burst nucleation, and Ostwald ripening. They are described here within the relevant frame of reference of the preparation of iron nanoparticles.

Using solution methods, the preparation of high surface area iron materials can be described by a general synthesis (Figure 1-2),

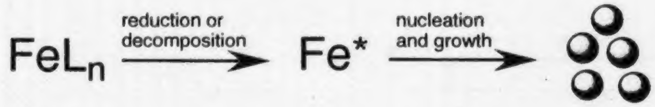

Figure 1-2 A general and ideal solution synthesis for the formation of iron particles.

A molecular iron species (FeL_n) in solution is transformed, usually through decomposition or reduction, to produce solvated iron atoms (Fe*). These species are assumed to collide in a sequential binuclear manner to form iron nuclei which grow into particles.[37] There is some debate whether the species that form particles are actually bare iron atoms and not a partially decomposed molecular species.[28] However, this simplification is advantageous for understanding the theories on nucleation and growth of particles under these synthetic conditions. [38]

1.3.1 Classical Nucleation Theory

Although the theory has undergone some significant development and expansion in recent years,[37, 39, 40] classical nucleation theory provides a good basis for a qualitative discussion on nanoparticle formation in solution. It was initially developed for vapor phase condensations, and the theory has since been extended to nuclei formation from solutions.[37] The approach is a thermodynamic one, contrasting the Gibbs free energy for creating the volume of a particle (favoured) with the Gibbs free energy of creating a new surface (disfavoured). Since the first is dependant on the volume of the nuclei and the second on the surface area, the thermodynamic barrier for nucleation, ΔG_N, for spherical nuclei can be described as:

$$\Delta G_N(r) = \tfrac{4}{3}\pi r^3 \Delta G_V + 4\pi r^2 \gamma \qquad (1)$$

Where ΔG_V is the volume free energy of the nuclei (a negative value), γ the surface energy between the particle and the solution (positive value), and r the radius (Figure 1-3). As a result of the two dependencies on r, there is a critical radius r^* where the ΔG_N is at a maximum:

$$r^* = {}^{-2\gamma}\!/\!_{\Delta G_V} \qquad (2)$$

This is the minimum radius for nuclei to be thermodynamically stable. Below this radius, nuclei lower their free energy by dissolving. Above this radius, the free energy is minimized by particle growth (Figure 1-3).[37]

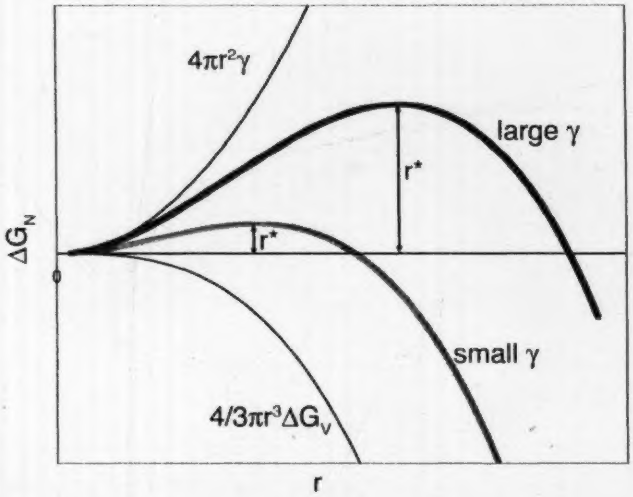

Figure 1-3 Classical nucleation theory description of the dependence of the thermodynamic barrier for nucleation with respect to radius. Adapted from Ref. (41).

For the present thesis, the key ramification is as such: lowering the surface energy of a particle (γ) lowers the critical radius causing smaller nuclei to be thermodynamically stable to dissolution. Furthermore, a lowering of γ causes a general thermodynamic stabilization of smaller particles (Figure 1-3). Consequently, lowering the surface energy of particles with the use of surface-bonding surfactants is one of the most common techniques for obtaining small particles. (Although not a part of "classical nucleation theory" it should also be noted that surfactants also cause a kinetic stabilization of small particles[42] by steric prevention of collisions between the particles and solvated precursors - a requirement for growth.)

Classical nucleation theory also predicts the concentration of nuclei forming. Applying a Boltzman distribution and collision theory, the number density of nuclei of a given radius, $N(r)$ is given by:

$$N(r) = [\mathrm{Fe}^*]\ \exp\left[\frac{\Delta G_N(r)}{k_B T}\right] \qquad (3)$$

Where [Fe^*] is the number concentration of the precursor for nucleation, k_B the Boltzman constant and T the temperature.[37] A high concentration of Fe* will provide many nuclei above the critical radius, and the precursor will be preferentially used for nuclei formation rather than growth onto existing particles. This is the second technique for obtaining small particles: experimental design to afford a large Fe* concentration through rapid decomposition, addition of reagents, *etc.*

1.3.2 The LaMer model for burst nucleation

This particular approach of rapid decomposition has been further expanded on by the LaMer model[38] which relates the concentration of the precursor with nucleation and growth behaviour. The LaMer model also explains "burst nucleation" where a lag time is observed before particles are formed and the produced particles tend to be monodisperse.

Following a concentration versus time curve (Figure 1-4), the concentration of Fe* is increased to supersaturation, C_s, but nuclei do not form until the concentration reaches C_0, the minimum concentration for nucleation. The concentration continues to climb until the maximum concentration for nucleation, C_N is reached. At this concentration, the rate of nucleation is extremely high and the concentration of Fe* decreases from its use in nucleation events. Once the concentration drops below C_0, nucleation is arrested and the drop in concentration is from growth onto existing nuclei. [38]

This behavior tends to give monodisperse particles because all the nuclei are formed within a short time frame, and growth therefore occurs evenly. Often this behaviour is discussed as a time separation of nucleation and growth processes to give monodisperse particles.[38] This type of behavior will be seen throughout Chapter 3 when near monodisperse particles are synthesized from the decomposition of $Fe(CO)_5$ in oleic acid and other surfactants. However, if Fe* has very low solubility in the medium and there is little concentration difference in C_s and C_o, nucleation and growth will happen somewhat indiscriminately causing polydispersivity.[38] The materials employed in Chapters 4 and 5, synthesized from the reduction of iron (III) chloride by sodium borohydride in water, result from this type of behavior.

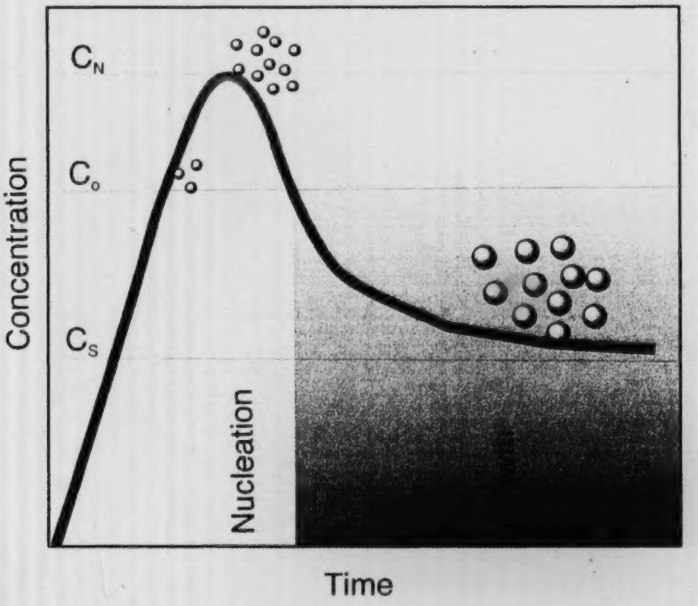

Figure 1-4 The LaMer model for burst nucleation. Adapted from Ref. (38)

As an extension of this, if we compare two reactions with the same amount of iron precursor, the one that provides a quick production of Fe* will have much of the iron used up while the concentration is above C_o - namely in nucleation events and less so in growth. A slow production of Fe* will allow for less of the total iron involved in nucleation events and more in growth. Therefore, providing a rapid increase in the concentration of Fe* will allow for smaller particles.

1.3.3 Ostwald ripening

Ostwald ripening was first described in 1900. Like nucleation theory and the LaMer model, the theory behind this coarsening behaviour has undergone recent development in attempts to give quantitative predictions,[43-45] yet the qualitative description suffices for the purpose of this thesis.

Small particles are dissolved and reprecipitated onto the larger ones making the particle sizes larger and larger. Starting with small monodisperse particles, the Ostwald ripening process will produce larger particles and a wider particle size distribution. Ostwald ripening can be described as a phenomena driven by the minimization of the high energy interfaces between particles and the solution.[43] Ostwald ripening relies on Fe* being reversibly soluble in solution and diffusing to larger particles. Therefore, Ostwald ripening only occurs when conditions are conducive to the dissolution of small particles.

1.4 Transmission Electron Microscopy (TEM)

1.4.1 Imaging and diffraction

The size of the particles within this study are typically 2-100 nm in diameter and therefore imaging them is outside the capabilities of optical microscopy. In 1925, Louis de Broglie theorized the wave-like nature of electrons. Their mass and velocities allow for very small so-called de Broglie wavelengths, and it is this property which is exploited in Transmission Electron Microscopy.[46] We use TEM and the associated techniques as the workhorse of characterization for Chapters 2 and 3 and briefly in Chapter 4 as it can readily be used to determine particle size, crystal morphology and elemental identification.

Electrons are emitted from a source (in this study a LaB_6 crystal heated and under a 120-200 keV bias) and pass through a series of condenser apertures, magnetic stigmators and magnetic lenses to focus the beam onto a sample. The beam passes through the sample and the image of the sample is magnified by objective, intermediate, and projector lenses and further improved by other stigmators and apertures. At this time, the electrons come in contact with a scintillating phosphor such as ZnS, a CCD camera or electron sensitive film so that the human eye can observe the image (Figure 1-5).[47] Because this is a transmission technique, the image observed can be thought of as two dimensional shadows of the sample.[48] The technique is extremely powerful for imaging single layers of dispersed nanoparticles of the size regime indicated above.

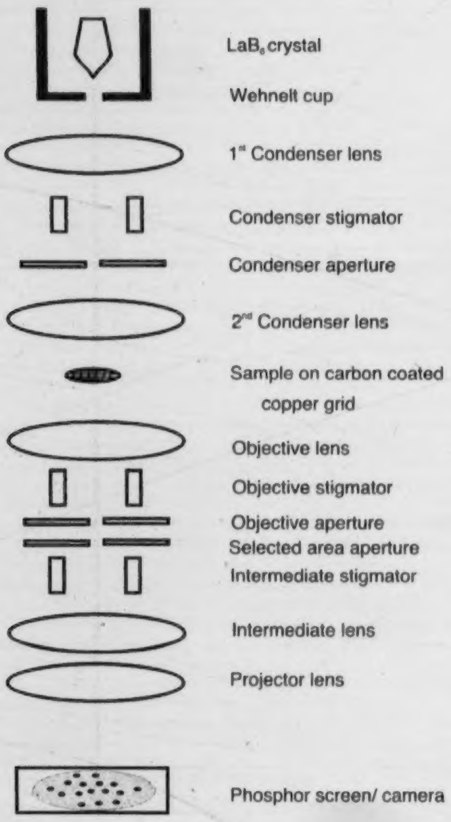
LaB_6 crystal
Wehnelt cup
1st Condenser lens
Condenser stigmator
Condenser aperture
2nd Condenser lens
Sample on carbon coated copper grid
Objective lens
Objective stigmator
Objective aperture
Selected area aperture
Intermediate stigmator
Intermediate lens
Projector lens
Phosphor screen/ camera

Figure 1-5 Schematic of the optics of a Transmission Electron Microscope. Based loosely on the JEOL 2010 instrument belonging to the University of Alberta Department of Physics and the primary instrument used for this report.

The limit of resolution of the instrument comes from several sources. Under the voltages typically employed in an TEM, the wavelengths of electrons are only several picometres and therefore not directly the cause of the limit of resolution. Instead, optical phenomena from the lenses limit resolution, dominated by spherical aberration.[49] Spherical aberration is caused by the off-axis electrons being bent by the lenses more strongly than those on axis.[50] As a result, point objects are imaged as a disk with a finite size.

The theoretical limit of resolution for a TEM can be approximated as

$$r_{\min} \approx 0.91(C_s \lambda^3)^{1/4} \qquad (4)$$

where r_{min} is the theoretical limit of resolution, C_s the spherical aberration constant for a given lens (or lens system), and λ the wavelength of the electrons. This number is typically 0.25-0.3 nm. In practical terms, the magnification may be increased, but no additional detail below this size range will be observed.[49] In practice, features and details of this size are not commonly observed without extensive alignment and correction for other optical aberrations and stigmations as well as a minimization of external vibrations to the TEM (people walking in the building, *etc.*). For the smallest particles in this study (~2-5 nm), the resolution of the instrument belonging to the University of Alberta Physics Department running at 200 keV gave more than sufficient resolution to accurately measure size. However, the instrument belonging to Ohio State University (used for parts of Chapter 3) running at 120 keV gave images that indicated features of this size; however, diameters could not be determined with satisfactory accuracy. Such samples were necessarily re-imaged with the instrument running at the higher accelerating voltage.

Two types of contrast are dominant throughout this study. Firstly, Rutherford scattering prevents electrons from hitting the screen and provides dark areas on a light screen. The scattering is increased by thicker samples and by Z^2, where Z is the atomic mass of the atoms in the sample.[51] For this reason, the carbon film used as a support for samples gives very little contrast, yet the particles of iron on the support are easily imaged.

The second important source of contrast is diffraction contrast. Electrons passing though a crystalline sample are diffracted according Bragg's Law.[52]

$$n\lambda = 2\,d\sin\theta \qquad (5)$$

Where n is an integer, λ the wavelength of the incident electrons, d is the spacing between crystallographic planes, and θ the acute angle of the diffracted beam with the non-diffracted beam.

Depending on the crystallographic orientation of each crystal to the electron beam, different numbers of electrons are diffracted giving differing contrast.[52] For the crystalline particles seen in Chapter 3, some appear darker than others as a result of diffraction contrast.

For crystalline samples, as stated earlier, the electrons may be diffracted. By changing the strength of the intermediate lens, one can choose to image the resulting diffraction pattern. A single crystal gives an array of spots corresponding to reflections from the different crystallographic planes. Diffraction from many crystals with random orientations gives a ring pattern. The ratio of the radii of the rings may be related back to Bragg equation and used as a tool for identifying crystallographic phases in a similar manner to powder X-ray diffraction.[52] This technique is called Selected Area Electron Diffraction (SAED).

One note should be made with regard to the electron microscopes at our disposal. Unfortunately, samples could not be introduced into the TEM without exposure to air. Even though many of our synthesis predicted the formation of metallic particles, often only the oxides resultant from air exposure were observed by TEM.

1.5.2 Energy Dispersive Spectroscopy (EDS)

The bombardment of a sample with a beam of high energy electrons gives rise to inelastic scatter some of the electrons and causes corresponding ejection of core electrons from the sample. This leaves core vacancies in sample atoms. The collapse of higher energy electrons to the core level causes the emission of characteristic X-rays which are collected by a detector for Energy Dispersive Spectroscopy (EDS).[53]

The principal quantum number of the orbital from which the core electron is ejected gives the primary label; in X-ray notation n = 1, 2 and 3 are called K, L and M shells, respectively. The subscript identifies the shell from which the higher energy electron drops to emit the X-ray; the change in principal quantum number for this drop are labeled α, β, γ, *etc.* for changes of 1, 2 and 3 quantum numbers, respectively.[53]

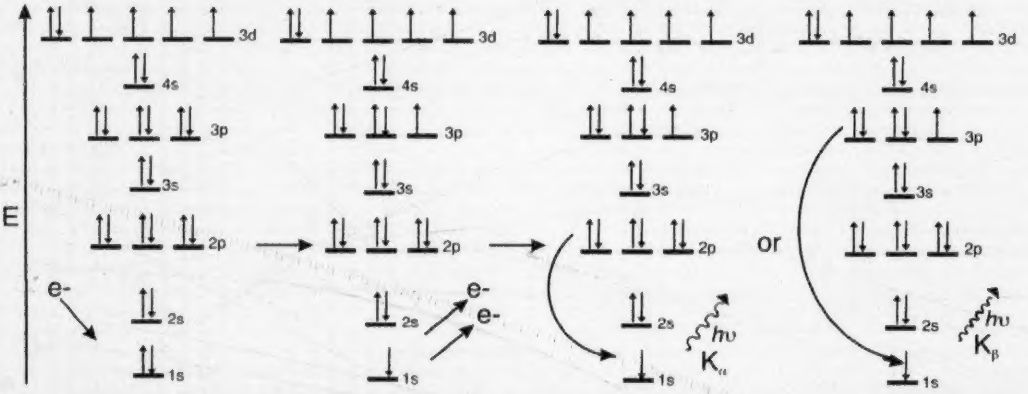

Figure 1-6 The origin of characteristic K_α and K_β X-rays for iron in the electron microscope which are collected for EDS. s-s transitions are symmetry forbidden and are therefore not commonly observed.[54]

EDS is used as a powerful elemental identification technique in electron microscopes.[53] Although EDS instruments can be quantitative,[55] the instrument and software at our disposal was not appropriately standardized. Despite this, for atoms of similar size, and when comparing the same line, the sensitivities are similar[55] and generalizations can be made by examining the peak height. Appropriate statements in these cases include, "there is more… than…", "there is less… than…", "there are similar amounts of…" For example, in Chapter 2, peak heights of the K_α signals of iron and titanium are compared qualitatively to determine approximate compositions in this manner.

1.5 X-Ray Photoelectron Spectroscopy (XPS)

X-Ray Photoelectron Spectroscopy is an application of Einstein's Nobel Prize-winning photoelectric effect. It yields information about the elements present as well as information about oxidation states or chemical environments of the element.[56] XPS is used extensively in Chapters 4 and 5 to identify the oxidation state of metals absorbed onto iron oxide capped particles and to infer mechanisms of sequestration.

A sample is illuminated with monochromatic X-rays and electrons are ejected with varying kinetic energies (*KE*) depending on the elements present. The relationship between the incident X-rays and the kinetic energy of the photoelectron, in a simplified form is:

$$KE = h\nu - BE \qquad (6)$$

where h is Plank's constant and ν is the frequency of the incident X-ray. The Binding Energy, *BE*, is the energy required to ionize an electron.[56] The ejected electrons are collected and binned according to their kinetic energy to yield a spectrum usually plotted as counts (or intensity) *versus* energy in electronvolts (eV). Typically, XPS spectra are not reported as a function of kinetic energy, which depends on the X-ray source, but rather source-independent binding energy. XPS focuses on ionizing core electrons from atoms. Since different elements will have different binding energies for their core electrons, in its simplest manifestation, XPS can be used as a elemental identification technique.[56] High resolution spectra give much more detailed chemical information but are complicated by subtleties.

For a given element, the binding energy is perturbed by chemical environment and especially oxidation state; an oxidized atom will have a collapse of all the remaining electrons toward the nucleus and therefore will have a larger binding energy for the ejection of a core electron. Consequently, high resolution XPS, which focuses on a small range of binding energy for a single element, can be used to identify oxidation state (Figure 1-7) and sometimes chemical environment.[56] This is typically done by comparison to standards and literature spectra.

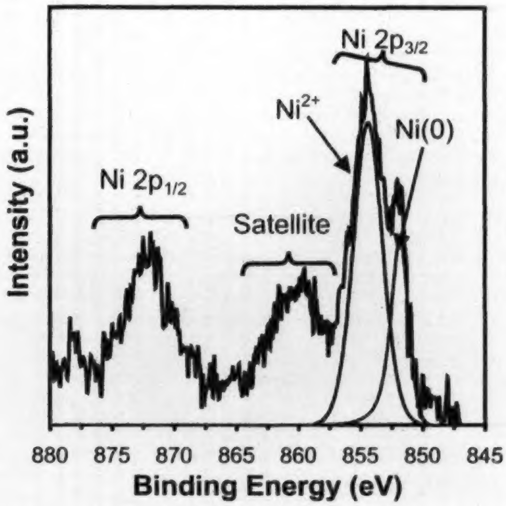

Figure 1-7 An example high resolution XPS of a Ni containing sample showing two spin orbit couples, a satellite peak and shifts in binding energy due to oxidation state. Gaussian-Lorentzian peak fitting is highlighted in blue. Asymmetric fitting of the zero oxidation state is highlighted in red.

After the ejection of a photoelectron, the remaining unpaired electron can couple with the angular momentum of the orbital it is in (except for electrons in the spherical S orbitals, which has no angular momentum). The total spin of the system is the angular momentum of the orbital plus the spin of the unpaired electron.

$$j = l + s \qquad (7)$$

where j is the total spin, l the angular momentum quantum number of the orbital from which the electron is ejected ($l = 0, 1, 2\ldots$) and s the spin of the electron($s = ½, -½$). The two possible spins of the electron results in two observed binding energies called spin orbit couples (Figure 1-7). The ratio of the spin degeneracies ($2j+1$) gives the ratio of the peak intensities.[57]

The nomenclature for labeling XPS emissions involves the relevant element, followed by the principal quantum number and orbital label *(i.e.*, s, p, d...) of the orbital from which the electron is ejected. The spin state, j, is then provided in subscript (*e.g.*, Ni $2p_{1/2}$) (Figure 1-7).[57]

The phenomenon of lower energy "shake up" satellite peaks is worth mentioning as it appears in some of the spectra reported in Chapter 5. Sometimes the incident X-ray can cause ejection of the photoelectron *and* the promotion of one of the valence electrons into a higher energy state. The photoelectron will have a correspondingly lower kinetic energy giving an additional high binding energy peak (Figure 1-7).[58]

In a similar fashion, the ejection of a photoelectron combined with promotion of a valence electron affects the peak shape of metallic signals. For metallic materials there is a continuum of states into which the valance electron may be promoted. Instead of a discrete satellite, this manifests as the zero oxidation state peak having a asymmetric shape with a tail into higher binding energy.[58] This is different from the Gaussian-Lorentzian[59] shaped peaks usually fitted (Figure 1-7).

If an atom has non-zero spin in its valence shell, there will be two non-degenerate spin states for the atom after the ejection of the photoelectron; the remaining core electron will have spin either parallel or anti-parallel with the spins of the valence electrons. (Figure 1-8). The corresponding two binding energies observed are referred to as multiplet splitting. The differences in binding energy for multiplet splitting are much weaker than those seen for spin-orbit coupling. For the transition metals, multiplet splitting greatly complicates peak fitting. [23, 56, 58] For this reason and because simple fittings provided the necessary information, assignment of fitted peaks of transmission metals in Chapter 5 is very general and non-rigorous.

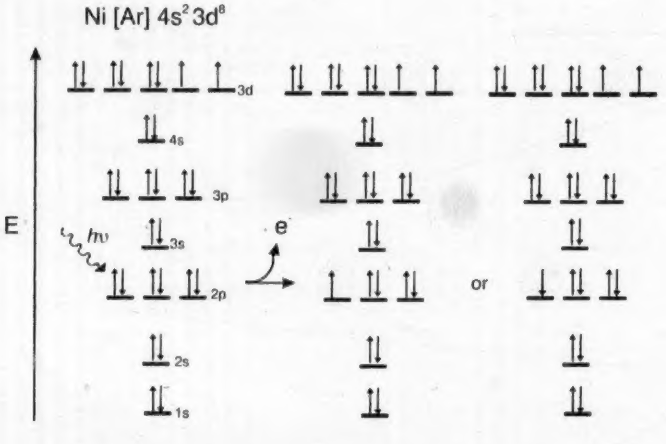

Figure 1-8 Source of XPS multiplet splitting in Ni(0).

It is important to remember that XPS is a surface technique. Much of the signal originates from the interactions within the top 10 nm of the material studied.[56] Although quantification of elemental composition is possible,[56] the spatial inhomogeneity of the samples of this study (i.e., in Chapters 4 and 5, the cores of the 20-80 nm particles are of a different composition than the shells) make such analysis inappropriate.

1.6 Scope of the thesis

The intermetallic FeTi has been identified as a hydrogen storage material but suffers from slow hydrogen absorption and desorption kinetics. We postulate the high surface area afforded by Fe-Ti nanoparticles would alleviate this problem. Chapter 2 is a series of experiments in the attempt to synthesize Fe-Ti nanoparticles using solution techniques already proven successful for other transition metal alloys.

Chapter 3 is a description of techniques to prepare iron and iron oxide nanoparticles of sizes less that 4 nm from the decomposition of $Fe(CO)_5$ in solvent and surfactant mixtures. Many different factors and techniques are explored, including surfactant choice, the role of impurities (especially water), the introduction of reagents into hot solvents and sonication techniques. The results are described as manifestations of the play off between the inhibition of nucleation and growth.

From there, our knowledge of iron particles is applied to the difficult problem of removing trace metal catalysts from reaction media in Chapter 4. Iron oxide capped iron particles are used to adsorb and reduce late transition metal catalysts onto particle surfaces. The particles are then removed by filtration yielding reaction products with much lowered trace metal concentrations. The technique is expanded on and modified in Chapter 5 to work for catalysts that contain coordinating phosphines. To achieve this, small bifunctional molecules are added to the mixture to bind to the catalysts and the particle surfaces. Extensive XPS of the particles after sequestration is used to illuminate the mechanisms of sequestration under the coordinating and non-coordinating conditions is described.

Chapter 6 provides a summary of the findings of the previous chapters and also presents directions for future work.

1.7 References

1 R. Tewari, *Antiquity,* 2003, **77**, 536-544.

2 R. M. Cornell and U. Schwermann, *The Iron Oxides: Structure, Properties, Reactions, Occurrences and Uses*, Second edn., Wiley-VCH, Weinheim, 2003, pp. 475-489.

3 M. M. P. Muir, *The Story of Alchemy and the Beginnings of Chemistry*, Hodder And Stoughton, London, 1902.

4 T. Bayley, *Journal of the Chemical Society, Transactions,* 1880, **37**, 828-836.

5 L. Mond and C. Langer, *Journal of the Chemical Society, Transactions,* 1891, **59**, 1090-1093.

6 H. J. H. Fenton, *Journal of the Chemical Society, Transactions,* 1894, **65**, 899-910.

7 S. E. Hazlet and C. A. Dornfeld, *Journal of the American Chemical Society,* 1944, **66**, 1781-1782.

8 R. M. Cornell and U. Schwermann, *The Iron Oxides: Structure, Properties, Reactions, Occurrences and Uses*, Second edn., Wiley-VCH, Weinheim, 2003, pp. 119-130.

9 A. T. Larson and C. N. Richardson, *Industrial and Engineering Chemistry,* 1925, **17**, 971.

10 H. Yokoi and T. Kantoh, *Bulletin of the Chemical Society of Japan,* 1993, **66**, 1536-1541.

11 Y. H. Zhou, M. Harmelin and J. Bigot, *Materials Science and Engineering a-Structural Materials Properties Microstructure and Processing,* 1991, **133**, 775-779.

12 S. Gangopadhyay, G. C. Hadjipanayis, B. Dale, C. M. Sorensen, K. J. Klabunde, V. Papaefthymiou and A. Kostikas, *Physical Review B,* 1992, **45**, 9778-9787.

13 P. C. Kuo, C. Y. Chang, T. S. Wu, Y. H. Chang and T. K. Hsu, *Journal of Materials Science Letters,* 1982, **1**, 137-140.

14 T. Miyahara and K. Kawakami, *IEEE Transactions on Magnetics,* 1987, **23**, 2877-2881.

15 R. F. Ziolo, E. P. Giannelis, B. A. Weinstein, M. P. O'Horo, B. N. Ganguly, V. Mehrotra, M. W. Russell and D. R. Huffman, *Science,* 1992, **257**, 219-223.

16 T. Hyeon, L. Su Seong, J. Park, Y. Chung and N. Hyon Bin, *Journal of the American Chemical Society,* 2001, **123**, 12798-12801.

17 R. S. Ram and P. F. Bernath, *Journal of Molecular Spectroscopy,* 2003, **221**, 261-268.

18 B. Meunier and J. Bernadou, *Active Iron-Oxo and Iron-Peroxo Species in Cytochromes P450 and Peroxidases; Oxo-Hydroxo Tautomerism with Water-Soluble Metalloporphyrins*, Springer, Berlin, 2000.

19 R. M. Cornell and U. Schwermann, *The Iron Oxides: Structure, Properties, Reactions, Occurrences and Uses*, Second edn., Wiley-VCH, Weinheim, 2003, pp. 9-38.

20 H. Okamoto, *Journal of Phase Equilibria,* 1996, **17**, 369-369.

21 R. M. Cornell and U. Schwermann, *The Iron Oxides: Structure, Properties, Reactions, Occurrences and Uses*, Second edn., Wiley-VCH, Weinheim, 2003, p. 176.

22 D. L. A. deFaria, S. V. Silva and M. T. deOliveira, *Journal of Raman Spectroscopy,* 1997, **28**, 873-878.

23 A. P. Grosvenor, B. A. Kobe, M. C. Biesinger and N. S. McIntyre, *Surface and Interface Analysis,* 2004, **36**, 1564-1574.

24 N. S. McIntyre and D. G. Zetaruk, *Analytical Chemistry,* 1977, **49**, 1521-1529.

25 G. Ketteler, W. Weiss, W. Ranke and R. Schlogl, *Physical Chemistry Chemical Physics,* 2001, **3**, 1114-1122.

26 A. R. West, *Basic Solid State Chemistry*, Second edn., Wiley, Toronto, 1999, p. 375.

27 C. M. Hessel, E. J. Henderson and J. G. C. Veinot, *Chemistry of Materials,* 2006, **18**, 6139-6146.

28 D. L. Huber, *Small,* 2005, **1**, 482-501.

29 A. R. Shahverdi, A. Fakhimi, H. R. Shahverdi and S. Minaian, *Nanomedicine-Nanotechnology Biology and Medicine,* 2007, **3**, 168-171.

30 N. Lewinski, V. Colvin and R. Drezek, *Small,* 2008, **4**, 26-49.

31 O. Koper and S. Winecki, Specific Heats and Melting Points of Nanocrystalline Materials in *Nanoscale Materials in Chemistry,* K. J. Klabunde, John Wiley and Sons Inc., Toronto, 2001, pp. 263-277.

32 K. J. Klabunde and R. S. Mulukutla, Chemical and Catalytic Aspects of Nanocrystals in *Nanoscale Materials in Chemistry,* K. J. Klabunde, John Wiley and Sons, Inc., Toronto, 2001, pp. 223-261.

33 K. J. Klabunde, J. Stark, O. Koper, C. Mohs, D. G. Park, S. Decker, Y. Jiang, I. Lagadic and D. Zhang, *Journal of Physical Chemistry,* 1996, **100**, 12142-12153.

34 P. Letellier, A. Mayaffre and M. Turmine, *Physical Review B,* 2007, **76**, 45428–45421-45428.

35 F. Ding, A. Rosen and K. Bolton, *Physical Review B,* 2004, **70**, 075416–075411-075416.

36 H. M. Duan, F. Ding, A. Rosen, A. R. Harutyunyan, S. Curtarolo and K. Bolton, *Chemical Physics,* 2007, **333**, 57-62.

37 T. A. Ring, *Advances in Colloid and Interface Science* 2001, **91**, 473-499.

38 V. K. LaMer and R. H. Dinegar, *Journal of the American Chemical Society,* 1950, **72**, 4847-4854.

39 D. T. Robb and V. Privman, *Langmuir,* 2008, **24**, 26-35.

40 W. Vogelsberger, *Journal of Physical Chemistry B* 2003, **107**, 9669-9676.

41 U. Schubert and N. Hüsing, *Synthesis of Inorganic Materials*, Wiley-VCH, Weinheim, 2000, pp. 135-154.

42 N. Herron, Y. Wang and H. Eckert, *J. Am. Chem. Soc.*, 1990, **112**, 1322-1326.

43 P. W. Voorhees, *Journal of Statistical Physics,* 1985, **38**, 231-252.

44 R. Mendoza, I. Savin, K. Thornton and P. W. Voorhees, *Nature Materials,* 2004, **3**, 385-388.

45 P. W. Voorhees, *Annual Review of Materials Science,* 1992, **22**, 197-215.

46 R. F. Egerton, *Physical Principles of Electron Microscopy*, Springer, 2005, pp. 1-16.

47 D. B. Williams and C. B. Carter, *Transmission Electron Microscopy*, Springer, New York, 1996, p. 108.

48 D. B. Williams and C. B. Carter, *Transmission Electron Microscopy*, Springer, New York, 1996, p. 10.

49 D. B. Williams and C. B. Carter, *Transmission Electron Microscopy*, Springer, New York, 1996, pp. 97-102.

50 R. F. Egerton, *Physical Principles of Electron Microscopy*, Springer, 2005, pp. 44-49.

51 D. B. Williams and C. B. Carter, *Transmission Electron Microscopy*, Springer, New York, 1996, p. 353.

52 R. F. Egerton, *Physical Principles of Electron Microscopy*, Springer, 2005, pp. 106-112.

53 R. F. Egerton, *Physical Principles of Electron Microscopy*, Springer, 2005, pp. 158-161.

54 G. L. Miessler and D. A. Tarr, *Inorganic Chemistry*, 2nd edn., Prentice-Hall, Toronto, 1998, pp. 362-363.

55 D. B. Williams and C. B. Carter, *Transmission Electron Microscopy*, Springer, New York, 1996, pp. 599-608.

56 C. R. Brundle, X-Ray Photoelectron Spectroscopy in *Encyclopedia of Materials Characterization*, eds. C. R. Brundle, J. Charles A. Evans and S. Wilson, Butterworth-Heinemann and Manning, Toronto, 1992, pp. 282-299.

57 D. Briggs and J. C. Rivière, Spectral Interpretation in *Practical Surface Analysis*, eds. D. Briggs and M. P. Seah, John Wiley and Sons, Toronto, Second edn., 1990, vol. 1: Auger and X-ray Photoelectron Spectroscopy, pp. 85-87.

58 D. Briggs and J. C. Rivière, Spectral Interpretation in *Practical Surface Analysis*, eds. D. Briggs and M. P. Seah, John Wiley and Sons, Toronto, Second edn., 1990, vol. 1: Auger and X-ray Photoelectron Spectroscopy, pp. 112-133.

59 P. M. A. Sherwood, Data Analysis in XPS and AES in *Practical Surface Analysis*, eds. D. Briggs and M. P. Seah, John Wiley and Sons, Toronto, Second edn., 1990, vol. 1: Auger and X-ray Photoelectron Spectroscopy, pp. 572-574.

Chapter 2: The Synthesis of FeTi intermetallic nanoparticles

2.1 Introduction

In the current push towards the development of a hydrogen-based energy economy, one of the major hurdles is the development of a means for safe and effective storage of hydrogen. In an ideal case, the way in which hydrogen is stored would both have high volume density (take up a small space), and a small mass density (still weigh a small amount). Although many creative methods have been proposed and studied over the last 40 years, ideal materials have yet to be developed and implemented on a grand scale.[2, 3]

Several metals and intermetallic materials have been found to reversibly store hydrogen with very high volume densities including $LaNi_5$, Pd, Mg, and FeTi.[3-5] These materials have been studied since the 1970s for this feature.[6] Unfortunately, each has its own drawbacks including prohibitive cost, high temperatures required for hydrogen cycling, and/or slow up-take and release of hydrogen.[3, 7]

The FeTi intermetallic is of particular interest because of its use of inexpensive and relatively light metals.[3] These materials have not reached their potential in applications primarily because of two factors: first, although the volume density of hydrogen stored is acceptable for stationary applications, hydrogen sorption and desorption is prohibitively slow.[3, 7] Second, the known preparative methods for FeTi are inappropriate for cost-effective scale up: namely, high energy ball milling,[4, 8] or thermal[9] and plasma[10] depositions of layers of FeTi onto substrates.

The problems of slow absorption and desorption kinetics and synthesis techniques being incompatible for scale-up can be solved by developing a solution based synthesis of nanoparticles of FeTi. Solution syntheses are readily scaleable when compared to the physical techniques listed above. Due to the large surface area to volume ratio, nanomaterials are predicted to have faster hydrogen sorption and desorption rates. [4-6]

Many nanoparticles of metallic alloys and intermetallics grace the literature in both mixed and core-shell structures.[11] However, to our knowledge, those reported to date are only alloys of metals from the latter half of the transitions metals (with a few exceptional main group metals).[11] The preparation of alloy or intermetallic nanoparticles containing an early transition metal, Ti, will be a significant step for the nanoparticle community.

There are several major techniques for the synthesis of alloy and intermetallic nanoparticles. This report will focus on the chemical co-reduction of precursors,[12-16] and solution phase thermal decomposition of low valent organometallic precursors.[17, 18] Alloys and intermetallics have also been prepared by the synthesis of core-shell nanoparticles followed by annealing.[11, 16]

The two known intermetallics of iron and titanium are FeTi and Fe_2Ti (Figure 2-1). This study focuses on the formation of FeTi, for its aforementioned advantages, which has a CsCl crystal structure. The room-temperature phase of the individual elements is body centered cubic (bcc) for α-Fe and hexagonally close packed (hcp) for α-Ti.[19] This structural mismatch between the two elements indicates the pure phases may not readily nucleate onto seeds of one another, *i.e.*, epitaxial growth will not be facile [20] Although a daunting prospect, many late transition metal alloys and intermetallics have been prepared where there is a structural mismatch between the two elemental structures.[11]

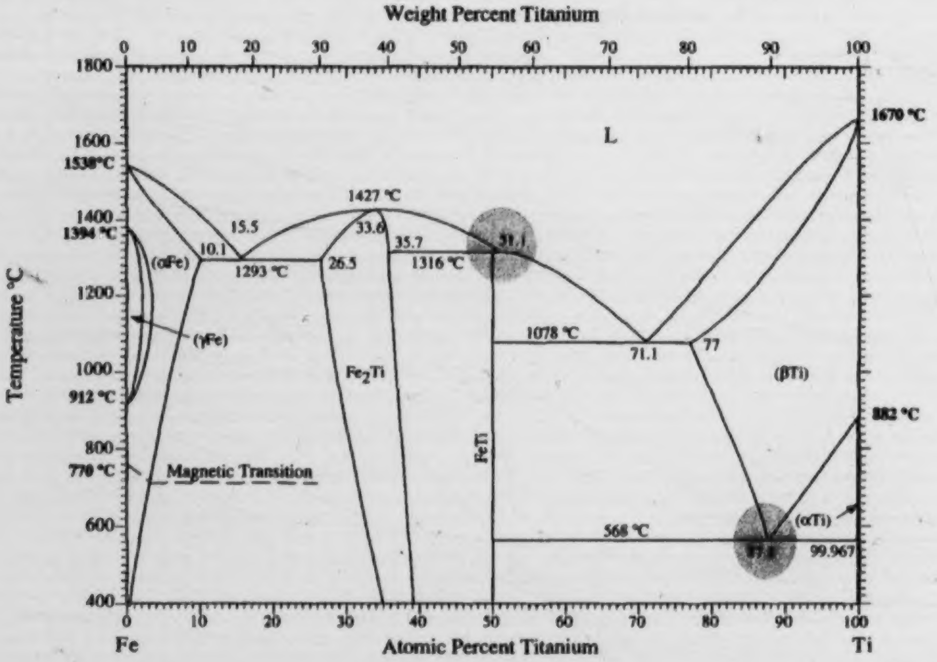

Figure 2-1 The binary phase diagram for iron and titanium.[1] Highlighted areas are the melting point of FeTi and the minimum temperature for the formation of β-Ti.

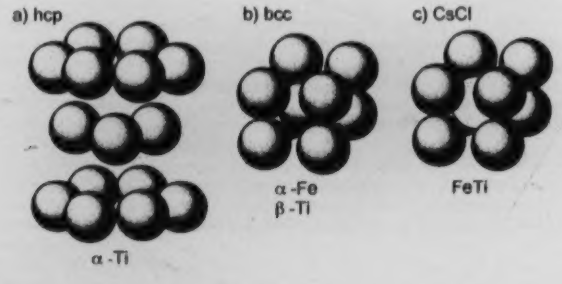

Figure 2-2 Relevant crystallographic structures a) hexagonally close packed (expanded vertically for visualization) b) body centred cubic c) CsCl. [21, 22]

The CsCl structure of FeTi [7] resembles bcc but with the atom at the body centre replaced by the heteroatom. Therefore, the FeTi structure more closely resembles bcc α-Fe than the hcp α-Ti (Figure 2-1). It is a bit of a surprise therefore that the formation of FeTi has been shown to involve the diffusion of Fe into Ti.[23] At a few % Fe (temperature dependant), Ti is converted to the bcc form, β-Ti. This is followed by increased dissolution of Fe to form the intermetallic (Figure 2-2). [1, 23]

Therefore, to form the CsCl structure, the most promising approach is to attempt a co-deposition of iron and titanium. Failing that, the preferential formation will be an iron core and a titanium shell to take advantage of the Kirkendall Effect [20, 24] and the preferential diffusion of iron into titanium.[23] As well, high temperatures will promote the formation of β-Ti[21] presumably aiding the formation of FeTi. We will also attempt syntheses at elevated temperatures. Although 568 °C (Figure 2-1) cannot be readily reached in solution chemistry, the depressed melting points seen for nanoparticles[25] may make this "ideal" temperature lower.

2.2 Experimental Procedures

2.2.1 Instrumentation and reagents

Transmission Electron Microscopy (TEM) samples were prepared by suspending particles in THF and drop-coating the solution onto carbon coated, 200 mesh Cu grid (SPI Supplies). Samples were evaluated using a JEOL 2010 Transmission Electron Microscope (TEM) at 200 keV accelerating voltage and a LaB_6 filament. This instrument was also fitted with Energy Dispersive X-Ray Spectroscopy (EDS) detector for elemental analysis.

Naphthalene was purchased from Fisher Scientific, potassium from Anachemia and titanium clusters from Strem. All other chemicals were purchased from Aldrich and used without purification unless otherwise noted. Pentane, 1,2-dimethoxyethane (DME) and tetrahydrofuran (THF) were dried and distilled from Na/benzophenone and methanol from magnesium turnings. Standard Schlenk techniques were used in all cases. "Sonication" in this chapter refers to a standard laboratory ultrasonic bath. Yields of nanoparticle products are not reported as the presence of surfactant hinders the acquisition of a meaningful number.

Preparation of $TiCl_4(THF)_2$

$TiCl_4(THF)_2$ was prepared according to a modified literature procedure.[26] $TiCl_4$ (5.80 mL, 52 mmol) was dissolved in 80 mL of pentane under argon. THF (18 mL, 200 mmol) was added slowly and a yellow precipitate formed. The solution was cooled to -20 °C for 40 minutes. The excess solvent was removed and the remaining precipitate dried *in vacuo*. $TiCl_4(THF)_2$ (17 g, 97% yield, mp 122-128 °C)

2.2.2 Co-reductions of metal chlorides at room temperature

(1) Example of co-reduction with lithium naphthalide.

Naphthalene (1.03 g, 8.07 mmol) was dissolved in 20 mL of DME under argon. Lithium wire (0.60 g, 8.6 mmol) was added and the contents were sonicated for 20 minutes giving a dark solution.[27] In a separate flask, $TiCl_4(THF)_2$ (0.33 g, 1.0 mmol), $FeCl_3$ (0.17 g, 1.1 mmol) and trioctylphosphine oxide (0.538 g 1.39 mmol) were dissolved in 20 mL of DME. While under sonication, the reductive solution was canulated in. This yielded a grey precipitate and a black supernatant. The supernatant was removed and the remaining solvent removed *in vacuo*. The remaining solid was placed in an 80 °C water bath *in vacuo* to sublime the remaining naphthalene, yielding a black oil.

(2) Example of co-reduction by potassium triethylborohydride

$TiCl_4(THF)_2$ (0.96 g, 2.9 mmol), $FeCl_3$ (0.47, 3.0 mmol), trioctylphosphine oxide (0.58 g, 1.5 mmol) were dissolved in 25 mL of DME. While stirring, 22 mL of $K[BEt_3H]$ solution (1.0 M in THF) was added. A gas was released and the orange solution turned black. Stirring was continued for four hours. The mixture was allowed to settle giving a grey precipitate. The black supernatant was canulated to a new flask. The solvent was removed *in vacuo* and the remaining solid dissolved in 5 mL of DME and 80 mL of pentane. The supernatant was collected and the solvent removed *in vacuo.*

2.2.3 Co-reduction of metal chlorides by alkali metals at high temperature

(3) High temperature reduction by lithium (270 °C)

$FeCl_3$ (0.49 g, 3.0 mmol) and $TiCl_4(THF)_2$ (0.995 g, 3.0 mmol) were dissolved in 10 mL of tetraglyme and 1 mL of oleylamine. A piece of Li wire was added (0.11 g). The solution was heated to ~180 °C upon which time the Li wire melted and the solution turned black. Heating was continued to 270 °C for 18 h. LiCl was removed as a solid by adding pentane and centrifuging.

(4) High temperature reduction by lithium (500 °C)

$FeCl_3$ (0.49 g, 3.0 mmol) and $TiCl_4(THF)_2$ (1.0 g, 3.0 mmol) and hexatriacontane (~3 g) were heated to reflux (~500 °C) under argon atmosphere. Lithium wire was added (~0.15 g) and reflux was continued for 1 h. After cooling to room temperature, particles were isolated by dissolution in pentane and the addition of water. A black film formed at the solvent interface which was separated and dissolved in THF.

2.2.4 Thermal decomposition of organometallic precursors

(5) Thermal decomposition of Ti CVD precursor and $Fe(CO)_5$

Bis(cyclopenadienyl)dicarbonyl titanium(II) (2.4 g, 10 mmol) was dissolved in 120 mL of benzyl ether, 30 mL of oleylamine and 30 mL of oleic acid. The solution was heated to 140 °C for 1.5 h. The solution was allowed to cool to 80 °C. $Fe(CO)_5$ (1.5 mL, 11 mmol) was added. The solution was headed to 250 °C for 16 h. Particles were isolated by precipitation and washing with methanol.

2.2.5 Compromise between thermal decomposition and reduction

(6) Thermal decomposition of $Fe(CO)_5$ on Ti clusters formed *in situ*

A flask was charged with naphthalene (0.81, 6.3 mmol), sodium chunk (excess), trioctylphosphine (2 mL) and 5 mL of DME. The mixture was sonicated for 1 h giving a dark green solution. The solution was canulated into a solution of $TiCl_4$ (0.41 g, 1.2 mmol) in 11 mL of DME yielding a black solution. The DME was removed *in vacuo.*

Benzyl ether (15 mL) was dried over Na and bubbled with argon for 1 h and then canulated into the titanium containing flask. $Fe(CO)_5$ (1.6 mL, 12 mmol) was added and the mixture heated to 240 °C for 20 min. After cooling to room temperature, the particles were isolated by repetitive precipitations with methanol and suspensions in pentane.

(7) Thermal decomposition of $Fe(CO)_5$ on commercial Ti clusters

Ti clusters (125 mg, ~0.84 mmol) and $Fe(CO)_5$ (0.30 mL, 2.3 mmol) were dissolved in 1 mL of trioctylphosphine and 20 mL benzyl ether. The solution was heated to 185 °C for 16 h. The particles were isolated by repetitive precipitations with methanol and suspensions in diethyl ether.

2.3 Results and Discussion

2.3.1 The Measurement of synthetic success

Titanium species tend to be very oxophillic[28] thus making the preparation and characterization of nanoparticles difficult.[29] Also, as will be seen in Chapter 3, iron particles below ~8 nm completely oxidize to form iron oxide nanoparticles under ambient conditions. The facile oxidation of these metals as nanoparticles makes characterization challenging.

Although air-excluding capillary X-ray diffraction (XRD) can be performed on-site, many of the syntheses produce salts as a by-product (*e.g.*, KCl) which in XRD and Selected Area Electron Diffraction (SAED) produce very strong reflections. These reflections from salt impurities in the isolated product often dominate the weak, broad reflections expected for nanoparticles.[30] Also, under the copper X-ray source in the XRD at our disposal, iron fluoresces producing a large background signal which also hinders the identification of nano-crystalline phases.

Instead, we use Transmission Electron Microscopy (TEM) and the associated techniques for primary characterization. The TEM at our disposal did not allow for the introduction of samples without exposure to air, so the identification of FeTi directly in the electron microscope by SAED was unlikely. Instead, there were several indicators, listed below, by which we decided to judge as indirect confirmation of the preparation of FeTi either as an alloy or core-shell nanoparticles.

1) the presence of both iron and titanium by Energy Dispersive X-Ray Spectroscopy (EDS)

2) the presence of individual particles and only one type of particles by TEM

3) SAED or XRD confirmation of $FeTiO_3$ (ilmenite) crystalline phase or other iron-titanium oxides[31, 32]

4) the presence of core shell nanoparticles to indicate the seeded growth of one metal onto another

2.3.2 Co-reductions of metal chlorides at room temperature (**1** and **2**)

The Kroll process is an industrial method for the formation of Ti metal from $TiCl_4$. In essence, $TiCl_4$, which can be purified by distillation, is reduced by sodium metal.[28] Although co-reductions of $FeCl_3$ and $TiCl_4(THF)_2$ in solution by Na, Li, and K were attempted, the reactions proved to be prohibitively slow at room temperature. In solution and below the melting points of the alkali metal, it was more convenient to use solvated alkali as a naphthalide complex. Much more reactive solutions were prepared of sodium naphthalide, lithium naphthalide or potassium naphthalide. The naphthalides have the advantage over trialkyl borohydride reducing agents (*vide infra)* that the byproduct of the reduction – naphthalene – is readily sublimed from then reaction products under vacuum while heating. Co-reductions were attempted using these reducing agents.

DME was chosen as a solvent as it is sufficiently polar to dissolve the metal chlorides and was known to allow the facile synthesis of alkali naphthalides.[27] THF was abandoned as a solvent as it was found to ring-open polymerize from the high concentration of the Lewis-acidic titanium tetrachloride.[33, 34]

Both of the two known solution syntheses of titanium nanoparticles involve reduction by triethylborohydride salts (*e.g.*, $K[BEt_3H]$).[29, 35, 36] We also attempted co-reductions of iron and titanium chlorides by potassium triethylborohydride. The common reducing agent $NaBH_4$ does not form Ti metal. Instead, $Ti(BH_4)_3(DME)$ forms, which can decompose to give TiB_2. [37]

Many iterations of these reductions were attempted using different surfactants (oleylamine, oleic acid, cetyltrimethylammonium bromide, trioctylphosphine oxide, trioctylphosphine, and combinations thereof) and changing the order that the iron and titanium precursors were reduced. Low temperature co-reductions of iron and titanium salts, regardless of reductant or surfactant choice, gave solids that did not appear to be isolated nanoparticles by TEM. EDS indicated the presence of both iron and titanium, yet the ratio was inconsistent between samples (Appendix A). SAED produced reflections characteristic of the salt byproduct such as KCl, NaCl or LiCl (Figure 2-3b).

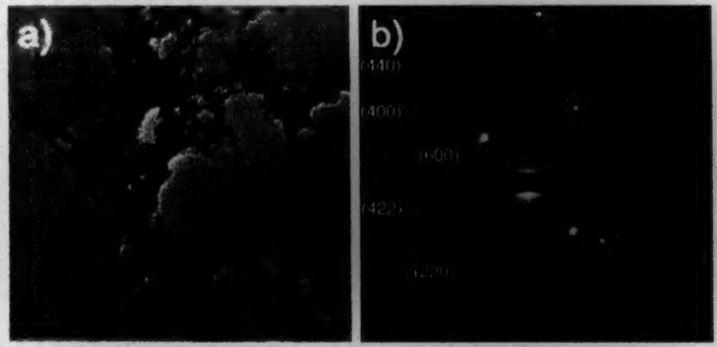

Figure 2-3 a) Representative TEM of the product of a co-reduction of iron(III) and titanium(IV) chlorides b) Example SAED of the product indexed to reflections characteristic of KCl.[38]

2.3.3 Co-reduction of metal chlorides at high temperature (**3** and **4**)

Alloying of the iron and titanium afforded by reduction was attempted by using a high boiling solvent, tetraglyme. Li wire was added at room temperature but does not melt until 180 °C, delaying reduction until that temperature. The solution-borne particles were annealed at reflux (280 °C) for 18 h. Reduction was also attempted at ~500 °C using a hexatriacontane as a solvent. At reflux, Li wire was added and the mixture was allowed to reflux for 1 h.

Particles were isolated from these reactions (Figure 2-4a), but the EDS indicated only the presence of iron (Appendix A). Titanium was not observed. The particles showed weak SAED reflections characteristic of $Fe_3O_4/\gamma\text{-}Fe_2O_3$ (Figure 2-4b). It is likely the titanium precursor was lost as volatile $TiCl_4$ and is therefore missing from the product.

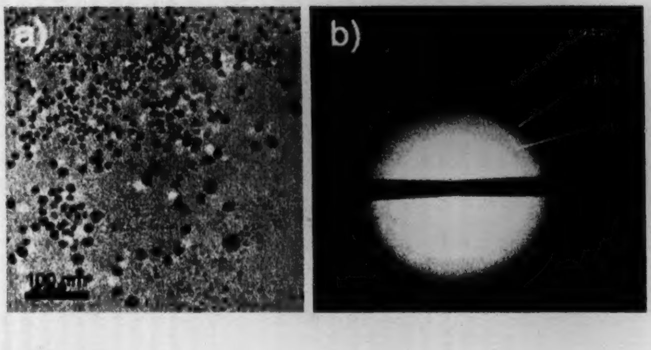

Figure 2-4 a) TEM of particles isolated from the high temperature reduction of iron and titanium chlorides. b) SAED indexed to γ-Fe_2O_3 (may also be Fe_3O_4)

2.3.4 Thermal decomposition of organometallic precursors (**5**)

One of the most notable synthesis of intermetallic nanoparticles employed organometallic precursors that were thermally decomposed to yield monodisperse FePt particles.[18] A thermal decomposition was also desired as it would provide a relatively clean synthesis; the products would not be contaminated with salts which had previously hampered characterization. $Fe(CO)_5$ is a well established (however incompletely understood, see Chapter 3) thermal precursor for forming iron nanoparticles.[39, 40] We sought organometallic Ti(0) species which could thermally decompose to yield titanium metal. Very few Ti(0) species grace the literature,[41-44] and some of those require unrealistic synthetic procedures for a large synthesis.[44, 45] Instead, the reported Chemical Vapour Deposition (CVD) precursor for Ti(0) films, bis(cyclopenadienyl)dicarbonyl titanium(II) ($Cp_2Ti(CO)_2$), was employed. Unfortunately, the temperature for complete decomposition of this precursor is greater than 1000 °C.[46] Since the presence of another metal, iron, left the possibility for catalyzed decomposition, thermal decompositions at 300 °C were attempted.

TEM combined with EDS indicated an amorphous titanium-containing material and sintered iron enriched nanocubes of ~20-70 nm were present (Figure 2-5a) (Appendix A). The nanocubes were highly crystalline and gave reflections characteristic of $Fe_3O_4/\gamma\text{-}Fe_2O_3$ (Figure 2-5b). This indicates the titanium precursor likely did not decompose under these experimental conditions, and the titanium areas in the TEM are a result of ambient oxidation of the molecular species to amorphous titania (TiO_2).

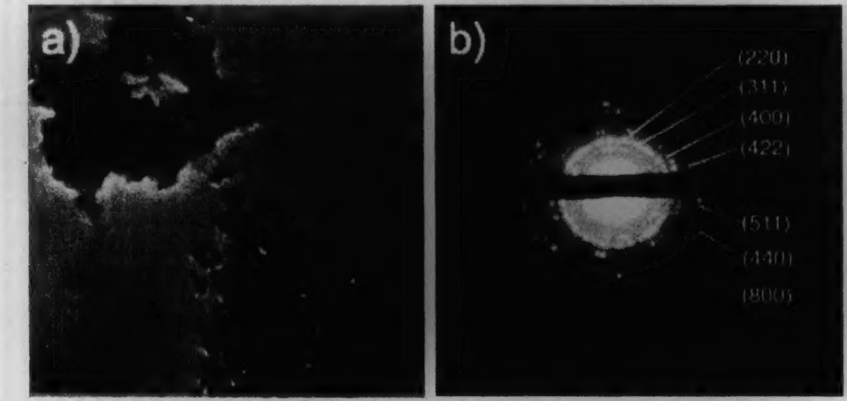

Figure 2-5 a) TEM of the material formed from the thermal decomposition of $Fe(CO)_5$ and $Cp_2Ti(CO)_2$ b) SAED of the cube structures and indexed to $\gamma\text{-}Fe_2O_3$ (may also be Fe_3O_4)

2.3.5 Compromise between thermal decomposition and reduction (**6** and **7**)

Since the titanium precursor was the Achilles' heel of the thermal decomposition route, a compromise was reached. Ti clusters were prepared *in situ* by reduction of $TiCl_4(THF)_2$ followed by the addition of $Fe(CO)_5$ and a thermal decomposition step. This compromise was also attempted by the thermal decomposition of $Fe(CO)_5$ in the presence of commercially available titanium clusters. In this way, we hoped to observe isolated core-shell particles.

When $Fe(CO)_5$ was decomposed in the presence of titanium clusters formed *in situ* or commercial titanium clusters, dark particles on a lighter support were observed by TEM (Figure 2-6a). EDS indicated both the presence of iron and titanium (Appendix A). SAED indicated the presence of $F_3O_4/\gamma\text{-}Fe_2O_3$ crystalline phase (Figure 2-6b). From this we infer the material formed after ambient oxidation is amorphous titania with iron oxide nanoparticles. This indicates the iron did not nucleate onto existing titanium clusters.

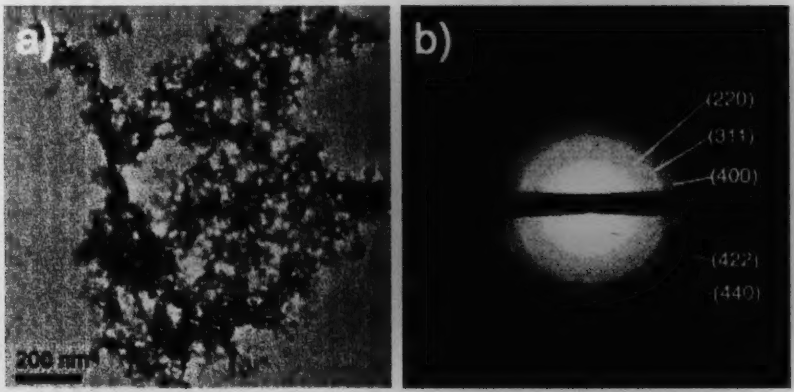

Figure 2-6 a) TEM of materials formed by the thermal decomposition of $Fe(CO)_5$ in the presence of titanium clusters b) SAED indexed to $\gamma\text{-}Fe_2O_3$ (may also be Fe_3O_4).

2.3.6 A global discussion and future possibilities

In almost all samples, there was observed spatial separation of titanium and iron containing materials on the TEM grid. We did not observe spatially separated nanoparticles that were one phase or core-shell. The ilmenite crystal phase or other iron titanium oxides were not observed for any synthesis, however Fe_3O_4/γ-Fe_2O_3 was observed for high temperature reductions and thermal decompositions. By the nature of indirect indicators of success, there are several explanations for these results. One must concede the possibility of the successful syntheses of FeTi nanoparticles, but the oxidation of the materials caused phase separation and sintering. However, given the evidence, this is not thought to be likely. Instead, these results are indicative of iron and titanium species that form as separate phases in the reaction, instead of the desired FeTi nanoparticles.

The general lack of success provides an interesting point of discussion. As stated earlier, these experimental procedures are logical extensions of successful synthetic techniques for late transition and main group metal alloy and intermetallic nanoparticles.[11] The key difference is that titanium is an early transition metal.

Phase diagrams indicate phases present often after the cooling of a melt.[19] Since FeTi is an intermetallic, it consequently represents a local thermodynamic minimum. In fact, FeTi has the strongest interatomic bond strength of all of the intermetallics with the CsCl structure.[7] However, phase diagrams do not indicate activation energies for the formation of such phases. A phase that forms from the melt at 1316 °C (Figure 2-1) may have an activation energy for formation requiring temperatures well above those readily available to a solution chemist. Beyond activation energies, the phases achieved though the cooling of a melt, are not necessarily the phases achievable through chemical processes with additional complicating factors such as solvent, differing reaction rates, solution solubility of precursors, increased surface energy, *etc.*

It is likely the crystal structure mismatch between α-Fe (bcc) and α-Ti (hcp) prevents epitaxial growth of one metal onto another; it reasonable there is a thermodynamic or kinetic advantage to forming two phases under these conditions. Since similar problems have been overcome in other alloy systems, this barrier to seeded growth must be particularly large in this system.

The promotion of the formation of bcc titanium is likely key to the future success of forming the CsCl structured FeTi nanoparticle intermetallic. Although reductions of salts at 500 °C were attempted to achieve the high temperature phase, the titanium precursor was lost through evaporation. A different, less-volatile precursor may yet prove this strategy successful.

To avoid the high temperatures required for prodding titanium to adopt its β form, the synthesis of ternary alloys may be advantageous. For example, at only a few weight percent, ruthenium will cause titanium to become bcc at temperatures lower than 200 °C.[47] Perhaps the addition of trace ruthenium to reaction mixtures will provide a back-door route to synthesizing FeTi alloy nanoparticles in the future.

2.4 Conclusions

FeTi intermetallic nanoparticles were not achieved through the chemical methods employed here. These involved various combinations of reductions of solutions of iron(III) and titanium(IV) chlorides and thermal decompositions the precursors $Fe(CO)_5$ and $Cp_2Ti(CO)_2$. These techniques are extensions of some already proven to be successful for late transition metal alloys. The structural mismatch between bcc α-Fe and hcp α-Ti preventing the seeded growth of one metal onto another, is indicated as a possible reason for the lack of success.

2.5 References

1 H. Okamoto, *Journal of Phase Equilibria,* 1996, **17**, 369-369.
2 L. Schlapbach, *Mrs Bulletin,* 2002, **27**, 675-676.
3 R. C. Bowman and B. Fultz, *Mrs Bulletin,* 2002, **27**, 688-693.
4 H. Aoyagi, K. Aoki and T. Masumoto, *Journal of Alloys and Compounds,* 1995, **231**, 804-809.
5 L. Zaluski, A. Zaluska and J. O. Ström-Olsen, *Journal of Alloys and Compounds,* 1997, **253**, 70-79.
6 A. Zaluska, L. Zaluski and J. O. Ström-Olsen, *Applied Physics A - Materials Science & Processing,* 2001, **72**, 157-165.
7 G. N. Kamm, *Physical Review B,* 1975, **12**, 3013-3022.
8 L. Sun, H. Liu, D. H. Bradhurst and S. Dou, *Journal of Materials Science Letters,* 1998, **17**, 1825-1830.
9 M. Singh, Y. K. Vijay and I. P. Jain, *International Journal of Hydrogen Energy,* 1991, **16**, 485-490.
10 K. Nowakowska-Langier, K. Zdunek and M. Kopcewicz, *Vacuum,* 2005, **78**, 423-426.
11 R. Ferrando, J. Jellinek and R. L. Johnston, *Chemical Reviews,* 2008, **108**, 845-910.
12 Y. B. Lou, M. M. Maye, L. Han, J. Luo and C. J. Zhong, *Chemical Communications,* 2001, 473-474.
13 S. U. Son, Y. Jang, J. Park, H. B. Na, H. M. Park, H. J. Yun, J. Lee and T. Hyeon, *Journal of the American Chemical Society,* 2004, **126**, 5026-5027.
14 R. Raja, V. B. Golovko, J. M. Thomas, A. Berenguer-Murcia, W. Z. Zhou, S. H. Xie and B. F. G. Johnson, *Chemical Communications,* 2005, 2026-2028.
15 S. W. Han, Y. Kim and K. Kim, *Journal of Colloid and Interface Science,* 1998, **208**, 272-278.
16 S. H. Zhou, B. Varughese, B. Eichhorn, G. Jackson and K. McIlwrath, *Angewandte Chemie-International Edition,* 2005, **44**, 4539-4543.
17 M. Zubris, R. B. King, H. Garmestani and R. Tannenbaum, *Journal of Materials Chemistry,* 2005, **15**, 1277-1285.
18 S. H. Sun, C. B. Murray, D. Weller, L. Folks and A. Moser, *Science,* 2000, **287**, 1989-1992.
19 H. Okamoto, *Desk Handbook: Phase Diagrams for Binary Alloys*, ASM International, 2000, pp. ix-xxv.
20 A. R. West, *Basic Solid State Chemistry*, 2nd edn., Wiley, Etobicoke, 2006, pp. 408-411.
21 H. Okamoto, *Desk Handbook: Phase Diagrams for Binary Alloys*, ASM International, 2000, p. 377.
22 A. R. West, *Basic Solid State Chemistry*, 2nd edn., Wiley, Etobicoke, 2006, pp. 10, 18, 47.
23 P. Tessier, R. Schulz and J. O. Strom-Olsen, *Journal of Materials Research,* 1998, **13**, 1538-1547.
24 Y. D. Yin, R. M. Rioux, C. K. Erdonmez, S. Hughes, G. A. Somorjai and A. P. Alivisatos, *Science,* 2004, **304**, 711-714.

25 O. Koper and S. Winecki, Specific Heats and Melting Points of Nanocrystalline Materials in *Nanoscale Materials in Chemistry*, K. J. Klabunde, John Wiley and Sons Inc. , Toronto, 2001, pp. 263-277.

26 P. M. Hamilton, R. McBeth, W. Bekebrede and H. H. Sisler, *Journal of the American Chemical Society*, 1953, **75**, 2881-2883.

27 S. Ji, L. B. Gortler, A. Waring, A. Battisti, S. Bank, W. D. Closson and P. Wriede, *Journal of the American Chemical Society*, 1967, **89**, 5311-5312.

28 F. A. Cotton and F. Wilkinson, *Advanced Inorganic Chemistry*, Wiley, Toronto, 1988, pp. 652-665.

29 D. Ghosh, S. Pradhan, W. Chen and S. W. Chen, *Chemistry of Materials*, 2008, **20**, 1248-1250.

30 M. F. Toney, X-Ray Diffraction in *Encyclopedia of Materials Charaterization*, eds. C. R. Brundle, J. Charles A. Evans and S. Wilson, Butterworth-Heinemann Manning, Toronto, 1992, pp. 207-208.

31 M. L. Trudeau, L. Dignard-Bailey, R. Schultz, P. Tessier, L. Zaluski, D. H. Ryan and J. O. Ström-Olsen, *Nanostructured Materials*, 1992, **1**, 475-464.

32 S. Itoh, T. Azakami, A. Kikuchi and T. Nagasaka, *Metals Materials and Processes*, 2003, **15**, 95-110.

33 P. A. Delaney, R. A. W. Johnstone and I. D. Entwistle, *Journal of the Chemical Society-Perkin Transactions 1*, 1986, 1855-1860.

34 M. Kucera, A. Zahradnickova and K. Majerova, *Polymer*, 1976, **17**, 528-534.

35 R. Pranke, J. Rothe, J. Pollmann, J. Hormes, H. Bonnemann, W. Brijoux and T. Hindenburg, *Journal of the American Chemical Society*, 1996, **118**, 12090-12097.

36 H. Bonnemann, W. Brijoux, R. Brinkmann, R. Fretzen, T. Joussen, R. Koppler, B. Korall, P. Neiteler and J. Richter, *Journal of Molecular Catalysis*, 1994, **86**, 129-177.

37 S. E. Bates, W. E. Buhro, C. A. Frey, S. M. L. Sastry and K. F. Kelton, *Journal of Materials Research*, 1995, **10**, 2599-2612.

38 H. E. Swanson and E. Tatge, *Journal of Research of the National Bureau of Standards*, 1951, **46**, 318-327.

39 T. Hyeon, *Chemical Communications*, 2003, 927-934.

40 S. Peng, C. Wang, J. Xie and S. H. Sun, *Journal of the American Chemical Society*, 2006, **128**, 10676-10677.

41 J. E. Ellis, S. R. Frerichs and B. K. Stein, *Organometallics*, 1993, **12**, 1048-1057.

42 K. M. Chi, S. R. Frerichs, B. K. Stein, D. W. Blackburn and J. E. Ellis, *Journal of the American Chemical Society*, 1988, **110**, 163-171.

43 S. R. Frerichs, B. K. Stein and J. E. Ellis, *Journal of the American Chemical Society*, 1987, **109**, 5558-5560.

44 M. D. Spencer, S. R. Wilson and G. S. Girolami, *Organometallics*, 1997, **16**, 3055-3067.

45 F. W. Benfield, M. L. H. Green, J. S. Ogden and D. Young, *Journal of the Chemical Society-Chemical Communications*, 1973, 866-867.

46 L. Valade, R. Choukroun, C. Danjoy, B. Chansou, D. De Caro and P. Cassoux, *Annales De Chimie-Science Des Materiaux*, 1998, **23**, 721-732.

47 N. G. Boriskina and Kornilov, II, *Russian Metallurgy*, 1976, 162-165.

Chapter 3: Size control of iron and iron oxide nanoparticles from the decomposition of $Fe(CO)_5$[*]

3.1 Introduction

Monodisperse iron and iron oxide nanoparticles in the 4-20 nm range have undergone a flurry of research in the last 10 years. Although synthesis, size control and characterization dominated the first 5 years,[1, 2] research is now pushing toward application-based research with a predominant focus on biomedical applications. [3, 4]

Iron and iron oxides nanoparticles are of interest to the medical community because of their magnetic properties, small size, and low toxicity.[5] Below 50 nm, particles have long sedimentation rates under physiological conditions and will not be easily excreted by the body.[5] Their small size allows for facile travel within the body so their magnetic properties can be exploited.[4] Researchers commonly cap particles with silica [6] or polymers[4] to make them bio-inert and/or bio-compatible and further modify the surfaces with bio-functionality to target particle placement within tissue.[3] The bio-application nearest commercial employment as MRI contrast agents.[4] The magnetic particles lower T_2 relaxation times of nearby protons and therefore aid contrast in the nearby tissue.[4]

---

[*] Reproduced in part with permission from J. E. Macdonald, C. J. Brooks and J. G. C. Veinot, *Chemical Communications* 2008, 3777 - 3779. Copyright 2008 The Royal Society of Chemistry.

In the size regime of interest, *i.e.*, below 10 nm, iron and iron oxide particles have a single magnetic domain and exhibit superparamagnetic behviour. That is to say, they have no hysteresis in their magnetization *versus* applied field curves, and their saturation magnetization is very high. However, strongly binding surfactants to the surfaces of particles reduce the values of the saturation magnetizations, and for smaller particles with a larger surface to volume ratio, this depression in magnetization is even more pronounced.[2] Therefore, for applications which exploit the superparamagnetic properties of iron and iron oxide nanoparticles, such as MRI contrast agents, it is advantageous to have particles as large as possible without losing their superparamagnetic properties.[6] This transition typically occurs for iron and iron oxide particles at diameters of ~10-20 nm. [2, 5] It is likely for this reason there has been little drive for particles that push our synthetic abilities to the lower size limits.

Yet there are other applications of monodisperse iron and iron oxide nanoparticles that have not been developed to the same extent and do not rely on the magnetic properties. Carbon NanoTubes (CNTs) are grown from metal nanoparticles at high temperatures under an atmosphere of a carbon source such as methane, acetylene or carbon monoxide. CNTs can be grown off catalyst particles of many different elements, but give varying yields and qualities.[7] Iron and other first row transition metal particles give a higher concentration of single walled CNT (SW-CNT) over multiwalled CNT (MW-CNT).[8, 9] As with all current CNT syntheses, the products are a complicated mixture of SW-CNT and MW-CNT, and within those two classifications, mixtures of diameters and different "wrappings" and corresponding chirality. Each of these have individual electronic properties ranging from semiconductor to metallic, and therefore, the electronic properties of the materials are difficult to study and exploit.[8]

To study the electronic properties of CNTs effectively and control their properties, the first challenge is to develop a preparative method that gives only SW-CNTs of a single diameter. There is a direct correlation between catalyst particle size and the diameter of the CNT; SW-CNT are preferentially grown on smaller particles whereas larger particles tend to grow MW-CNT.[7-10] Metal particle catalysts for CNT synthesis are classically synthesized by the reduction of metal salts onto support materials.[9] This type of synthesis tends to give very little control over the size and size distribution of metal nanoparticles formed. As a result of this polydispersivity, both SW-CNT and MW-CNT of varying diameters are yielded. Our collaborators at Honda Research Institute Inc. have predicted monodisperse iron particle catalysts of 1.6 nm will give pure SW-CNT[11] and a reproducible, high yielding synthesis (~0.5 g) of monodisperse iron or iron oxide particles of this size will aid CNT research and development. With this goal in mind, we embarked on a journey to develop methods for achieving size control of monodisperse iron and iron oxide nanoparticles below the common 4 nm diameters already seen in the literature.[1, 2]

The general synthesis for iron and iron oxide nanoparticles involves a chemical transformation of a molecular iron source to give a species that will either precipitate out as iron or one of the iron oxides. A surfactant is used to inhibit growth of the nuclei of solids that form and thereby suppress growth beyond the nano-size regime. The chemical transformations oft studied are reduction,[12] hydrolysis[13] and energy induced decomposition of iron precursors.[1, 2] We were drawn to the thermal decomposition of iron precursors such as iron acetylacetoneate,[3] $Fe(N(SiMe_3)_2)_2$ [14] and $Fe(CO)_5$ [15] because there were already examples in the literature of these precursors yielding monodisperse particles. Iron pentacarbonyl was particularity attractive as the only predicted by-product was $CO_{(g)}$ and had already been shown to give monodisperse particles as small as 3 nm.[16]

The size control of near monodisperse iron and iron oxide nanoparticles synthesized from thermal decomposition of $Fe(CO)_5$ in high boiling point solvents and surfactants is well established, however the associated processes are extremely complex. Not only is the decomposition route complicated and ill-understood,[2, 17] many factors such as solvent and surfactant choice,[18-20] concentration ratios,[21] reaction times[19, 22] and temperature[19, 23] play important roles, thus making the system difficult to study. Recently, several research groups have attempted to separate and understand these factors to tailor particle size. Despite many modes of control, most studies have achieved sizes in the 3-20 nm range [2, 24] and very few have shown particles with average diameters below 4 nm.[16, 19] The most recent foci for attaining size control have been methods for the separation of nucleation events from growth.[22, 25] As described by the LaMer model, growth onto existing particles is thermodynamically favourable, yet nucleation is kinetically favoured when the concentration of the active species for nucleation is high.[26-28] By extension, there are two general modes of attack for achieving small particles: namely, increasing the number of nucleation events or inhibiting growth of the particles. Herein is a description of experiments into achieving particle size control upon these two fronts.

3.2 Experimental Procedures

3.2.1 Reagents

Triethylamine was purchased from Kodak, aspartic acid from Fischer Scientific and phosphoric acid from Mallinckrodt. All other reagents were purchased from Aldrich and were used without purification unless otherwise noted. Yields of nanoparticle products are not reported as the presence of surfactant hinders the acquisition of a meaningful number.

3.2.2 Control of growth in thermal decompositions of $Fe(CO)_5$

Synthesis of uncapped nanoparticles

Benzyl ether (10 mL) was bubbled with argon for 1 h in a dry reflux apparatus. After heating to 120 °C, $Fe(CO)_5$ (0.30 mL, 2.3 mmol) was added. The temperature was increased to reflux (~300 °C) for 13 h to give a black solution. Particles were isolated by the addition of pentane followed by precipitation in methanol and centrifugation.

Synthesis of oleylamine capped nanoparticles

Benzyl ether (10 mL) and oleylamine (2.5 mL, 7.6 mol) were bubbled with argon for 1 h and heated to 130 °C. $Fe(CO)_5$ (0.30 mL, 2.3 mmol) was added and the heat was increased to reflux (~300 °C) for 13 h. After cooling to room temperature, the particles were isolated by successive precipitation in methanol, centrifugation, and suspension in pentane three times.

Synthesis of TOPO capped particles

Trioctylphosphine oxide (99%) (TOPO) (5 g) was placed in a dry, argon filled reflux apparatus. $Fe(CO)_5$ (0.30 mL, 2.3 mmol) was added. The mixture was heated to 200 °C for 2.5 h upon which the solid had melted and the solution turned black. Cooling to room temperature gave a black solid. Excess TOPO was dissolved in acetone and the solution centrifuged to give a black precipitate.

Synthesis of oleic acid capped particles with triethylamine

Benzyl ether (10 mL) and oleic acid (2 mL, 6.3 mmol) were bubbled with argon for 1.5 h. Triethylamine (distilled and stored over KOH) (0.5 mL, 3.6 mmol) and $Fe(CO)_5$ (0.30 mL, 2.3 mmol) were added and the temperature was increased to 190 °C for 16 h. After cooling to room temperature, the particles were isolated by successive precipitation in methanol and suspension in pentane five times.

Synthesis of *N*-lauroylaspartic acid (**6**) [29, 30]

A solution of DL-aspartic acid (**4**) (0.79 g, 5.9 mmol) and sodium carbonate (2.58 g, 24 mmol) was prepared in 100 mL of deionized water. A solution of lauroyl chloride (**5**) (1.4 mL, 6 mmol) in THF (50 mL) was prepared and added to the aqueous solution. The solution was stirred for 2 h, then acidified with 1 M HCl. The product was extracted 3× with ethyl acetate and the solvent removed *in vacuo*. The product was purified by silica column chromatography. The impurities were eluted with 5% dichloromethane in hexanes. The major product was then eluted with 5% acetic acid in ethyl acetate. Solvents were removed under reduced pressure yielding *N*-lauroylaspartic acid (**3**) (0.95 g, 51% yield) ^{1}H NMR (300 MHz, DMSO-D$_6$): δ 12.4 (s), 8.07 (1H, d), 4.50 (1H, m), 2.60 (2H, m), 2.07 (2H, t), 1.45 (2H, t), 1.20-1.27 (16H, m), 0.85 (3H, t).

Synthesis of *N*-laurolyaspartic acid capped particles

Benzyl ether (3.3 mL) and *N*-lauroyl aspartic acid (0.66 g, 2.1 mmol) were bubbled with argon for 1 h. $Fe(CO)_5$ (0.10 mL, 0.77 mmol) was added and the solution heated to 182 °C for 16 h under argon. After returning the solution to room temperature, particles were isolated by several successive precipitations in methanol and suspensions in pentane.

3.2.3 *Synthesis of oleic acid capped particles and promotion of nucleation by water*

A stock solution of 5:1 (volume) benzyl ether and oleic acid (90%) was prepared. Water was added to ~60 mL aliquots of this stock solution and the water concentration was determined by Karl Fischer titrations. The lowest concentrations of water were achieved by drying the aforementioned solvent/surfactant mixture over $MgSO_4$ or by vacuum distillation of the benzyl ether over Na prior the preparation of the solvent/surfactant mixture. In a typical reaction, the surfactant/solvent mixture was bubbled for 1 h with argon. Using standard Schlenk techniques, 10 mL of the solution

(5.3 mmol oleic acid) was transferred into a dry, argon flushed reflux apparatus. $Fe(CO)_5$ (0.30 mL, 2.3 mmol) was added. Heat was applied at a controlled rate such that the temperature equilibrated at ~200 °C after 1 h (Figure 3-1).

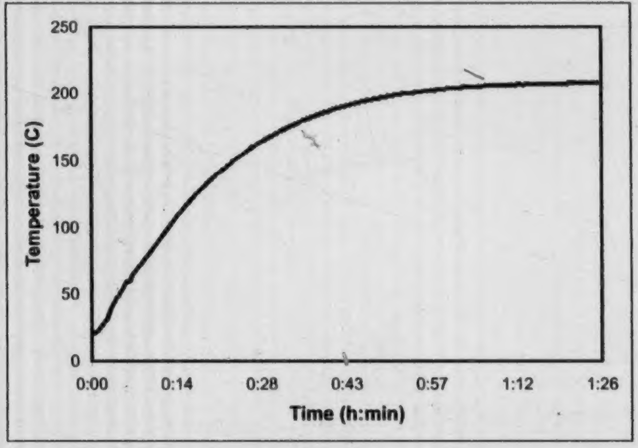

Figure 3-1 Example heating curve of sand bath.

The reaction mixture remained at 192-217 °C for 16 h upon which time the yellow solutions had turned black. Multiple experiments were performed for each concentration of water. Particles were isolated by repetitive precipitation with methanol and dissolution with tetrahydrofuran.

TEM was performed and the diameters of 85-200 particles were measured per sample. For repetitive experiments at identical water concentrations, the data sets were treated to ANalysis Of VAriation (ANOVA) (single factor) to confirm differences in the populations. Further ANOVA over the different water concentration was performed to confirm differences in the populations and a Tukey post test were preformed (see Appendix B).

3.2.4 *Avoiding the slow temperature gradient by hot introduction of* $Fe(CO)_5$

Liquid introduction of $Fe(CO)_5$ into hot solvent/surfactant

A mixture of octyl ether (50 mL) and oleylamine (1.1 mL, 3.3 mmol) were bubbled with argon for 2 h in a 500 mL three neck flask affixed with a condenser and then heated to ~290 °C. Another 10 mL of octylether was bubbled with argon for ½ hour and $Fe(CO)_5$ (0.30 mL, 2.3 mmol) was added. This solution was taken up in a syringe and added to the hot reaction mixture. The solution turned black and was allowed to cool to room temperature. The particles were collected by several successive precipitations in methanol and suspensions in pentane.

Gas phase introduction of $Fe(CO)_5$ into hot solvent/surfactant

A two neck flask with a condenser was loaded with ~3 g of TOPO or ~3 mL of octylether and heated to 280-300 °C under argon atmosphere. In a separate flask, 0.7-0.9 mL of $Fe(CO)_5$ was added and bubbled with argon while in a warm water bath (~60 °C). A polytetrafluroethylene (PTFE) canula connected the head space of this flask to below the liquid line of the hot TOPO/octylether-filled reflux apparatus. The top of the reflux apparatus was opened to the atmosphere by way of a septum and needle. By this method, gaseous $Fe(CO)_5$ was introduced into the hot liquid with argon as a carrier gas. The solution turned black, the flow of gasses was arrested, and the reaction flask returned to room temperature giving a black solid. Particles were isolated by the addition of acetone or 95% ethanol respectively and centrifugation to give a black precipitate.

3.2.5 Sonochemical decomposition

Sonication experiments were performed using a Misonix 3000 Sonicator with a sapphire tip or titanium micro tip as indicated.

Sonochemical synthesis with oleic acid

a) Benzyl ether (50 mL) and oleic acid (6 mL) were mixed and bubbled with argon for 30 min. $Fe(CO)_5$ (0.70 mL, 5.2 mmol) was added. Under an argon blanket, the solution was sonicated with a sapphire tip for 20 min (on time) with 1 s, ~18 W pulses and 1 s rest times. The solution was observed to turn black within 20 seconds. Particles were isolated by the addition of ethanol followed by centrifugation.

b) Oleic acid (50 mL) and $Fe(CO)_5$ (0.80 mL, 6.1 mmol). Procedure as before.

Sonochemical synthesis with oleylamine

Benzyl ether (12 mL) and oleylamine (0.55 mL) were bubbled with argon for 60 min. $Fe(CO)_5$ (0.30 mL, 2.3 mmol) was added. Under an argon blanket, the solution was sonicated with a sapphire tip for 10 s (on time) with 1 s, ~18 W pulses and 1 s rest times giving a black solution. Particles were isolated by the addition of methanol followed by centrifugation.

Sonochemical synthesis with TOPO

TOPO (80 mg) was dissolved in benzyl ether (12 mL) and bubbled with argon for 30 min. $Fe(CO)_5$ (0.30 mL, 2.3 mmol) was added and 2.0 mL aliquots taken to ~4 mL vials.

Under an argon blanket and using a Ti micro-tip, the solution was sonicated with 1 s pulses of ~15 Watts, 3 s rest times.

a) 20 s (on time) The yellow solution turned dark yellow. Particles were isolated by the addition of methanol followed by centrifugation.

b) 2.5 min (on time) The yellow solution turned much darker, but was not opaque. Particle were isolated by the addition of methanol followed by centrifugation.

3.2.5 Details of instrumentation and characterization

Gas Chromatography- Mass Spectroscopy (GCMS) was performed on a Waters 7070E GC-MS using electron ionization. 1 μL of a dichloromethane solution of the product was injected into a Phenomenex ZB-5, 30 m x 0.25 mm column with a 0.35 μm film. The carrier gas was helium at 1 mL/min. The injection port was at 275 °C and a linear temperature profile (50-300 °C at 10 °C / minute) was employed.

Fourier Transform Gas Phase Infra Red Spectroscopy was performed on a Magna System 750 IR using Omnic 7.1 software. The cell had a 10 cm path length with KBr windows. 32 scans were performed. The cell was flushed with argon and the area around the cell was flushed with N_2 gas until the CO_2 absorbance was at a minimum. This spectrum was used as a background. Acquisition of the spectrum of the reaction gases were handled similarly; the area around the cell was flushed with N_2 gas until the CO_2 absorbance was at a minimum. From this the aforementioned background spectra was subtracted.

Transmission Electron Microscopy samples were prepared by suspending particles in tetrahydrofuran and drop-coating the solution on carbon coated, 200 mesh Cu grid (SPI Supplies) under ambient conditions. Samples were predominately evaluated using a JEOL 2010 Transmission Electron Microscope (TEM) at 200 keV accelerating voltage and a LaB_6 filament. Systematic error in particle size measurements is less than 3%.

Some samples were imaged using a Tecnai G2 Spirit TEM at 120 keV accelerating voltage and a LaB_6 filament. Images produced from this instrument are noted as (Tecnai TEM) in the figure captions.

3.3 Results and Discussion

3.3.1 Studies into suppressing growth of iron nanoparticles.

The use of surfactants is a common technique for inhibiting the growth of particles. In principle, the stronger the interaction of the head group with the particle surface, the smaller the diameters of the particles synthesized.[1, 19, 31] To confirm this prediction, studies were performed with surfactants of varying head groups: carboxylic acid, amine and phosphine oxide (Scheme 3-1).

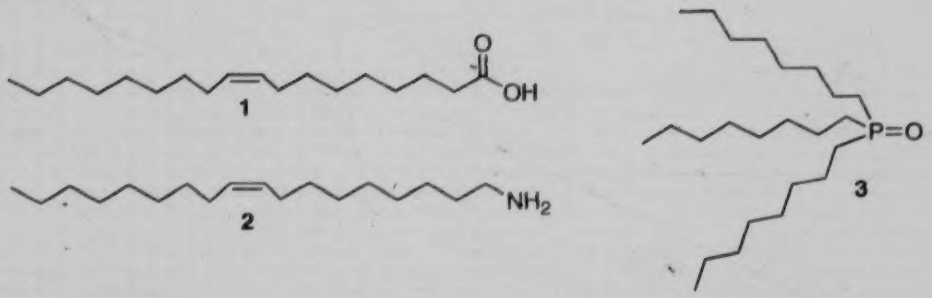

Scheme 3-1 Surfactants employed for study of size controlled synthesis of iron/iron oxide nanoparticles: oleic acid (**1**), oleylamine (**2**), and trioctylphosphine oxide (TOPO) (**3**)

Without surfactant, the thermal decomposition of $Fe(CO)_5$ in benzyl ether gave a polydisperse mixture of particles (Figure 3-2a). Particles ranged in diameter from ~2 nm up to ~15 nm. The presence of so many ~2 nm particles indicates the decomposition of $Fe(CO)_5$ in the absence of surfactant was rapid leading to many nucleation events and small particles. The larger particles indicate growth onto existing particles and/or Ostwald ripening processes. From this it was inferred both nucleation and growth processes are relatively uninhibited when surfactant is not present.

Since carboxylic acids have very strong affinities for iron and iron oxide surfaces, as predicted, the use of oleic acid as a surfactant gave small, monodisperse particles with diameters of 5.6 ± 0.5 nm ($n = 158$) consistent with the literature (Figure 3-2b) (Appendix B).[1, 18, 31] Since there are no large (*i.e.*, diameters above 8 nm) particles like those of the surfactantless system, oleic acid therefore inhibits growth on nucleated particles. The use of a more weakly interacting surfactant, oleylamine [32-34] yielded particles which were larger and more polydisperse with diameters of 8.5 ± 2.0 nm ($n = 76$) (Figure 3-2c) (Appendix B).

Figure 3-2 Iron oxide nanoparticles from the thermal decomposition of $Fe(CO)_5$ in benzyl ether and a) no surfactant b) oleic acid d = 5.6 ± 0.5 nm (n = 158) c) oleylamine d = 8.5 ± 2.0 nm (n = 76)

The decomposition of $Fe(CO)_5$ in high boiling solvents is known to give Fe(0) nanoparticles,[31] however subsequent oxidation in ambient conditions necessary for TEM characterization gave crystalline γ-Fe_2O_3 nanoparticles (Figure 3-3) under the aforementioned conditions.[25]

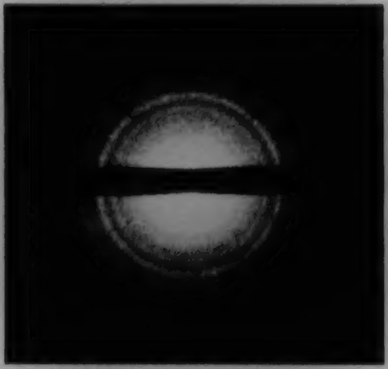

Figure 3-3 Representative Selected Area Electron Diffraction (SAED) of particles showing characteristic reflections of γ-Fe_2O_3.[19]

However, Selected Area Electron Diffraction (SAED) indicated amorphous particles were achieved when the surfactant was changed to trioctylphosphine oxide (TOPO). TOPO is expected to have an even weaker interaction with iron surfaces than oleylamine and therefore is predicated to give even larger particles. At first glance, the TEM images confirm the size prediction (Figure 3-4); large particles were noted with diameters of 11.8 ± 4.4 nm (n = 119) that were large enough to exhibit core-shell Fe@Fe_xO_y characteristics upon exposure to air (Appendix B). The shells of the core-shell particle formed were 3.2 ± 0.6 nm (n = 137) thick. This is consistent with the general observation throughout this study that particles below ~ 8 nm (near twice the shell thickness) are completely oxidized in air and do not appear to be core-shell by TEM.

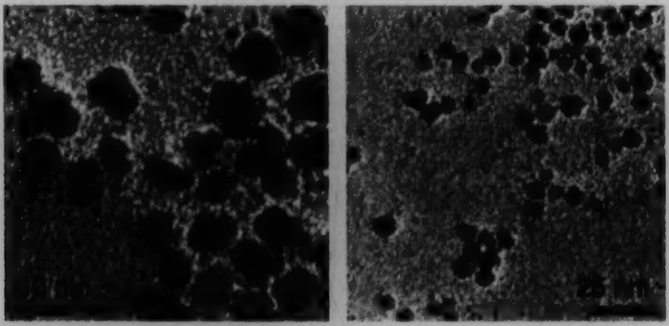

Figure 3-4 Particles formed from the decomposition of $Fe(CO)_5$ in the presence of TOPO

Upon closer inspection of the TEM images, we noted a second, much smaller, set of particles with diameters of 3.0 ± 0.6 nm (n = 80) (Appendix B). Two separate size distributions have also been observed for Ni particles and rods synthesized from the hydrogenation of $Ni(COD)_2$ in the presence of TOPO, by Cordente *et al.*, but an explanation was not provided.[35]

The observations of two distinct size distributions are not indicative of the Ostwald ripening processes (without distinctly time-separated nucleation events, which is not the case here).[36] Instead, this can be explained by a difference in chemical identity between the two particle sizes formed, and may be from the direct formation of metal and metal oxide nanoparticles respectively. The direct formation of two chemically different materials will therefore have differing interactions with the surfactant, nucleation and growth processes effecting eventual particle size. Trioctylphosphine oxide is known to have acid impurities such as H_3PO_4 which may act as an oxidant for the formation of the smaller particles. Indeed, the addition of 5 μL of phosphoric acid to the reaction gave almost exclusively small particles. Cordente, *et al.*, indicated the concentration of the smaller particles increased with higher concentration of TOPO and the $^{31}P\{^1H\}$ NMR did not show any presence of phosphine indicating TOPO itself is not the oxidant.[35] Their results are also consistent with the hypothesis of oxidative impurities in the surfactant.

Having observed the smallest monodisperse particles with oleic acid as a surfactant (without the complication of the addition of a direct oxidant such as the previous case), attempts were made to increase the strength of the interactions between the surfactant acid head groups and the particle surfaces to achieve even smaller particles. Triethylamine was added to the reaction mixture to increase the concentration of free oleate expecting the oleate to bond more strongly to the particle surfaces. However, this yielded larger than expected particles with diameters of 6.5 ± 0.8 nm (n = 164) (Figure 3-5a). This observation is consistent with a recent study on the use of different oleate salts.[18] Also, aspartic acid was *N*-acylated to give *N*-lauroylaspartic acid (**3**): a surfactant with two carboxylic acid head groups (Scheme 3-2). Instead of the expected smaller particles, a similar size was seen for those seen when oleic acid is used but with a larger polydispersivity: 5.2 ± 1.9 nm (n = 112) (Figure 3-1b). Hyeon *et al.* also noted increasing the oleic acid concentration counter-intuitively increases particle growth. They postulated that oleic acid ligates the active molecular species for particle formation as iron oleate complexes. As a result, the concentration of the active species is lower inhibiting nucleation events. The iron oleate decomposes more slowly and provides a source of iron for growth on the smaller population of nuclei formed.[31] The result is larger particles.

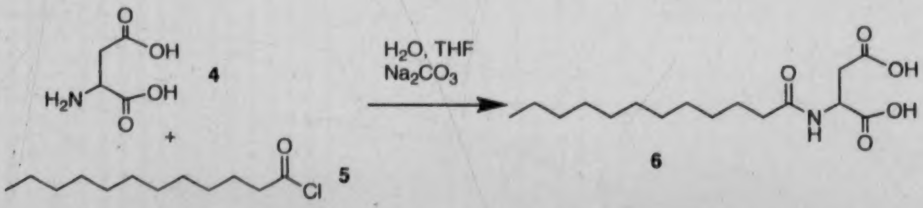

Scheme 3-2 Synthesis of *N*-lauroylaspartic acid (**6**)

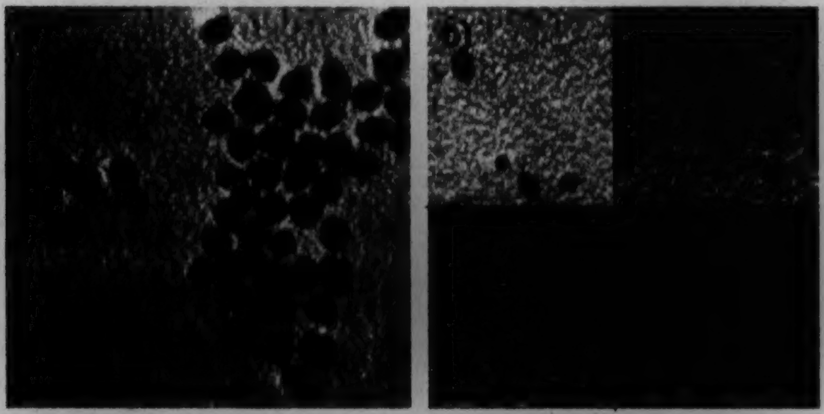

Figure 3-5 Particles from the decomposition of $Fe(CO)_5$ in the presence of a) oleic acid and triethylamine 6.5 ± 0.8 nm (n = 164) b) *N*-lauroyl aspartic acid 5.2 ± 1.9 nm (n = 112)

We suggest deprotonation of oleic acid with triethyl amine increased the nucleophilic character of the surfactant for the active iron species, and thereby decreased the number of nucleation events which dominated over the effect of the inhibition of growth. Equally, the use of two carboxyllic acid head groups in *N*-lauroyl aspartic acid only provides a chelated, more strongly ligated molecular iron species locked-up in surfactant preventing the nucleation of particles.

Formation of iron oleate has been resoundingly implicated in the literature as an inhibitor of nucleation.[1] The formation of iron-oleylamine complexes during synthesis have also been observed.[37] It is proposed that iron-oleate and iron-amine complexes are formed *in situ* and subsequently decomposed at higher temperatures.[37] The complete decomposition of $Fe(CO)_5$ in solutions containing TOPO can be observed to occur at ~120 °C within 1/2 hour whereas for the other surfactants, much higher temperatures (~170 °C) and longer reaction times (several hours) are required. Therefore, TOPO-iron complexes play less of a role in particle nucleation than iron-acid and iron amine complexes.

In summary, testing of the prevailing theory that strongly interacting surfactants with iron and iron oxide surfaces gives smaller particles– was met with varying success. This indicated that the surfactant is involved with other processes in particle formation beyond growth inhibition. There are two competing phenomena in determining particle size with surfactant. A surfactant with a strong affinity for a particle surface will inhibit growth giving smaller particles. However, the formation of surfactant-ligated iron species in the process of the decomposition of $Fe(CO)_5$ may add a layer of complication. If the surfactant also has a strong affinity for the active species that forms particles, it will lock up the iron as slow-to-decompose complexes and prevent nucleation events. The remaining iron will grow on to few nuclei that do form, and yield overall larger particles. The control of growth cannot be entirely isolated from that of nucleation by straightforward use of surfactants. Furthermore, impurities in the surfactant may produce particles that differ chemically and change the observed particle sizes. The role of impurities is often neglected. Indeed, water as an ever-present impurity in the decomposition of $Fe(CO)_5$ will prove to be surprisingly important (*vide infra*).

3.3.2 Particle size control through increasing nucleation events

The second front by which we aimed to achieve small iron or iron oxide nanoparticles from the decomposition of $Fe(CO)_5$ was to attempt to increase the number of nucleation events. The concentration of the active species for particle formation should be high and should be made so over as short a period of time as possible. The LaMer model[26, 38, 39] predicts this will cause the iron precursor to be used predominantly in nucleation events rather than in growth yielding overall smaller particles. In essence, some way should be developed to achieve very rapid and effective decomposition of $Fe(CO)_5$.

Others have used photonic techniques such as LASER pyrolysis [40-43] to achieve the same end; however, solution techniques more readily available to the traditional chemist were chosen for this study. Three general methods were examined: addition of water as a promoter to lower the activation energy of decomposition, introduction of $Fe(CO)_5$ to hot solvents and surfactants, and sonication of $Fe(CO)_5$ containing solutions.

3.3.3 Promotion of decomposition by water [44]

Catalysis or promotion of the decomposition of $Fe(CO)_5$ will provide a more rapid formation of the active species for particle formation upon heating. This in turn causes more nucleation events and smaller particles. One of the earliest reported syntheses of monodisperse iron/iron oxide nanoparticles by thermal decomposition of $Fe(CO)_5$ used polymers as "surfactants" which were shown to catalyze the decomposition. Despite the catalysis, the smallest particles reported were 6 nm.[20]

In this section, we report evidence that trace water promotes the decomposition of $Fe(CO)_5$ to increase nucleation events which leads to decreased particle size down to 2.2 nm. Water is therefore an important factor in determining the particle size.

A distinctive trend relating particle size and initial water concentration was observed (Figure 3-6, Figure 3-7). ANOVA between the different water concentrations indicated the groups are statistically different at more than 99.999% confidence. Tukey's test for multiple comparisons over the different water concentrations indicate a statistically significant decrease in particle size with water concentration (Appendix B). With a water-saturated solution (~1600 ppm), average particle sizes were as low as 2.2 nm. At much lower concentrations of water (~100 ppm), average particle sizes were as large as 5.6 nm using otherwise identical reaction conditions. The standard deviations of the particle sizes for each data set were typically below 0.6 nm (see Appendix B).

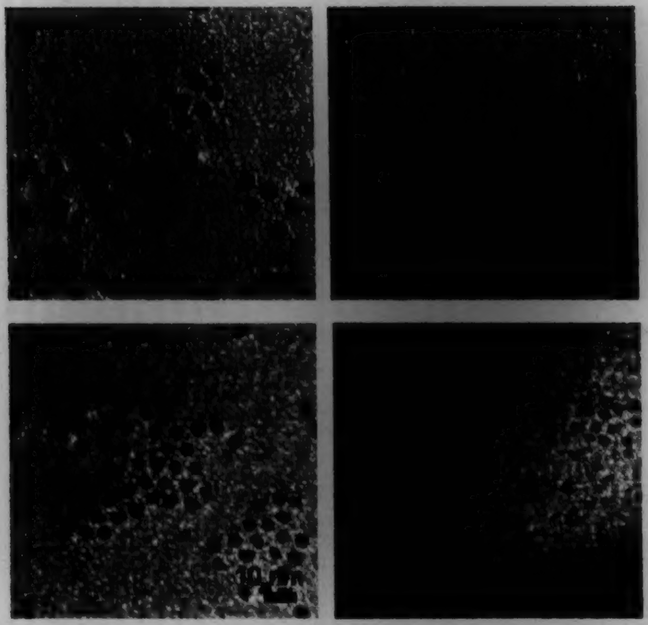

Figure 3-6 Brightfield TEM images of iron oxide nanoparticles synthesized from the thermal decomposition of $Fe(CO)_5$ in benzyl ether and oleic acid a) 101 ppm H_2O, particle diameters = 5.6 ± 0.3 nm b) 181 ppm H_2O, 4.9 ± 0.3 nm c) 657 ppm H_2O, 3.5 ± 0.2 nm d) 1590 ppm H_2O, 2.2 ± 0.1 nm

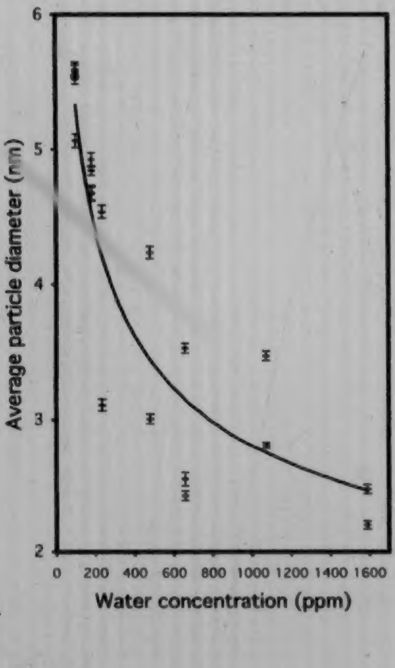

Figure 3-7 The affect of water concentration on the average particle size diameter in the thermal decomposition of $Fe(CO)_5$ to give iron oxide nanoparticles. Error bars are the standard error in the mean for each particle size distribution to highlight the differences in samples at the same water concentration. The curve is presented to guide the eye.

Several explanations for this trend were dismissed based on the literature evidence. It was possible that water was behaving as a base, to deprotonate the oleic acid to oleate making it a more strongly binding surfactant. However the addition of other bases such as short-chain amines, gave larger particles.[18] Equally, the addition of oxidants into reaction mixtures, another possible role for the water, have also given larger particles.[31] Also, two distinct sizes were not observed such as the case observed with oxidizing impurities in TOPO stabilized syntheses (Section *3.3.1*, Figure 3-4). This would have been expected if water was acting as an oxidant and much less than stoichiometric amounts of water was present, as is the present case.

Instead we propose the water becomes intimately involved in the decomposition of $Fe(CO)_5$ to afford a more rapid decomposition and thereby increases nucleation events.

$Fe(CO)_5$ is a well studied model catalyst for the water-gas-shift reaction outlined in (1),

$$H_2O + CO \xrightarrow{Fe(CO)_5} H_2 + CO_2 \quad (1)$$

The activation energy for the catalyzed reaction in (1) has been measured to 22 kcal/mol in water/methanol[45] and 19 kcal/mol in the gas phase.[46] The rate-determining step is the initial addition of water and loss of a proton to form $Fe(CO)_4COOH^-$.[45] Without CO overpressure, decarbonylation is rapid and it is not rate determining in the decomposition of $Fe(CO)_5$ under water-gas-shift conditions. Indeed, the further loss of CO from the catalyst to form polynuclear iron complexes has long been known.[47, 48]

The rate-determining step for decomposition of $Fe(CO)_5$ without water-gas-shift conditions is the first decarbonylation. This process has an activation energy near twice that of the water-gas-shift reaction at 40 kcal/mol.[48] Therefore, the presence of water lowers the activation energy for the decomposition of $Fe(CO)_5$ by near a factor of 2. Since the rate of reaction is exponentially related to the negative of activation energy by the Arrhenius equation,[49] this lowering of the activation energy markedly increases the decomposition rate to afford a higher concentration of the unidentified active species for particle formation. This, in turn, leads to more nucleation events and decreased particle size.

A log-log plot of the particle diameters, d, and water concentration gives a linear relationship (Figure 3-8) with the line equation of:

$$\begin{aligned} \log d &= -0.30\log[H_2O] + 1.3 \\ R^2 &= 0.8013 \end{aligned} \qquad (2)$$

The R^2 of 0.80 indicates a strong correlation between the two variables. The R^2 is a result of the scatter in the plot (the source of which will be discussed shortly) around an underlying linear trend.[50] The relationship can be expressed as:

$$d = 21[H_2O]^{-0.30} \qquad (3)$$

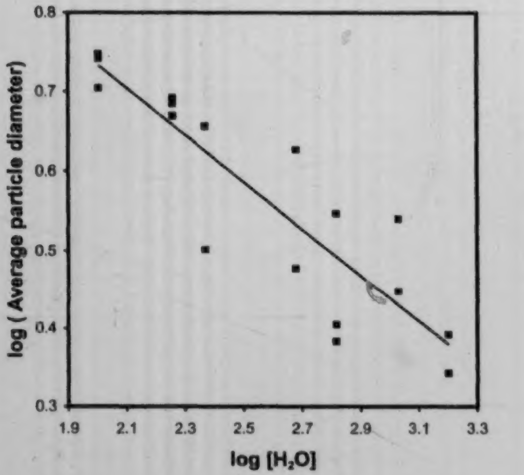

Figure 3-8 Log-log plot of water concentration and particle size giving a linear trend with the equation:

$\log d = -0.30\log[H_2O] + 1.3$

$R^2 = 0.8013$

A physical interpretation of this result is not straightforward and requires a theoretical relationship between particle volume, diameter and nucleation sites. Since the amount of $Fe(CO)_5$ in each reaction is constant, it can be assumed the total amount of iron is the same for every sample. Therefore the total volume, V_{tot}, of iron oxide is constant and can be expressed as the sum of all of the particle volumes:

$$V_{tot} = \sum_{n=1}^{n} \tfrac{4}{3}\pi\left(\frac{d_n}{2}\right)^3 \qquad (4)$$

Where n is the number of particles. Assuming our samples are monodisperse and the diameters are equal, equation (4) simplifies to:

$$V_{tot} = n\tfrac{4}{3}\pi\left(\frac{d}{2}\right)^3 \qquad (5)$$

rearrangement gives:

$$d = \frac{6}{\pi V_{tot}} n^{-\frac{1}{3}} \qquad (6)$$

Using our hypothesis that water is intimately involved in nucleation and that the concentration of water is directly proportional with the number of nuclei formed, a relationship is developed which describes the experimental results. Collecting constants as k, a theoretical relationship of:

$$d = k[H_2O]^{-\frac{1}{3}} \qquad (7)$$

results, which is consistent with our experimental exponential dependence of -0.30 (Equation 3). This further supports our hypothesis that water is involved in nucleation.

To confirm water-gas-shift processes were indeed occurring, the gases emanating from the reaction were collected and analyzed by gas phase Fourier Transform InfraRed spectroscopy (FT-IR). The influence of ambient CO_2 was minimized and subtracted: the

IR cell was flushed with argon and the area around the cell was flushed with N_2 gas until the CO_2 absorbance was a minimum. This spectrum was used as a background. Acquisition of the spectrum of the reaction gases was handled similarly; the area around the cell was flushed with N_2 gas until the CO_2 absorbance was at a minimum. From this the aforementioned background spectra was subtracted (Figure 3-9).

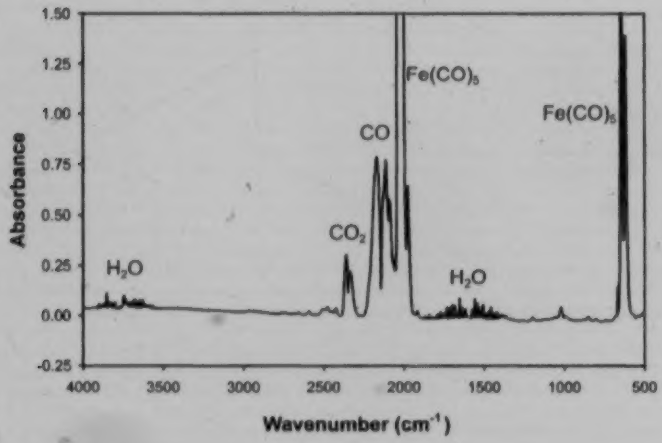

Figure 3-9 FT-IR of the gas released from the thermal decomposition of $Fe(CO)_5$ in benzyl ether and oleic acid. Peaks indicative of $Fe(CO)_5$ are off scale to allow for visualization of the other components.

FT-IR analysis confirmed four gasses released from the reaction solution: CO (R and S rotational bands at 2170 and 2115 cm^{-1}), $Fe(CO)_5$ (11 bands between 2002-2041, 644, 619 cm^{-1}), CO_2 (R and S rotational bands of the asymmetric stretch at 2360 and 2339 cm^{-1}) and water vapour (asymmetric stretching modes between 3500-3800 cm^{-1}, bending modes between 1500 and 1900 cm^{-1}).

The presence of CO is consistent with the decomposition of $Fe(CO)_5$ and the presence of CO_2 confirms water-gas-shift reactions occur despite the acidic conditions.[46] The other expected gas produced by the water-gas-shift reaction is H_2, but it could not be identified as it is not IR active. As the reaction temperatures were well above the boiling points of $Fe(CO)_5$ (bp. 103 °C)[2] and water, the presence of a very strong absorbance from $Fe(CO)_5$ and a weaker contribution from H_2O are not surprising. However, their presence indicates the concentrations of these two species in solution are somewhat variable. For this reason, efforts were made to ensure consistent heating rates and identical reaction apparatus were employed so that these effects would be systematic.

Consistent heating rates and resting temperatures were vital to the observation of the present trend. Compared to the ~1 h long heating time to reach ~200 °C (Figure 3-7), when heating took at least twice as long to reach the resting temperature much larger particles were obtained: 4.4 ± 0.5 nm at initially 1073 ppm H_2O and 4.6 ± 0.5 nm for initially 1590 ppm H_2O. Slower heating allows more substantial evaporation of H_2O, reducing the promoting effect of water-gas-shift chemistry for $Fe(CO)_5$ decomposition.

This effect of heating rates on the particle diameter is the likely cause of the observed scatter in the plot (Figure 3-7). In repeated experiments at the same water concentrations and similar heating rates, ANOVA revealed the samples were statistically different (Appendix B, visualized as error bars in Figure 3-7). Small variations in heating rate resulted in subtle changes in the H_2O concentration causing scatter in the plot.

The reaction products had the distinctive almond-like odour of benzaldehyde.[21] Vacuum distillation of a reaction mixture followed by Gas-Chromatography-Mass Spectroscopy of the distillate showed evidence of benzaldehyde and toluene. This indicates thermal decomposition of the solvents at these temperatures for such extended periods of time. Furthermore, under these solvent conditions, a maximum water concentration of ~1600 ppm was achieved. The use of more hydrophilic solvents such as glymes may provide a further lower limit to particle size observed by this technique.

These experiments illuminate the influence of water concentration on particles size in the decomposition of $Fe(CO)_5$ to give near monodisperse nanoparticles of iron oxide. Average particle sizes were observed to range from of 5.6 nm down to 2.2 nm by simply changing the water concentration.

3.3.4 Avoiding the slow temperature gradient by hot introduction of $Fe(CO)_5$

To increase nucleation, a rapid decomposition of $Fe(CO)_5$ is preferable to achieve a sudden and high concentration of the active species for nucleation. Previously, $Fe(CO)_5$ has been added to room temperature or ~100 °C solutions before heating to the decomposition temperatures (see Section *3.3.1*). This slow heating itself may cause fewer nucleation events. Therefore, to achieve rapid decomposition the introduction of $Fe(CO)_5$ directly into solutions above the decomposition temperature was attempted.

A solution of $Fe(CO)_5$ was prepared and introduced directly into a ~290 °C mixture of octylether and oleylamine. This synthesis gave core-shell particles[23] (8.4 ± 3.1 nm ($n = 35$)) that sintered into large agglomerates of several hundred nanometers (Figure 3-10a and b). Yet at higher concentrations of oleylamine, and a lower temperature of only 200 °C, much smaller particles were achieved (3.86 ± 0.57 nm ($n = 123$)) (Figure 3-10c). Since surfactant concentration appears to be very important to achieve smaller particles, we can infer that under these conditions, growth remains a dominant factor over increasing nucleation events. The higher temperature may also be the cause for the large, core-shell particles and is most likely the cause of the sintering. At such high temperatures, the surfactant may be more labile from the particle surfaces allowing for enhanced growth and the sintering of particles together.

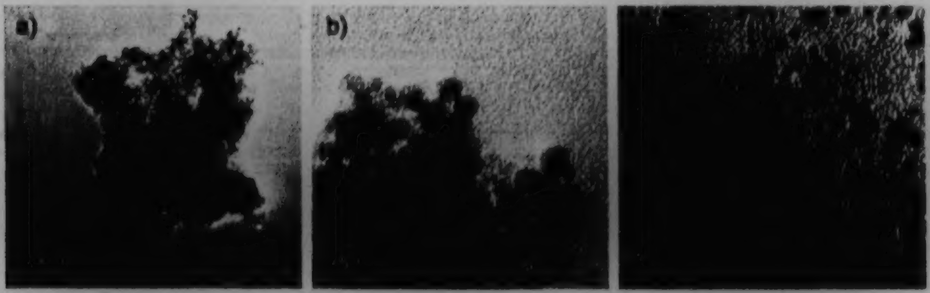

Figure 3-10. Particles achieved by introduction of liquid phase $Fe(CO)_5$ into octylether and a) and b) 1.5 eq oleylamine at ~290 °C c) 4 eq. oleylamine at 200 °C (Tecnai TEM).

Immediate decomposition of $Fe(CO)_5$ yields 5 eq. of CO gas (0.3 mL of $Fe(CO)_5$, 541 mL of CO gas evolved) at 300 °C – a temperature well above the flash point of many of the solvents and surfactants employed. This became a safety concern when using standard laboratory glassware. Instead, a gas phase introduction method was schemed to allow for $Fe(CO)_5$ to be introduced slowly, yet be exposed to the rapid temperature change required for rapid decomposition.

Using argon as a carrier gas, gaseous $Fe(CO)_5$ was bubbled into octylether at reflux (286 °C). Even with only the use of a very weakly coordinating solvent, octylether, small particles of 2.25 ± 0.17 nm (n = 149) diameter were produced (Figure 3-11a) indicating the decomposition was indeed rapid and provided many nucleation events. However, without a surfactant present, the particles sintered and did not readily disperse into individual particles after isolation. A surfactant was necessary to allow for later dispersion.

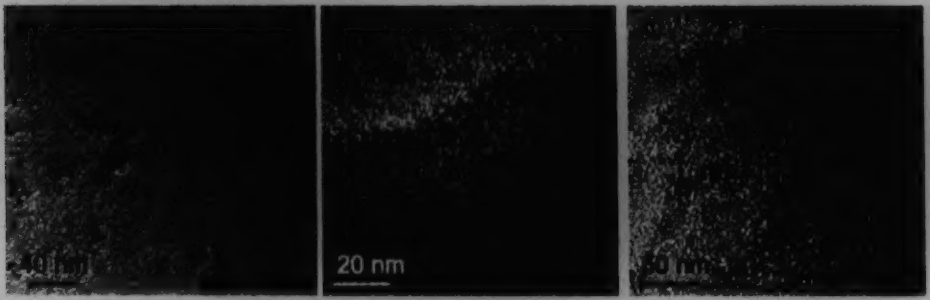

Figure 3-11 Iron oxide particle achieved from the bubbling of gaseous $Fe(CO)_5$ into hot solvents and surfactants a) octylether at 286 °C (JEOL TEM) b) TOPO at 280 °C c) TOPO at 280 °C, cooled, reheated and introduction restarted (Tecnai TEM)

When $Fe(CO)_5$ was bubbled into TOPO at 280 °C, the particles more readily dispersed after isolation. TEM revealed small particles of similar size to those achieved without surfactant (2.67 ± 0.27 nm (n = 92)) (Figure 3-11b). This preparation should be contrasted with the large and polydisperse particles seen from $Fe(CO)_5$ injected into a warm solution and slow heating to achieve decomposition (see Section *3.3.1,* Figure 3-4). From this, it is inferred hot introduction does indeed increase nucleation events to allow for smaller particles compared to introduction of the $Fe(CO)_5$ into a room temperature solution and then heating.

However, the growth processes are not arrested under these conditions. When the addition of $Fe(CO)_5$ was arrested, the solution cooled, then reheated, and introduction of $Fe(CO)_5$ resumed, both small and larger core-shell particles were observed (Figure 3-11c). This indicates that growth and/or Ostwald ripening processes are not completely inhibited by the TOPO under these conditions and the small particles sizes observed for the previous sample were from an increase in nucleation events and not from the surfactant inhibiting particle growth.

This gas-introduction technique was not optimized as the reaction and flow rates were extremely difficult to control. The decomposition of $Fe(CO)_5$ to release $CO_{(g)}$ increased the pressure in the reaction flask causing the gas introduction canula to arrest or even flow backwards. Also, without optimization, the yield of this method is unsatisfactory as it only gave several milligrams of product– barely enough to prepare a TEM grid.

The introduction of $Fe(CO)_5$ directly into hot solvent and surfactant mixtures as a gas or as a solution was observed to yield particles as small as ~3.5 nm. The size of particles achieved using oleylamine and TOPO were markedly smaller than those achieved through a slow heating of $Fe(CO)_5$/solvent/surfactant solutions (Section *3.3.1*). This strongly suggests that introduction of $Fe(CO)_5$ into hot surfactant and solvent mixtures increases the number of nucleation events to afford smaller particles. However, it was also shown that growth processes were not completely arrested by the presented experimental conditions and larger core-shell particles were observed under certain situations. This included very high temperatures where the surfactant is more labile from particle surfaces and the provision of seeds for growth by two separate decompositions steps.

3.3.5 Sonochemical decomposition

Sonochemical decomposition was performed to provide a rapid decomposition of $Fe(CO)_5$. Sonication of solutions is known to cause the formation, followed by implosive collapse, of micro-bubbles. This behavior provides localized temperatures of 5000 K followed by very rapid cooling ($\geq 10^{10}$ K/s).[51] This technique appears ideal for the preparation of small, monodisperse iron nanoparticles; the localized extreme temperatures will provide very rapid decomposition.

Sonochemical decomposition of $Fe(CO)_5$ has previously been reported for iron materials.[51-56] However, only a few reports describe dispersed particles[51, 54] and the technique appears to be under-explored. We undertook sonochemical studies on the decomposition of $Fe(CO)_5$ using different surfactants, and sonochemical reaction parameters in order to flesh out this technique for nanoparitlce formation.

Our initial studies indicated that the sonochemical synthesis produced particles larger than those that were observed for thermal decompositions (see Section *3.3.1*). For example, the sonochemical decomposition of $Fe(CO)_5$ in a solution of benzyl ether and oleic acid produced particles that were 6.0 ± 2.0 nm (n = 109) (Figure 3-12a). Many were large enough to be core-shell. Changing the reaction conditions to be under neat oleic acid produced even larger particles of diameters 9.8 ± 2.7 nm (n = 198) (Figure 3-12b). This indicates, again like the thermal decompositions, oleic acid is coordinating the iron in a molecular species and preventing nucleation. The larger sizes of the particles indicate the problem is more pronounced under sonochemical than thermal conditions.

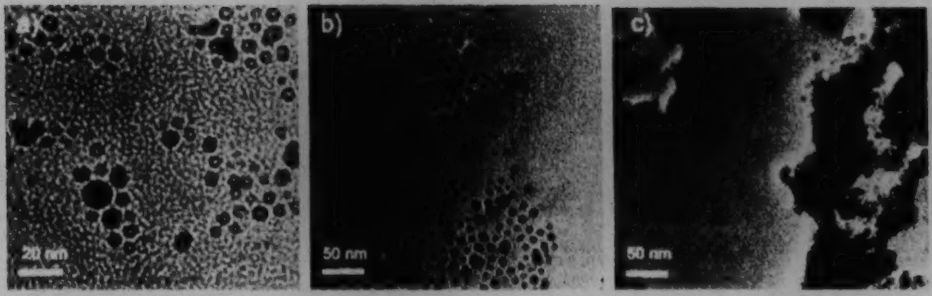

Figure 3-12 Sonochemical decomposition of $Fe(CO)_5$ in a) benzyl ether and oleic acid 6.0 ± 2.0 nm (n = 109) b) neat oleic acid 9.8 ± 2.7 nm (n = 198) c) benzyl ether and oleylamine (All images from Tecnai TEM).

When oleylamine was used as a surfactant, the same approximate sizes of particles as the oleic acid samples were produced however, they were sintered together – even with only a 20 s sonication time (Figure 3-12c). The weaker surfactant becomes labile under these conditions and cannot protect the particles from sintering.

Since oleylamine was also known to inhibit nucleation by ligating the iron, we continued experiments with TOPO. Although TOPO is considered an even weaker binding ligand than oleylamine, with it comes enhanced steric bulk as it has three carbon chains rather than only the one on oleic acid and oleylamine (Scheme 3-1). The added steric bulk of the TOPO was predicted to prevent sintering.

A series of small scale experiments using TOPO as a surfactant were performed examining pulse times, resting times, and reaction time. It was found that pulses of 1 s followed by a 3 s rest gave the most consistent and desirable results. When the total sonication time was 20 s, dispersed particles were observed (3.2 ± 1.0 nm, n = 172) (Figure 3-13a). To our knowledge, these are the smallest iron/iron oxide nanoparticles achieved by sonochemical synthesis reported in the literature.[54] However, after such a short reaction time, only a small amount of the $Fe(CO)_5$ was observed to be decomposed as evidenced by the yellow colour of the solution. Correspondingly, very little product was obtained. Increasing the reaction time in an attempt to increase the yield produced particles which where made up of similar sized particles as before but sintered together (Figure 3-13b and c).

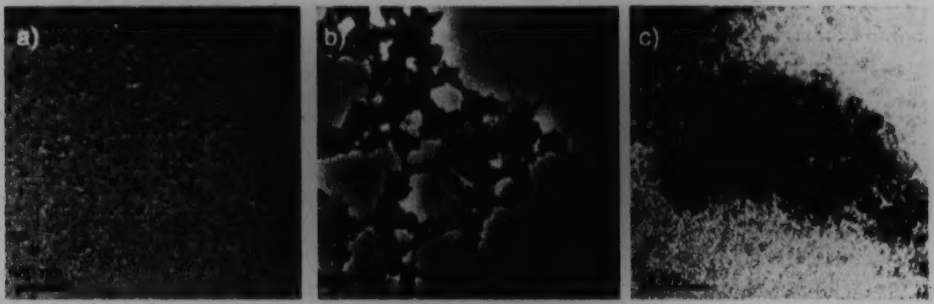

Figure 3-13 Sonochemical decomposition of $Fe(CO)_5$ in TOPO for a) 20 s, d = 3.2 ± 1.0 nm (n = 172) (JEOL TEM) b and c) 2.5 min (Tecnai TEM).

Sonication can be used for the synthesis of dispersed iron oxide nanoparticles below 4 nm. However, to avoid sintering of the particles, very short reaction times are necessary; as a result, the quantity of product obtained was small. Should this technique be further developed for bulk synthesis, it is likely a flow through reactor would produce the highest quality of dispersed nanoparticle product with a reasonable yield. Surfactant choice is very important as surfactants known to ligate iron in the decomposition of $Fe(CO)_5$, such as oleic acid and oleylamine, inhibited nucleation and gave larger particles than desired. Oleic acid did provide dispersed particles even under extended reaction times.

3.3.6 Calculation of the number of atoms per particle

To aid the understanding of the scale of the synthesized particles within this chapter, the approximate sizes of the iron particles, before oxidation, and the number of atoms in each particle is calculated here.

Using the literature density for α-Fe (7.87 g/cm^3),[57] the calculated density for maghemite based on the unit cell (5.49 g/cm^3),[58] and their formula masses, an volume expansion for the oxidation of an iron particle can be calculated.

$$\frac{vol\,Fe_2O_3}{vol\,Fe}=\frac{\dfrac{159.19\,g/mol\,Fe_2O_3}{5.49\,g/cm^3\,Fe_2O_3}}{\dfrac{55.85\,g/mol\,Fe}{7.87\,g/cm^3\,Fe}}\times\frac{1\,mol\,Fe_2O_3}{2\,mol\,Fe}=2.04 \qquad (8)$$

The corresponding expansion of the particle diameter, d, is:

$$\frac{d\,Fe_2O_3}{d\,Fe}=\left(\frac{vol\,Fe_2O_3}{vol\,Fe}\right)^{1/3}=1.27 \qquad (9)$$

Therefore, observed 5.6 nm and 2.2 nm diameter maghemite particles would have originated as a 4.4 nm and 1.7 nm iron particles, respectively.

For the α-Fe, BCC crystal structure, the number of atoms in a particle can be approximated by[59]:

$$\#\,of\,atoms=\frac{vol\,particle}{vol\,of\,unit\,cell}\times atoms\,per\,unit\,cell=\frac{\pi}{3}\left(\frac{d}{a_{Fe}}\right)^3 \qquad (10)$$

where a_{Fe} is the lattice parameter of α-Fe (0.287 nm). Therefore, a 4.4 nm diameter iron particle has ~3800 atoms where as a 1.7 nm diameter particle has only ~200 atoms. At these sizes these approximations likely hold, yet extension of these calculations into smaller sizes is cautioned. Magic number clusters of iron are predicted to occur at ~100 and have been observed for fewer atoms of iron.[60, 61] These clusters are predicted to be the result an thermodynamic energy minimum from of the completion of icosohedral geometries of the arranged iron atoms in the clusters. These geometries therefore deviate from the bulk crystal structure and the spherical shape assumed above. In these cases, other methods of determining the number of atoms in the particles will be required.

3.4 Conclusions

Several techniques were studied to afford monodisperse iron/iron oxide nanoparticles below 4 nm from the decomposition of $Fe(CO)_5$. Inhibition of growth and increasing (or inhibiting) nucleation events were the two general themes for technique development, however it was found that only rarely can the exploration of one be done without a discussion of the other.

Surfactants can inhibit growth but can also prevent nucleation by ligating the iron as molecular species. This limits the strict application of different surfactants for achieving smaller particles than those already seen in the literature.

Water as an impurity was shown to act as a promoter for the thermal decomposition of $Fe(CO)_5$ through water-gas-shift chemistry. This more ready decomposition increases nucleation events and was observed to decrease average particle size from 5.6 nm down to 2.2 nm for oleic acid capped particles.

Introduction of $Fe(CO)_5$ into hot solvent and surfactant mixtures was shown to be an effective route for increasing nucleation events and decreasing particles size down to 2.3 nm. However, safety and low yields were of concern.

Sonication of $Fe(CO)_5$ containing solutions can also be used to yield dispersed particles as small as 3.2 nm. A bulky surfactant that would not strongly ligate the iron was required to achieve such sizes and impede sintering. However, yields were low because of the short reaction times required to prevent sintering.

The goal of 1.6 nm diamter particles was nearly reached; calculations indicate that the 2.2 nm maghemite particles synthesized and observed are a result of the oxidation of 1.7 nm iron particles. Significant achievements were made into understanding the factors influencing particles size. Furthermore, several different techniques were developed for achieving particles smaller than 4 nm.

3.5 References

1 T. Hyeon, *Chemical Communications*, 2003, 927-934.

2 D. L. Huber, *Small*, 2005, **1**, 482-501.

3 P. Tartaj, M. P. Morales, T. Gonzalez-Carreno, S. Veintemillas-Verdaguer and C. J. Serna, *Journal of Magnetism and Magnetic Materials*, 2005, **290**, 28-34.

4 O. Bomati-Miguel, M. P. Morales, P. Tartaj, J. Ruiz-Cabello, P. Bonville, M. Santos, X. Q. Zhao and S. Veintemillas-Verdaguer, *Biomaterials*, 2005, **26**, 5695-5703.

5 K. Somaskandan, T. Veres, M. Niewczas and B. Simard, *New Journal of Chemistry*, 2008, **32**, 201-209.

6 A. H. Lu, E. L. Salabas and F. Schuth, *Angewandte Chemie-International Edition*, 2007, **46**, 1222-1244.

7 D. Takagi, Y. Homma, H. Hibino, S. Suzuki and Y. Kobayashi, *Nano Letters*, 2006, **6**, 2642-2645.

8 M. L. Terranova, V. Sessa and M. Rossi, *Chemical Vapor Deposition*, 2006, **12**, 315-325.

9 E. Lamouroux, P. Serp and P. Kalck, *Catalysis Reviews-Science and Engineering*, 2007, **49**, 341-405.

10 M. H. Rummeli, C. Kramberger, F. Schaffel, E. Borowiak-Palen, T. Gemming, B. Rellinghaus, O. Jost, M. Loffler, P. Ayala, T. Pichler and R. J. Kalenczuk, *Physica Status Solidi B-Basic Solid State Physics*, 2007, **244**, 3911-3915.

11 Christopher Brooks, Honda Research Institute Inc., personal communication 2006.

12 M. J. Bonder, Y. Zhang, K. L. Kiick, V. Papaefthymiou and G. C. Hadjipanayis, *Journal of Magnetism and Magnetic Materials*, 2007, **311**, 658-664.

13 S. Santra, R. Tapec, N. Theodoropoulou, J. Dobson, A. Hebard and W. H. Tan, *Langmuir*, 2001, **17**, 2900-2906.

14 F. Dumestre, B. Chaudret, C. Amiens, P. Renaud and P. Fejes, *Science*, 2004, **303**, 821-823.

15 D. Farrell, S. A. Majetich and J. P. Wilcoxon, *Journal of Physical Chemistry B*, 2003, **107**, 11022-11030.

16 S. J. Park, S. Kim, S. Lee, Z. G. Khim, K. Char and T. Hyeon, *Journal of the American Chemical Society*, 2000, **122**, 8581-8582.

17 R. Psaro, A. Fusi, R. Ugo, J. M. Basset, A. K. Smith and F. Hugues, *Journal of Molecular Catalysis*, 1980, **7**, 511-522.

18 M. V. Kovalenko, M. I. Bodnarchuk, R. T. Lechner, G. Hesser, F. Schaffler and W. Heiss, *Journal of the American Chemical Society*, 2007, **129**, 6352-6353.

19 X. W. Teng and H. Yang, *Journal of Materials Chemistry*, 2004, **14**, 774-779.

20 T. W. Smith and D. Wychick, *Journal of Physical Chemistry*, 1980, **84**, 1621-1629.

21 *The Merck Index*, 13th edn., Merck and Co., Whitehouse Station, NJ, 2001, p. 181.

22 M. F. Casula, Y. W. Jun, D. J. Zaziski, E. M. Chan, A. Corrias and A. P. Alivisatos, *Journal of the American Chemical Society*, 2006, **128**, 1675-1682.

23 A. Cabot, V. F. Puntes, E. Shevchenko, Y. Yin, L. Balcells, M. A. Marcus, S. M. Hughes and A. P. Alivisatos, *Journal of the American Chemical Society,* 2007, **129**, 10358-10360.

24 U. Jeong, X. W. Teng, Y. Wang, H. Yang and Y. N. Xia, *Advanced Materials,* 2007, **19**, 33-60.

25 J. Park, E. Lee, N. M. Hwang, M. S. Kang, S. C. Kim, Y. Hwang, J. G. Park, H. J. Noh, J. Y. Kini, J. H. Park and T. Hyeon, *Angewandte Chemie International Edition,* 2005, **44**, 2872-2877.

26 V. K. Lamer and R. H. Dinegar, *Journal of the American Chemical Society,* 1950, **72**, 4847-4854.

27 T. Sugimoto, *Journal of Colloid and Interface Science* 2007, **309**, 106-118.

28 A. G. Roca, M. P. Morales and C. J. Serna, *IEEE Transactions on Magnetics,* 2006, **42**, 3025-3029.

29 E. Jungermann, J. F. Gerecht and I. J. Krems, *Journal of the American Chemical Society,* 1956, **78**, 172-174.

30 D. J. Fox, J. Reckless, S. M. Wilbert, I. Greig, S. Warren and D. J. Grainger, *Journal of Medicinal Chemistry,* 2005, **48**, 867-874.

31 T. Hyeon, S. S. Lee, J. Park, Y. Chung and H. Bin Na, *Journal of the American Chemical Society,* 2001, **123**, 12798-12801.

32 S. Peng, C. Wang, J. Xie and S. H. Sun, *Journal of the American Chemical Society,* 2006, **128**, 10676-10677.

33 J. W. Cheon, N. J. Kang, S. M. Lee, J. H. Lee, J. H. Yoon and S. J. Oh, *Journal of the American Chemical Society,* 2004, **126**, 1950-1951.

34 H. P. Shao, H. Lee, Y. Q. Huang, I. Y. Ko and C. Kim, *IEEE Transactions on Magnetics,* 2005, **41**, 3388-3390.

35 N. Cordente, M. Respaud, F. Senocq, M. J. Casanove, C. Amiens and B. Chaudret, *Nano Letters,* 2001, **1**, 565-568.

36 P. W. Voorhees, *Annual Review of Materials Science,* 1992, **22**, 197-215.

37 S. Yu and G. M. Chow, *Journal of Nanoscience and Nanotechnology,* 2006, **6**, 2135-2140.

38 D. T. Robb and V. Privman, *Langmuir,* 2008, **24**, 26-35.

39 U. Schubert and N. Hüsing, *Synthesis of Inorganic Materials*, Wiley-VCH, Weinheim, 2000, pp. 135-154.

40 S. Veintemillas-Verdaguer, O. Bomati-Miguel and M. P. Morales, *Scripta Materialia,* 2002, **47**, 589-593.

41 S. Veintemillas-Verdaguer, O. Bomati, M. P. Morales, P. E. Di Nunzio and S. Martelli, *Materials Letters,* 2003, **57**, 1184-1189.

42 S. Martelli, A. Mancini, R. Giorgi, R. Alexandrescu, S. Cojocaru, A. Crunteanu, I. Voicu, M. Balu and I. Morjan, *Applied Surface Science,* 2000, **154**, 353-359.

43 R. Alexandrescu, I. Morjan, A. Crunteanu, S. Cojocaru, S. Petcu, V. Teodorescu, F. Huisken, B. Kohn and M. Ehbrecht, *Materials Chemistry and Physics,* 1998, **55**, 115-121.

44 J. E. Macdonald, C. J. Brooks and J. G. C. Veinot, *Chemical Communications,* 2008, 3777 - 3779.

45 A. D. King, R. B. King and D. B. Yang, *Journal of the American Chemical Society,* 1980, **102**, 1028-1032.

46 L. S. Sunderlin and R. R. Squires, *Journal of the American Chemical Society,* 1993, **115**, 337-343.

47 W. Hieber and H. Vetter, *Zeitschrift fur Anorganische und Allgemeine Chemie,* 1933, **212**, 145-168.

48 K. E. Lewis, D. M. Golden and G. P. Smith, *Journal of the American Chemical Society,* 1984, **106**, 3905-3912.

49 R. B. Jordan, *Reaction Mechanisms of Inorganic and Organometallic Systems*, 2nd edn., Oxford University Press, New York, 1998, p. 15.

50 D. G. Altman, *Practical Statistics for Medical Research*, Chapman and Hall, New York, 1991, pp. 278-279, 308-309.

51 K. Shafi, A. Ulman, X. Z. Yan, N. L. Yang, C. Estournes, H. White and M. Rafailovich, *Langmuir,* 2001, **17**, 5093-5097.

52 X. Cao, Y. Koltypin, G. Kataby, R. Prozorov and A. Gedanken, *Journal of Materials Research,* 1995, **10**, 2952-2957.

53 R. Abu Mukh-Qasem and A. Gedanken, *Journal of Colloid and Interface Science,* 2005, **284**, 489-494.

54 K. S. Suslick, M. M. Fang and T. Hyeon, *Journal of the American Chemical Society,* 1996, **118**, 11960-11961.

55 H. Khalil, D. Mahajan, M. Rafailovich, M. Gelfer and K. Pandya, *Langmuir,* 2004, **20**, 6896-6903.

56 T. Prozorov, G. Kataby, R. Prozorov and A. Gedanken, *Thin Solid Films,* 1999, **340**, 189-193.

57 *CRC Handbook of Chemistry and Physics*, 70th edn., CRC Press, Inc., Boca Raton, 1989-1990, pp. B-96.

58 Maghemite Mineral Data 2008. http://webmineral.com/data/Maghemite.shtml (accessed August 21, 2008).

59 J. D. Holmes, K. J. Ziegler, R. C. Doty, L. E. Pell, K. P. Johnston and B. A. Korgel, *Journal of the American Chemical Society,* 2001, **123**, 3743-3748.

60 G. Rollmann, M. E. Gruner, A. Hucht, R. Meyer, P. Entel, M. L. Tiago and J. R. Chelikowsky, *Physical Review Letters,* 2007, **99**.

61 M. Sakurai, K. Watanabe, K. Sumiyama and K. Suzuki, *Journal of Chemical Physics,* 1999, **111**, 235-238.

Chapter 4: Iron/Iron oxide nanoparticle sequestration of catalytic metal impurities from aqueous media and organic reaction products *

4.1 Introduction

Late transition metal homogeneous catalysts are well established as powerful tools in organic synthesis. They allow for otherwise difficult syntheses with rapidity, selectivity, and high yields.[1] Unfortunately, even trace catalyst impurities remaining after product purification can interfere with later synthetic steps and eventual material application.[2,3] Also, application of metal catalysts is often limited for pharmaceutical syntheses because metal concentrations in the final product exceed health standards (*e.g.*, 5 ppm for Pt, Pd, Ru, or Rh; 10 ppm for Ni; 15 ppm for Cu; 20 ppm for Fe).[2-4]

To date, techniques for removing transition metal catalysts from organic reaction products are often time consuming, taking up to 65 h,[3] and employ high surface area adsorbents such as carbon black and absorbing polymers. Modern commercial resins, fibers, and powders are commonly modified with metal scavenging thiol, carboxylic acid, or amine functionalities.[2, 3, 5] Each sequestration method has associated benefits and limitations. For example, some are metal specific,[3, 5] others absorb less discriminately, sometimes reducing yields;[2, 5] some achieve only minimum extraction requirements prescribed by regulatory bodies, while others are expensive or impractical in many laboratory or industrial situations.[3] We present a rapid, versatile, inexpensive, and straightforward alternative for removing catalytic metal ions from solutions of organic reaction products in water-miscible solvents (*e.g.*, THF). Importantly, the present approach employs common reagents and is practical for both laboratory and industrial application.

---

* Reproduced with permission from J. E. Macdonald, J. A. Kelly and J. G. C. Veinot, *Langmuir*, 2007, **23**, 9543-9545. Copyright 2007 American Chemical Society.

Herein, oxide-capped metallic iron nanoparticles ($Fe@Fe_xO_y$) are used to sequester catalytic metal ions from organic reaction products. Similar approaches have been applied to the environmental remediation of some metal ions (e.g., Cr(VI), Pb(II), Ni(II), Ag(I), Cd(II)),[6-10,11] however a direct transposition of these methods to organic reaction products may be complicated by adverse side reactions, leaching of Fe, *etc. (vide infra)*. Furthermore, while comparable iron nanomaterials have effectively lowered some metal contaminant concentrations in the environment, it remains unclear if stringent pharmaceutical regulatory requirements for standard catalytic metal concentrations in organic materials can be met.[4]

4.2 Experimental Procedures

4.2.1 Reagents

Iron(III) chloride hydrate, copper sulfate and styrene were purchased from Fisher, cobalt(II) nitrate from Mallinckrodt, silver nitrate from Englehard, sodium borohydride from EMD Chemicals, sodium nitrate from ACP chemicals, rhodium(III) chloride hydrate from Colonial Metals and potassium nitrate from BDH Chemicals. The remaining reagents were purchased from Sigma-Aldrich. All reagents were used as received without further purification. Phenyl azide was synthesized using a literature procedure.[12] Typically, in-house deionized water was employed for the synthesis of iron nanoparticles. Sequestration studies were performed using 18.2 MΩ·cm water.

4.2.2 *Synthesis and sequestration*

Synthesis of $Fe@Fe_xO_y$

$Fe@Fe_xO_y$ was prepared using a modified literature procedure.[9, 13] Briefly, $FeCl_3 \cdot 6H_2O$ (5.70 g, 21 mmol) was dissolved in 400 mL of deionized water. A solution of $NaBH_4$ (2.24 g, 59 mmol) in 30 mL of water was added dropwise while the iron chloride solution was stirred vigorously. The orange solution became dark with a black precipitate. The precipitate was vacuum filtered and washed with 500 mL of water followed by 50 mL of 95% ethanol. The resulting black paste was transferred to a round bottom flask and dried *in vacuo* for two days to yield a black powder that was stored in an argon-filled glovebox (< 0.1 ppm H_2O, 0.6 ppm O_2). Yield: 1.06 g.

Sequestration of aqueous metal ions

Metal salt solutions (*i.e.*, nitrates, chlorides, or acetates) were prepared at metal concentrations of ~ 100 ppm in 3 x 10^{-6} M KOH solution. Silver nitrate, ruthenium chloride and rhodium chloride solutions were prepared in 18.2 MΩcm water. $Fe@Fe_xO_y$

were placed in round bottom flasks in an argon-filled glovebox and transferred to a Schlenk line. An appropriate metal ion solution was transferred to the flask to achieve a ratio of 50 mg of $Fe@Fe_xO_y$ for every 10.00 mL of solution. The particle/solution mixture was subsequently capped and stirred for 30 min. The mixtures were allowed to settle for 2 minutes to allow the majority of the $Fe@Fe_xO_y$ to collect on the magnetic stir bar. This aided the subsequent gravity filtration in which remaining solids were removed. The addition of KNO_3 (0.10 g) and a second filtration was required to remove highly charged, dispersed particles. The resulting colorless filtrates were acidified with two drops of concentrated nitric acid to facilitate analysis of metal concentrations by Quadropole-Inductively Coupled Plasma-Mass Spectroscopy (Quad-ICP-MS).

"Click" Cu(I) catalyzed cycloaddition to form 1,4-disubstituted 1,2,3 triazole (3) [14]

Phenylazide (**1**) (0.59 g, 5 mmol) and 3-phenyl-1-propyne (**2**) (0.4 mL, 3 mmol) were suspended in 20 ml of a 1:1 mixture of water:butanol. To this suspension, 0.5 mL of a freshly prepared 1.0 M sodium ascorbate solution was added followed by copper sulphate hydrate (12.5 mg, 0.05 mmol). The reaction mixture was stirred for 16 h, until an off-white solid formed. The solid was filtered and washed twice with cold deionized water, yielding 715 mg (94%) of 1,4-disubstituted 1,2,3 triazole (**3**). ^1H NMR (400 MHz, $CDCl_3$): δ 7.62 (2H, m), 7.53 (1H, s), 7.43 (2H, m), 7.34 (1H, tt), 7.27 (4H, m), 7.20 (1H, m), 4.06 (2H, s). The product was also confirmed by Gas Chromatography-Mass Spectroscopy (GC-MS) (m/z: 235, 206, 180, 130, 104, 77, 51)

Sequestration of Cu impurities from "Click" cycloaddition product

129.2 mg of the products from the aforementioned "Click" reaction were dissolved in 20 mL of THF and 0.5 mL of KOH solution (pH 10.3). This was added to 100 mg of Fe@Fe_xO_y and stirred for 3 h in oxygen free conditions. The mixture was allowed to stand for 2 minutes allowing for most of the nanoparticle powder to collect on the magnetic stir bar. Remaining solids were removed by gravity filtration and the iron nanoparticles were washed three times with THF. Approximately 2/3 of the filtrate was added to 50 mg of Fe@Fe_xO_y and 0.5 mL of KOH solution (pH 10.3) and stirred for 3 h. The mixture was allowed to stand for 2 minutes allowing for most of the nanoparticle powder to collect on the magnetic stir bar. Remaining solids were removed by gravity filtration and the iron nanoparticles were washed three times with THF. Solvent from the two filtrates was removed *in vacuo* yielding slightly yellow crystals (100% of cycloadduct recovered). No additional products were observed by GC-MS.

Determination of metal concentrations in "Click" cycloaddition product

The organic product (*ca.* 50-85 mg) of was placed in a porcelain crucible and heated to 625 °C overnight in air. The remaining dark solids were dissolved in concentrated nitric acid, diluted with 18.2 MΩcm water in a 10.00 mL volumetric flask and metal concentrations were determined using Quad-ICP-MS.

Another approach involved dissolving the organic product (ca. 55-185 mg) in 8 M HNO_3 (25.00 mL), followed by analysis by Quad-ICP-MS for Cu content.

Synthesis of *N,N*-dimethyl-β-alanine hydrochloride [15]

β-alanine (3.59 g, 40.3 mmol), formalin (5 mL) and 90% formic acid (25 mL) were brought to reflux for 8 h. Concentrated HCl (5 mL) was added and the solvent was removed *in vacuo* giving a slightly yellow solid. Formic acid (~15 mL) was added and the slurry was vacuum filtered and washed with formic acid. White solid 3.1 g, 55% yield. ^{1}H NMR (500 MHz, $CDCl_3$): δ 2.87-2.901 (8H, m), 3.41-3.437 (2H, t).

Pd catalyzed Heck coupling to form *trans*-stilbene (**6**) [15]

Bromobenzene (**5**) (1.05 mL, 10 mmol), styrene (**4**) (1.75 mL, 15 mmol), palladium acetate (16.3 mg, 72.6 μmol), *N,N*-dimethyl-β-alanine hydrochloride (10 mg, 71.6 μmol), potassium carbonate (2.72 g, 20 mmol) and anhydrous dimethyformamide (10 mL) were stirred and heated to 130 °C for 16 h leaving a dark solution. The product was extracted in diethyl ether and washed with water three times. The ether layer was gravity filtered to remove any black precipitate and the solvent was removed *in vacuo*. Slightly yellow crystals, 1.77 g of *trans*-stilbene (**6**). Yield 98% ^{1}H NMR (400 MHz, $CDCl_3$): δ 7.50 (4H, d), 7.34 (4H, t), 7.24 (2H, t), 7.10 (2H s). The product was further confirmed by GC-MS. m/z: 180, 165, 152. (Trace minor products noted 1,1-diphenyl ethene (m/z: 180, 165, 152) and 1,1,2- triphenylethene (m/z: 256, 239, 176).)

Sequestration of Pd impurities from Heck coupling product

Trans-stilbene (**6**) as a product from above (308.7 mg) was dissolved in 15 mL of THF and added to 50 mg of $Fe@Fe_xO_y$ under argon atmosphere. An additional 0.5 mL of KOH solution (pH 10.3) was added. The mixture was stirred for 20 min and then allowed to stand for 2 min to allow the majority of the nanoparticles to collect on the magnetic stir bar. The solution was gravity filtered and the nanoparticles washed three times with THF. The filtrate solvent was removed *in vacuo* yielding off white crystals (302.7 mg, 98%). No additional products were observed by GC-MS.

Determination of metal concentrations in Heck coupling product

Organic products (*ca.* 115-125 mg) were placed in a sublimation flask and heated to 200 °C under dynamic vacuum. The residual dark solids remaining in the flask were dissolved in warm concentrated nitric acid and diluted with 18.2 MΩcm water in a 10.00 ml volumetric flask. Metal concentrations were found with Quad-ICP-MS.

4.2.3 Material characterization

Quadropole Inductively Coupled Plasma- Mass Spectroscopy (Quad ICP-MS) was performed on a Perkin Elmer Elan 6000 ICP-MS. Samples were acidified with nitric acid to pH <2. The flow rate on the instrument was 1 mL/min and dual detector mode was employed. A blank was subtracted after internal standard correction and the values reported are an average of three readings (35 sweeps per reading).

Gas Chromatography- Mass Spectroscopy (GC-MS) was performed on a Waters 7070E GC-MS using electron ionization. 1 μL of a dichloromethane solution of the product was injected into a Phenomenex ZB-5, 30 m x 0.25 mm column with a 0.35 μm film. The carrier gas was helium at 1 mL/min. The injection port was at 275 °C and a linear temperature profile (50-300 °C at 10 °C / minute) was employed.

X-Ray Photoelectron Spectroscopy (XPS) was performed on and AXIS-165 XPS spectrometer from Kratos Analytical. The source was monochromatic Al Kα X-rays at a power of 210 W. The analyzer was perpendicular to the surface. Base pressure in the analytical chamber was 10^{-6} - 10^{-7} Pa. The area of the sample analyzed was 400 x 700 μm, with the analyzer normal to the surface. The pass energy for the survey spectra and the high-resolution spectra were 160 eV and 20 eV, respectively. The instrument resolution is 0.4 eV. Samples were pressed onto carbon tape and spectra were calibrated to the C 1s peak at 284.8 eV.

Transmission Electron Microscopy samples were prepared by suspending particles in THF and drop-coating the solution on carbon coated, 200 mesh Cu grid (SPI Supplies). Samples were evaluated using a JEOL 2010 Transmission Electron Microscope (TEM) at 200 keV accelerating voltage and a LaB_6 filament. This instrument was also fitted with Energy Dispersive X-Ray (EDS) detector for elemental analysis.

4.3 Results and Discussion

The generally accepted mechanism by which low valent iron nanomaterials remove ionic metal species involves the surface adsorption of ions onto the oxide shell. Subsequently, ions are reduced to their elemental form by electrons supplied from the iron core. While this process increases the sequestration capacity far beyond what is afforded by surface adsorption alone,[8, 9] it relies heavily upon surface interaction with metal ions. In this regard, surface wettability and coordination of organic reagents could hinder application of Fe@Fe_xO_y in these environments. Furthermore, while the present method can conceivably remove any metal ion with a suitable reduction potential, it is necessary that we demonstrate that typical catalytic metal concentrations in aqueous media can be lowered from typical catalytic to sub-40 ppb levels as a benchmark for the present work. These low concentrations are prerequisites to any further extension of this approach to organic synthetic applications; ppb metal levels in solution translate to ppm concentrations in the organic product upon removal of solvent during work-up. We subsequently extend our methodology to two important synthetic reactions for which metal toxicity could limit utility: namely, a Cu(I)-catalyzed "Click" reaction[14] and a Pd-catalyzed Heck coupling.[15, 16]

4.3.1 Fe@Fe_xO_y and the sequestration of aqueous ions

Fe@Fe_xO_y were prepared by sodium borohydride reduction of iron(III) chloride in aqueous solution.[9, 13] Bright field transmission electron micrographs (TEM) show particles are pseudospherical, have dimensions of 20-80 nm, and tend to aggregate into chains (Figure 4-1) as a result of their magnetic properties.[17, 18] Selected area electron diffraction (SAED) shows well-defined rings previously indexed to Fe_3O_4 (Figure 4-1, inset).[13] No reflections characteristic of iron metal are observed, suggesting a non-crystalline metallic core. Particles can be stored refrigerated in ethanol[10] or dry in inert atmosphere.

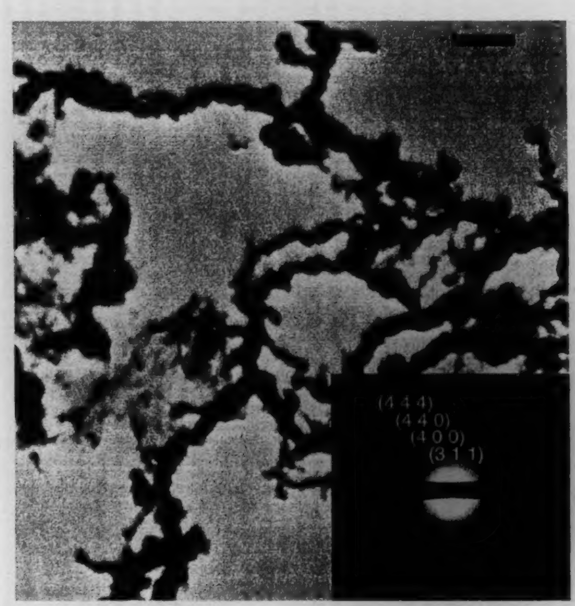

Figure 4-1 Brightfield TEM image of Fe@Fe_xO_y, bar = 200 nm. Inset: SAED showing characteristic reflections indexed to Fe_3O_4.[13]

Aqueous catalytic metal ion sequestration was achieved by adding basic (pH ≈ 8.5) solutions of metal salts to Fe@Fe_xO_y. At increased pH, surface -OH groups are deprotonated thereby facilitating coordination of metal ions.[9] Typically, 50 mg of Fe@Fe_xO_y were used for 10 mL of 100 ppm metal ion solution. After stirring for 30 min, gravity filtration afforded clear, colorless solutions with metal concentrations smaller than those typically realized using status quo sequestration materials[2, 3, 9] while also far surpassing pharmaceutical standards (Table 4-1).[4] We also confirmed iron leaching is negligible; no significant increase in iron concentration was noted following sequestration of any metal species; background iron concentration surpassed pharmaceutical requirements (Table 4-1).[4] X-ray Photoelectron Spectroscopy (XPS) of the recovered particles confirmed the presence of the sequestered metals in all cases except cobalt. At such low concentrations, the cobalt 2p emission was masked by the strong iron LMM Auger peak (788-790 eV), hence the presence of cobalt could not be confirmed. Concentrations of the sequestered metals were too low to allow for detailed analysis (Appendix C). TEM of the particles after sequestration showed no obvious changes.

Table 4-1 Sequestration of metal ions from basic aqueous solutions using $Fe@Fe_xO_y$.

M	Metal Source	Initial $[M^{x+}]$ (ppm) [d]	Final $[M^{x+}]$ (ppb) [d]	% removed	[Fe][a] (ppm) [d]
Co^{2+}	$Co(NO_3)_2 \cdot xH_2O$	117	16.7	99.986	0.100
Ni^{2+}	$Ni(NO_3)_2 \cdot 6H_2O$	131	37.1	99.97	0.143
Cu^{2+}	$Cu(NO_3)_2 \cdot 2.5H_2O$	129	28.7	99.98	0.0894
Ru^{x+} [b,c]	$RuCl_3 \cdot xH_2O$	101	4.7	99.995	
Rh^{x+} [b,c]	$RhCl_3 \cdot xH_2O$	228	0.6	99.9997%	
Pd^{2+} [c]	$Pd(OAc)_2$	138	5.8	99.996	0.869
Ag^{+} [c]	$AgNO_3$	123	0.2	99.9998%	0.110
Pt^{4+}	$PtCl_4$	67.3	2.4	99.996	
Fe	Blank Particles				4

[a] Cl^- interferes with the ICP-MS analysis for [Fe].[19] [b] $RuCl_3$ and $RhCl_3$ are known to produce multiple oxidation states in aqueous media.[1] [c] These metals are known to form stable oxides in basic conditions.[20] As a consequence, analysis was performed in neutral conditions. [d] Concentrations given have < 6% relative standard deviation upon 3 runs by ICP-MS.

4.3.2 Application to Organic Synthesis

To highlight the importance of this method, we applied it to a synthetically significant, well-established metal catalyzed reactions: Cu(I)-catalyzed "Click" cycloaddition (Scheme 4-1)[14] and a Pd-catalyzed Heck coupling (Scheme 4-2).[15] An N-O ligand was chosen for the Heck coupling to minimize the influence of strongly-binding phosphines (which will be a focus of Chapter 5).

Scheme 4-1 Application of Fe@Fe_xO_y sequestering to a "Click" copper catalyzed cycloaddition.[14] Copper concentrations are provided in ppm of the organic product.

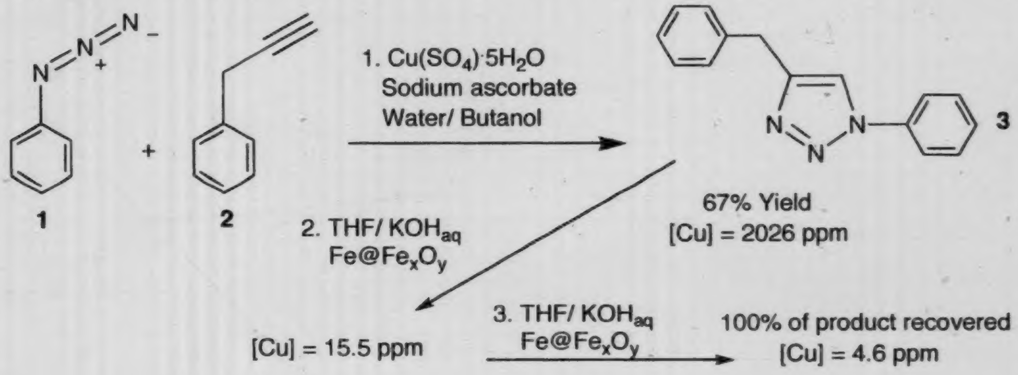
1
2
3
+
1. $Cu(SO_4)\cdot 5H_2O$
Sodium ascorbate
Water/ Butanol
67% Yield
[Cu] = 2026 ppm
2. THF/ KOH_{aq}
Fe@Fe_xO_y
[Cu] = 15.5 ppm
3. THF/ KOH_{aq}
Fe@Fe_xO_y
100% of product recovered
[Cu] = 4.6 ppm

Scheme 4-2 Application of Fe@Fe_xO_y sequestering to a Pd catalyzed Heck coupling.[15] Pd concentrations are provided in ppm of the organic product.

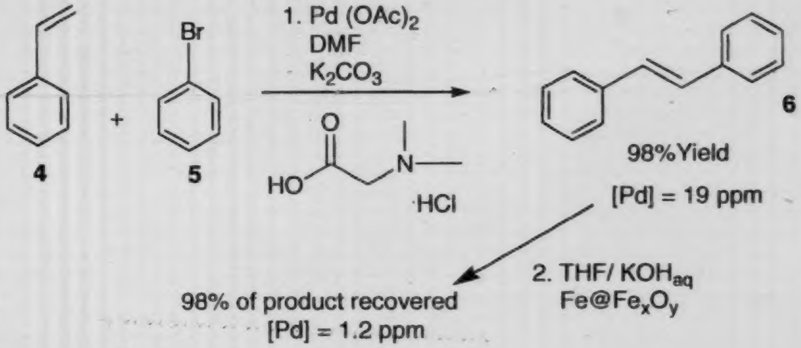
4
5
6
+
Br
1. Pd $(OAc)_2$
DMF
K_2CO_3
HO
O
N
·HCl
98%Yield
[Pd] = 19 ppm
2. THF/ KOH_{aq}
Fe@Fe_xO_y
98% of product recovered
[Pd] = 1.2 ppm

Metal ions were then sequestered from THF solutions of crude organic product mixtures prior to traditional purification. Cu content in the "Click" reaction product mixture was reduced from 2026 to 15.5 ppm upon a first sequestration step. Because this concentration exceeded the pharmaceutical standard, a second treatment with Fe@Fe_xO_y

was employed, further lowering the concentration to 4.6 ppm. For the Heck reaction, Pd concentration was reduced from 19 to 1.2 ppm. Importantly, no additional organic byproducts were observed by gas chromatography-mass spectroscopy for either reaction, confirming Fe@Fe_xO_y did not promote adverse side reactions. Additionally, Fe concentrations were not significantly above those reported in Table 4-1.

4.4 Conclusions

The present method for removing trace catalytic metal ions from organic reaction products is easily employed because it requires no complex procedures. Furthermore, Fe@Fe_xO_y are quantitatively removed by gravity filtration without column chromatography. The reagents for preparing Fe@Fe_xO_y are common in many synthetic laboratories making this technique readily available to the laboratory chemist. Advantages at the industrial scale are readily evident; all procedures are readily scalable and the magnetic properties of the particles make them amenable to magnetic filtration. We have shown the successful sequestration of a host of catalytic metal ions from aqueous solutions to levels far below pharmaceutical standards.[4] The technique has been extended to the sequestering of Cu and Pd from organic reaction media showing it to be comparable or better than many scavenging techniques available.[2, 3]

4.5 References

1 P. B. Kettler, *Organic Process Research and Development,* 2003, **7**, 342-354.

2 K. McEleney, D. P. Allen, A. E. Holliday and C. M. Crudden, *Organic Letters,* 2006, **8**, 2663-2666.

3 C. E. Garrett and K. Prasad, *Advanced Synthesis & Catalysis,* 2004, **346**, 889-900.

4 Committee for Proprietary Medicinal Products Note for guidance on specific limits for residues of metal catalysts, **2002**. The European Agency for the Evaluation of Medicinal Products. www.emea.europa.eu/pdfs/human/swp/444600en.pdf (accessed January 25, 2008).

5 A. Thayer, *Chemical and Engineering News,* 2005, **83**, 55-58.

6 S. M. Ponder, J. G. Darab, J. Bucher, D. Caulder, I. Craig, L. Davis, N. Edelstein, W. Lukens, H. Nitsche, L. F. Rao, D. K. Shuh and T. E. Mallouk, *Chemistry of Materials,* 2001, **13**, 479-486.

7 S. M. Ponder, J. G. Darab and T. E. Mallouk, *Environmental Science & Technology,* 2000, **34**, 2564-2569.

8 X. Q. Li, D. W. Elliott and W. X. Zhang, *Critical Reviews in Analytical Chemistry,* 2006, **31**, 111-122.

9 X. Q. Li and W. X. Zhang, *Langmuir,* 2006, **22**, 4638-4642.

10 X. Q. Li and W. X. Zhang, *Journal of Physical Chemistry C,* 2007, **111**, 6939-6946.

11 Commonly referred to as "zero valent iron"; see references 6 and 7

12 R. O. Lindsay and C. F. H. Allen, *Organic Syntheses,* 1955, **3**, 710.

13 Y. P. Sun, X. Q. Li, J. S. Cao, W. X. Zhang and H. P. Wang, *Advances in Colloid and Interface Science,* 2006, **120**, 47-56.

14 V. V. Rostovtsev, L. G. Green, V. V. Fokin and K. B. Sharpless, *Angewandte Chemie, International Edition in English,* 2002, **41**, 2596-2599.

15 X. Cui, Z. Li, C. Z. Tao, Y. Xu, J. Li, L. Liu and Q. X. Guo, *Organic Letters,* 2006, **8**, 2467-2470.

16 N. J. Agard, J. A. Prescher and C. R. Bertozzi, *Journal of the American Chemical Society,* 2004, **126**, 15046-15047.

17 A. T. Ngo and M. P. Pileni, *Journal of Physical Chemistry B,* 2001, **105**, 53-58.

18 B. D. Korth, P. Keng, I. Shim, S. E. Bowles, C. Tang, T. Kowalewski, K. W. Nebesny and J. Pyun, *Journal of the American Chemical Society,* 2006, **128**, 6562-6563.

19 D. A. Skoog, F. J. Holler and T. A. Neiman, *Principals of Instrumental Analysis*, 5 edn., Harcourt Brace, Orlando, 1998, p. 266.

20 F. A. Cotton and F. Wilkinson, *Advanced Inorganic Chemistry*, Wiley, Toronto, 1988, pp. 871, 878, 942.

Chapter 5: Removal of residual metal catalysts with iron/iron oxide nanoparticles from coordinating environments*

5.1 Introduction

Iron oxide capped iron nanoparticles ($Fe@Fe_xO_y$)[1] are known to sequester metal ions from aqueous[2-9] and organic media.[7] Research to date has primarily focused on applications in environmental contaminant remediation and removal of trace catalyst impurities from organic reaction products. Catalytic metal impurities remaining after synthesis can detrimentally affect later synthetic steps,[10-12] alter the properties of end-use materials,[13] and are a health concern if the end product is a phamaceutical.[14] Although the use of $Fe@Fe_xO_y$ has been briefly described as a technique for removing catalytic late-transition metal ions from organic reaction media,[7] this approach requires a more comprehensive study involving more relevant and complex metal homogeneous catalysts.

$Fe@Fe_xO_y$ are effective, straightforward to prepare, inexpensive, and their magnetic properties make them amenable to magnetic filtration. It is generally accepted $Fe@Fe_xO_y$ sequesters metal ions *via* a two-part mechanism. First, ions are coordinated to surface Fe-OH groups on the iron oxide. The iron core can then reduce the metals to their metallic state leading to extremely efficient sequestration. Presumably, this process will occur for any ion with a reduction potential more positive than that of iron, and hence gives access to many late transition metals and early main group metals.[2] Despite these favourable characteristics, it is reasonable that complex coordinating environments ubiquitous in the environment and reaction media would hinder efficient metal sequestration. Environmental aqueous media is often rife with phosphates, carboxylic acids and amines;[15, 16] and homogeneous metal catalysts are often ligated with phosphines and amines.[11, 17] Matrix effects have been studied for aqueous systems, and although there is evidence of matrix components promoting remediation,[16,18] more frequently coordinating species have been shown to hinder remediation of metal ions.[9, 18-21] It has been identified that coordinating media could seriously hinder the application of these materials in environmental remediation.[9, 18] The influences of ligating environments commonly found in organic reaction media have not been studied and could also limit the application of Fe@Fe_xO_y to sequestration of residual catalytic metals.

---

* Reproduced with permission J. E. Macdonald and J. G. C. Veinot, *Langmuir*, 2008, **24**, 7169-7177. Copyright 2008 American Chemical Society.

In Chapter 4, we showed that Fe@Fe_xO_y can be used to effectively sequester catalytic late transition metal ions from organic reaction products in organic media. This sequestration from reaction products was achieved in situations where catalytic ions were not coordinated to strongly binding ligands. However, some of the most powerful and useful homogeneous catalysts of Pd, Rh, and Ru (*e.g.*, Grubbs' catalyst (1st generation), Wilkinson's catalyst, as well as many palladium systems) employ strongly binding, bulky phosphines to prepare the active species,[22] tailor reactivity[10] and prevent plating out of zero oxidation state metal during the catalytic cycle.[17]

In this chapter, we present the development of a modification of our previous procedure to address the challenges associated with coordinating environments: the addition of small molecules such as 3-mercaptopropionic acid and cysteamine to aid the sequestration of phosphine containing catalysts from organic reaction products. We apply this technique to nickel,[23] rhodium,[24] ruthenium, [11] and palladium [25, 26] homogeneous and heterogeneous catalyzed reactions. We also present a discussion on the mechanism of sequestration under these new conditions.

5. 2 Experimental Procedures

5.2.1 Reagents

Tetrakis(triphenylphosphine) palladium(0) and tris(dibenzylideneacetone)-dipalladium(0) were purchased from Strem, aspartic acid and glycine from Fisher Scientific, potassium carbonate and cobalt(II) nitrate from Mallinckrodt, silver nitrate from Englehard, sodium borohydride, potassium hydroxide, ACS grade nitric acid from EMD Chemicals, sodium nitrite from ACP chemicals, rhodium(III) chloride hydrate from Colonial Metals, and potassium nitrate from BDH chemicals. The remaining reagents were purchased from Sigma-Aldrich. Reagents were used without further purification unless otherwise noted. Typically, in-house deionized water was employed for syntheses, whereas >18 MΩ·cm water was used for remediation studies. Sonication in this chapter refers to the use of a standard laboratory ultrasonic bath.

5.2.2 Synthesis of Fe@Fe_xO_y

Fe@Fe_xO_y were prepared using a modified literature procedure.[3, 7] Briefly, $FeCl_3 \cdot 6H_2O$ or $FeCl_3$ (21 mmol) was dissolved in 400 mL of deionized water. A solution of $NaBH_4$ (2.24 g, 59 mmol) in 30 mL of water was added dropwise while the iron (III) chloride solution was stirred vigorously. The orange solution became dark and a black precipitate formed. The precipitate was vacuum filtered and washed with 500 mL of deionized water followed by 50 mL of 95% ethanol. The resulting black paste was transferred to a round bottom flask and dried *in vacuo* for two days to yield a black powder that was stored in an argon-filled glovebox (< 0.1 ppm H_2O, 0.6 ppm O_2). Yield: 1.06 g.

5.2.3 Sequestration of in the absence of coordinating ligands

Solutions of metal salts, $Co(NO_3) \cdot 6H_2O$, $Ni(NO_3)_2 \cdot 6H_2O$, $Cu(NO_3)_2 \cdot 6H_2O$, $RhCl_3 \cdot xH_2O$, $Pd(NO_3)_2 \cdot H_2O$, and $PtCl_4$ were prepared at concentrations of ~13-26 mM of metal in 3×10^{-6} M KOH. Since hydroxide is known to cause the precipitation of the silver and ruthenium oxides,[27] $AgNO_3$ and $RuCl_3 \cdot xH_2O$ solutions were prepared in >18 MΩcm water. The Fe@Fe_xO_y powder was ground using a mortar and pestle to break up large aggregates and known quantities were placed in round bottom flasks in an argon-filled glovebox. Flasks were transferred to an argon-filled glovebag or Schlenk line where metal ion solutions were added to achieve ratios of 50 mg of Fe@Fe_xO_y per 10 mL of solution. The mixtures were capped and stirred. The solutions became colourless after several min, however stirring was continued for 40 h to ensure equilibrium conditions. Solids were removed by gravity filtration and gave colourless filtrates. The filtrates were acidified with nitric acid and analyzed by Quadropole-Inductively Coupled Plasma-Mass Spectroscopy (Quad-ICP-MS) for metal concentrations.

The recovered Fe@Fe_xO_y particles were washed with 40 mL of deionized water followed by 3 mL of 95% ethanol. For all sequestrations except silver, filter papers (Whatman No. 2) were dried in air at 50 °C and the solids collected for X-ray Photoelectron Spectroscopy (XPS). To prevent oxidation, particles used for silver sequestration were dried and maintained in inert atmosphere prior to analysis.

5.2.4 Small molecule additive screening

In a typical experiment, 5.00 mL of a 70-150 ppm (metal concentration) solution of the catalyst, 20 mmol of the additive small molecule, 0.5 mL of aqueous KOH solution (water, 0.2 mM, 0.4 M or 0.8 M) and 20 mg of Fe@Fe_xO_y were sonicated under static argon atmosphere for 1 h. Mixtures were subsequently centrifuged, gravity filtered and the solids washed 3× with THF. Solvents were evaporated, and 5.00 mL of concentrated HNO_3 was added. Metal concentrations were determined by Quad-ICP-MS. (Appendix D)

5.2.5 Application to metal catalyzed organic synthesis without ligands

Hydrogenation of cinnamic acid over Raney nickel [23]

Cinnamic acid 1.0 g (6.75 mmol) was dissolved in 40 mL of THF and added to 1.2 g of Raney nickel (washed with THF 3× under argon atmosphere) under argon atmosphere. The mixture was stirred vigorously under H_2 for 17 h. The solution was decanted and filtered through celite. Solvent was removed *in vacuo* giving a pale yellow solid, benzenepropanoic acid 0.8842g, 88% yield. ^1H NMR (400 MHz, $CDCl_3$): δ 7.17 (5H, m), 2.88 2H, t), 2.61 (2H, t). 0.1331 g of the product was placed in a crucible and heated in air to 625 °C for 16 h. Remaining solids were dissolved in 10.00 mL HNO_3 and tested for [Ni] by ICP-MS. [Ni] = 75 ppm with respect to the organic product.

Sequestration of Ni from benzenepropanoic acid

The crude product of the hydrogenation of cinnamic acid (256.5 mg), 100 mg of $Fe@Fe_xO_y$, 1 mL of 0.2 mM KOH and 13 mL of THF were stirred under argon atmosphere for 19 h. The mixture was gravity filtered and the solvent was removed *in vacuo*. 147 mg of the product was placed in a crucible and heated to 625 °C for 16 h. Remaining solids were dissolved in 10.00 mL HNO_3 and analyzed for nickel by Quad-ICP-MS. [Ni] = 75 ppm with respect to the organic product.

5.2.6 Application to metal catalyzed organic synthesis with phosphines present

Hydrogenation of (-)- Carveol over Wilkinson's Catalyst [24, 28]

(-)-Carveol (mixture of isomers) (1.0 mL, 6.2 mmol) and Wilkinson's Catalyst (chlorotris(triphenylphosphine) ruthenium(I)) (156 mg, 2.7 mol%) were dissolved in dry toluene in an argon atmosphere. The solution was stirred under H_2 (~1 atm) for 3.5 h over which time the orange solution turned brown. The solvent was removed *in vacuo* leaving a brown oil. GS-MS indicated a number of components in the reaction mixture identified as: 2-methyl-5-isopropylcyclohexanol (8%, m/z: 138, 95, 65), 2-methyl-5-isopropylcyclohex-2-eneol (two eluted peaks- diastereomers) (57%, m/z: 154, 139, 125, 111, 93, 82), carveol (10%, m/z: 152, 109, 82, 41), triphenylphosphine oxide (18%, 277, 210, 199, 71). Signals of the remaining components (7%) were insufficient to identify their structure.

63.1 mg of the products were heated to 200 °C under vacuum to remove most of the organic material. The remaining material was dissolved in 5.00 mL of concentrated HNO_3 and analyzed for Rh content. [Rh] = 4.98×10^3 ppm with respect to the organic products.

Heck coupling with $Pd(PPh_3)_4$ to yield methyl cinnamate [25]

Methyl acrylate (1.36 mL, 15 mmol), bromobenzene (1.05 mL, 10 mmol), $Pd(PPh_3)_4$ (288 mg, 2.5 mol%), potassium carbonate (2.72 g, 20 mmol), and DMF (10 mL) were stirred together and heated for 16 h. The solution turned black. The product was extracted in diethyl ether and washed with water three times. The remaining organic layer was gravity filtered leaving a yellow solution. Solvent was removed *in vacuo* to yield a yellow oil (1.14 g). Products were determined by GC-MS: methyl cinnamate (58%, m/z: 162, 131, 102, 77, 51), methyl 3,3-diphenylacrylate (26%, m/z: 238, 207, 178), triphenylphosphine oxide (16%, m/z: 277, 199, 152, 77).

73.5 mg of the product mixture was dissolved in 5.00 mL of concentrated HNO_3 and analyzed for Pd content by Quad-ICP-MS. [Pd]= 7.34 ppm with respect to the organic products.

Ring closing metathesis using Grubbs' Catalyst 1st Generation (10) to yield 4,4-dicarbethoxy-1-cyclopentene [11]

Diethyl diallylmalonate (240 µL, 1.00 mmol), Grubbs' Catalyst 1st Generation (40 mg, 5 mol%), and 100 mL of methylene chloride (distilled over CaH_2 and bubbled with argon), were stirred under argon for 2 h. Solvents were removed *in vacuo* leaving a brown oil. Quantitative yield of 4,4-dicarbethoxy-1-cyclopentene. ^1H NMR (400 MHz, $CDCl_3$): δ 5.60 (2H, t), 4.19 (4H, q), 3.01 (4H, s), 1.25 (6H, t). 15.3 mg of the product was dissolved in 5.00 mL of conc. HNO_3 and analyzed for Ru content by ICP-MS. [Ru]= 13.9 x 10^3 ppm with respect to the product.

Suzuki-Miyaura coupling by palladium catalysts to yield 4-nitrobiphenyl

a) 4-bromonitrobenzene (1.10 g, 5.44 mmol), phenylboronic acid (0.700 g, 1.05 eq), K_2CO_3 (1.89 g, 2.5 eq), $Pd_2(dba)_3$ (10.5 mg, 0.42 mol% Pd) were refluxed in degassed acetone 12.5 mL and water 12.5 mL under argon atmosphere for 2 h. The product was extracted with diethyl ether 3× and then washed with water 3×. The solution was gravity filtered and solvents removed *in vacuo*. Quantitative yield of 4-nitrobiphenyl. ^{1}H NMR (400 MHz, CD_3OCD_3): δ 8.37 (2H, m), 7.99 (2H, m), 7.82 (2H, m), 7.55-7.56 (3H, m). Purity was confirmed by GC-MS: m/z: 199, 152, 115, 76.

b) 4-bromonitrobenzene (1.11 g, 5.48 mmol), phenylboronic acid (0.699 g, 1.05 eq), K_2CO_3 (1.89 g, 2.5 eq), $Pd(PPh_3)_4$ (13.2 mg, 0.21 mol% Pd) were refluxed in degassed acetone 12.5 mL and water 12.5 mL under argon atmosphere for 12 h. The product was extracted with diethyl ether 3× and then washed with water 3×. The solution was gravity filtered and solvents removed *in vacuo*. 42% yield of 4-nitrobiphenyl by GC-MS. Crude mixture contained 53% *p*-bromonitrobenzene, 9% phenylboronic acid and 38% 4-nitrobiphenyl.

Sequestration of ligated catalytic metal impurities by $Fe@Fe_xO_y$ and small molecule additives

In a typical experiment, 80-170 mg of the crude product mixtures from metal catalyzed reactions were added to $Fe@Fe_xO_y$ (100 mg), 3-mercaptopropionic acid or cysteamine (100 mmol), 0.4 M $KOH_{(aq)}$ (2.5 mL) and THF (15-25 mL). The mixtures were stirred under argon for 19-20 h and gravity filtered. The isolated solids were washed with THF. If the filtrate was still cloudy, a second filtration was performed. Solvents were evaporated and most of the organic components were removed by heating above 150 °C under vacuum. The remaining solids were dissolved in a known quantity of concentrated HNO_3 with care. Note: NO_2 gas formed if the organic material was not completely removed by sublimation. Metal concentrations were analyzed by Quad-ICP-MS.

5.2.7 Characterization

Quad-ICP-MS

Quadropole Inductively Coupled Plasma- Mass Spectroscopy (Quad ICP-MS) was performed on a Perkin Elmer Elan 6000 ICP-MS. The flow rate on the instrument was 1 mL/min and dual detector mode was employed. A blank was subtracted after an internal standard correction and the values reported are an average of three readings (35 sweeps per reading). Concentrations typically have <6% relative standard deviation.

X-Ray Photoelectron Spectroscopy

X-Ray Photoelectron Spectroscopy (XPS) was performed on and AXIS-165 XPS spectrometer from Kratos Analytical. The source was either Mg operated at 140 W or monochromatic Al Kα X-rays at a power of 210 W. The base pressure in the analytical chamber was 10^{-6} - 10^{-7} Pa. The sample areas analyzed were 400 × 700 microns, with the analyzer normal to the surface. The pass energy for the survey spectra and the high-resolution spectra were 160 eV and 20 eV respectively. The instrument resolution is 0.4 eV. Samples were pressed into indium foil or carbon tape to prevent charging. Spectra were fitted using CasaXPS (VAMAS) software and were calibrated to the lowest binding energy component of the C 1s emission at 284.8 eV. Fitted peaks were 30% Lorentzian and 70% Gaussian with asymmetric peaks used for the fitted zero oxidation states in the metals. Metal zero oxidation state fittings had peak full widths at half maximum ranging from 0.8-1.6 eV. S 2p emission was fit using a spin-orbit couple area ratio of 2:1, line widths of 1.33-1.35 eV within the strongest peak and 3.3 in the higher binding energy peak. The separation between the spin-orbit couples of S 2p emission was set to 1.15 eV.[29]

5.3 Results and Discussion

5.3.1 Preparation of Fe@Fe_xO_y

Fe@Fe_xO_y were prepared by the aqueous sodium borohydride reduction of iron (III) chloride. They can be stored refrigerated in ethanol for extended periods of time or dry under inert atmosphere.[4] In this study, the Fe@Fe_xO_y were stored dry, in argon to facilitate quantification. The black, magnetic powder is comprised of multi-layered, pseudo-spherical, polydisperse particles with diameters between 20-80 nm.[7] Particle cores are amorphous iron and the shells have been identified as crystalline Fe_3O_4

terminated by surface Fe-OH groups.[30] Commonly, sequestrations are performed at pH > 8.5 to deprotonate Fe-OH groups and facilitate ion binding of the Fe@Fe_xO_y surface.[2-4]

5.3.2 Mechanistic studies in the absence of coordinating ligands

Fe@Fe_xO_y sequester metal ions by coordinating cations to surface Fe-OH groups. Remediation is aided, and its capacity increased, by the reduction of these coordinated ions to their metallic state by the iron core, but only when the E^o of the coordinated cations is more positive than iron (*vide supra*).[4] This dual remediation mechanism has been shown for many metals of environmental concern.[2-5, 9, 18-21] Surprisingly, it was recently reported in a study of the environmental remediation of technetium ions that the reduction mechanism is not as straightforward as first believed. X-ray Absorption Near Edge Spectroscopy (XANES) of supported Fe@Fe_xO_y recovered from Tc^{7+} sequestration showed no evidence of Tc(0) even though a comparison of electrochemical potentials predicts reduction to the metallic state. Instead evidence of reduction to only Tc^{4+} was observed.[9] In this context, we present evidence of the reduction of important catalytic late transition metals to their zero oxidation state as an antecedent to further investigation into the influence of coordinating environments.

When free metal ions in solutions were sequestered onto Fe@Fe_xO_y at approximately 5 mmol/g, the XPS clearly showed emissions arising from the presence of both the metallic and higher oxidation states (Figure 5-1).

The previous studies outlined in Chapter 4 were at lower concentrations of metal ions and did not provide adequate signal for such identification.[7] Even at the higher concentrations, we did not observe metallic oxidation states for silver and ruthenium when sequestration was performed in basic conditions (not shown). This may be understood considering salts of both of these metals are known to form insoluble oxides in the presence of hydroxide.[27] Contrary to Li and Zhang's earlier work,[4] both the metallic and +1 oxidation state for Ag were observed[31] when the sequestration was performed in neutral conditions. The Ru $3p_{3/2}$ emission did not allow confident assignment of oxidation states. Its presence, at the very least, is consistent with the accepted complexation mechanism. The metallic state was readily confirmed for all other metals investigated here.

It was also noted during these investigations that ion $E°_{M^{x+}/M}$ plays a significant role in the quantity of metal ion sequestered (Table 5-1). $Fe@Fe_xO_y$ (5 mg/mL) were added to aqueous solutions containing 13-27 mM of metal ion. We noted that initial concentrations of ions with E° values close to Fe^{2+} (*e.g.*, Co^{2+} and Ni^{2+}) were lowered much less than ions with much higher reduction potentials than Fe^{2+} (*e.g.*, Cu^{2+}, Pd^{2+}, Ag^{+}, Pt^{4+}, Rh^{3+}, Ru^{3+}).

It is difficult to formulate a quantitative relationship between particle sequestration capacity and metal ion oxidation potential. Analysis is complicated because the exact identities of the solution species are unknown; for example, "$RuCl_3$" is known to be a mixture of several ruthenium oxidation states[10] and $PtCl_4$ has been proposed to form $[PtCl_4(OH)_2]^{2-}$ in water.[27] Also, surface absorption provides a secondary mode of sequestration, which may depend more on hard-soft acid-base interactions[32] than E°.

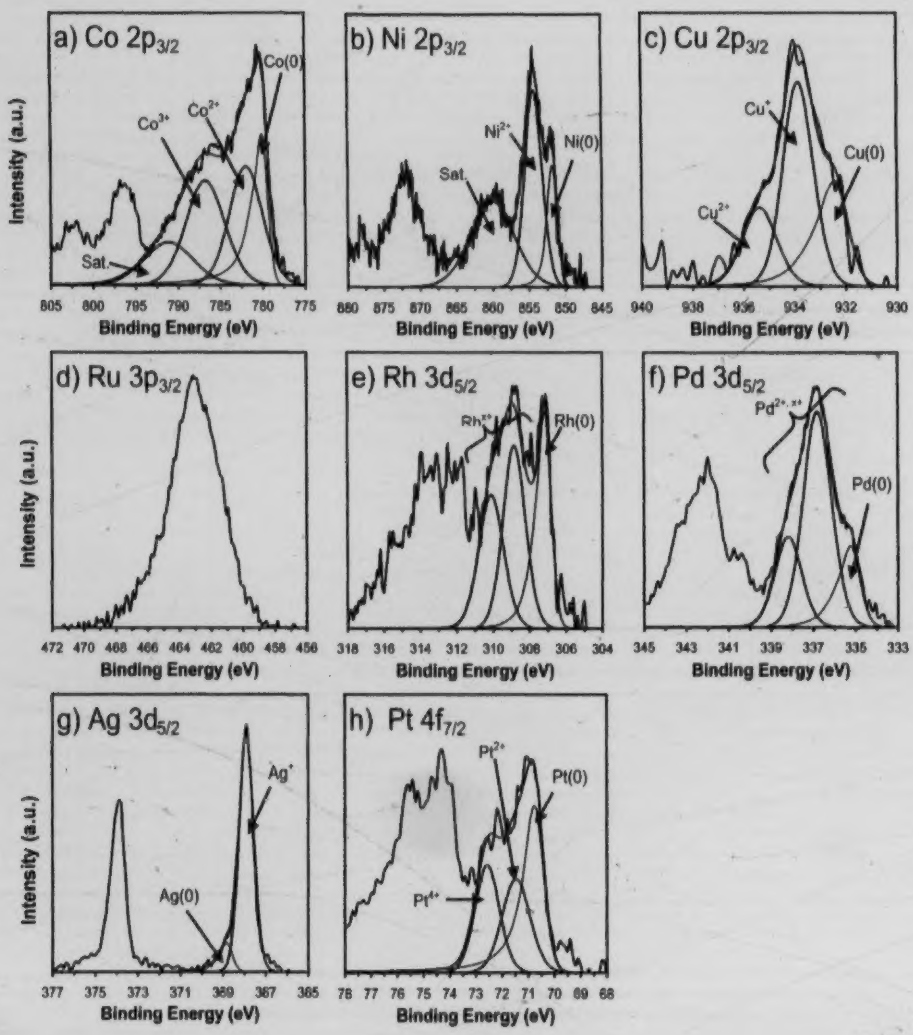

Figure 5-1 High resolution XPS of metals on Fe@Fe$_x$O$_y$ after being sequestered. Sequestration was of simple metal salts from aqueous solution. Only the highest spin state for each appropriate orbital was fitted as indicated. The sum of the fittings are highlighted in blue. Of the fittings, the zero oxidation state fittings are highlighted in red and peaks labeled Sat. are identified as satellites. Special note: g) These particles were handled continually under inert atmosphere to present a strong Ag(0) signal. A present, but less intense signal was observed for particles handled in air (not shown).

Table 5-1 Sequestration of metal ions from non-coordinating environments [a]

	Metal Source	E° (V)	Original [M] (mM)	Final [M] (mM)	% Sequestered
Co[b]	$Co(NO_3)_2 \cdot xH_2O$	-0.28	18	8.01	54.524
Ni[b]	$Ni(NO_3)_2 \cdot 6H_2O$	-0.257	19	5.40	71.170
Cu[b]	$Cu(NO_3)_2 \cdot xH_2O$	0.3419	19	0.97	94.991
Pd[b]	$Pd(NO_3)_2 \cdot xH_2O$	0.951	27	0.0005	99.998
Ag[c]	$AgNO_3$	0.7996	20	0.0009	99.996
Pt[d]	$PtCl_4$	0.718	13	0.000095	99.9993
Rh[e]	$RhCl_3 \cdot xH_2O$	0.758	17	0.000079	99.9995
Ru[f]	$RuCl_3 \cdot xH_2O$	0.386	26	0.00001	99.99997

a) $Fe@Fe_xO_y$ to solution ratio of 5 mg: 1 mL, E° are with respect to Standard Hydrogen Electrode. b) $M^{2+} + 2e^- \rightarrow M$, E° directly from Ref. (33). c) $Ag^+ + 1e^- \rightarrow Ag$ E° directly from Ref. (33). d) Approximated from the E° of $[PtCl_6]^{2-} + 2e^- \rightarrow [PtCl_4]^{2-}$ and $[PtCl_4]^{2-} + 2e \rightarrow Pt$ in Ref. (33). e) $Rh^{3+} + 3e^- \rightarrow Rh$ E° directly from Ref.(33). f) Ru approximated from the E° of $Ru^{2+} + 2e^- \rightarrow Ru$ and $Ru^{3+} + e^- \rightarrow Ru^{2+}$ in Ref. (33).

In all the presented cases, the sequestered metal ion $E^{\circ}_{M^{x+}/M}$ is greater than that of iron. Qualitatively, one would expect the vast excess of Fe(0) to reduce all of the metal. Clearly, this is not the case as a maximum capacity of metal ion that can be sequestered is observed. Although affiliated phenomena have been described using a band-bending approach,[4] in the context of the present discussion an electrochemical explanation[6] is more appropriate. Iron oxidation is proposed to be limited by ion mobility within the surface passivating oxide.[34, 35] Initially, electrons are free to tunnel to the surface of the particle and reduce the surface coordinated ions. As a result of the small dimensions of the iron core, every reduction results in a buildup of positive charge within the core, which cannot be relieved by the migration of ions. This process results in an additional anodic potential, E_{field}. The resultant electrochemical cell is described as:

$$E_{cell} = E^{\circ}_{M^{x+}/M} - E_{Fe^{3+}/Fe} - E_{field}$$

Where E_{cell} is the effective cell potential, $E^{o}_{M^{x+}/M}$ and $E_{Fe^{3+}/Fe}$ are the half cell potentials of the sequestered metal M, and iron, respectively. Provided the E_{cell} remains positive, metal ion reduction is spontaneous. For a more positive $E^{o}_{M^{x+}/M}$, the potential of E_{field} is correspondingly larger when $E_{cell} = 0$ and reduction of the surface metal is arrested. As a result, more electrons have left the core before reduction becomes no longer spontaneous. Hence, metals with more positive $E^{o}_{M^{x+}/M}$ (Pt, Pd, Ag), qualitatively, are reduced and sequestered more effectively than those with E^{o} closer to that of iron (Co, Ni).

5.3.3 Application to heterogeneous and simple homogeneous catalysts

Heterogeneous catalysts, in principle, circumvent challenges associated with removing dissolved catalysts. Still, some heterogeneous catalysts such as Raney nickel[36] and palladium on carbon commonly leach metal impurities into solution and, as a result, the desired reaction product.[17]

Sequestration of leached nickel with $Fe@Fe_xO_y$ from the product mixture obtained from the hydrogenation of cinnamic acid (1) using Raney nickel was performed. The nickel content in the product mixture was reduced from 75 ppm to 15 ppm (Scheme 5-1). Unfortunately, high resolution XPS of the recovered $Fe@Fe_xO_y$ particles indicated the presence of nickel, but the emission intensity was insufficient to assign oxidation states (Figure 5-2).

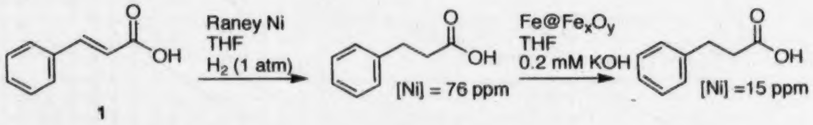

Scheme 5-1 Hydrogenation of cinnamic acid (**1**) over Raney nickel followed by the sequestration of leached nickel by Fe@Fe$_x$O$_y$

In contrast, we report clear evidence for coordination and reduction mechanisms for the sequestration of copper from the product of a "Click" copper(II) sulphate catalyzed azide-alkyne [3+2] cycloaddition (as described in Chapter 4). The product was contaminated much more so than in the Raney nickel case. The concentration of copper in the product was lowered from 2026 ppm to 16 ppm in one step.[7] High resolution XPS of the recovered particles clearly showed a Cu 2p$_{3/2}$ emission which was characteristic of Cu(0), Cu^{1+}, Cu^{2+} (Figure 5-2).

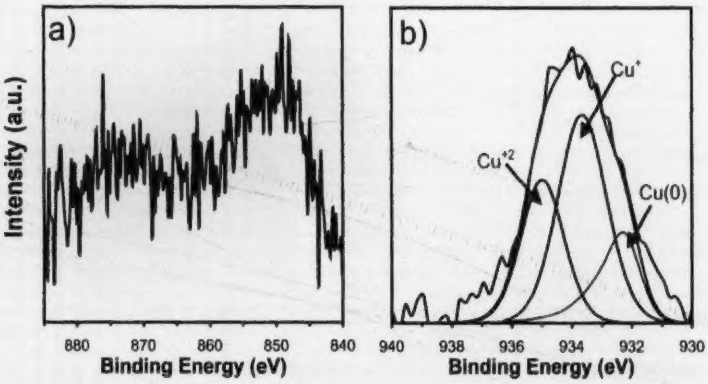

Figure 5-2 a) XPS Ni 2p region of Fe@Fe$_x$O$_y$ after sequestering nickel leached from a hydrogenation over Raney nickel. Not background subtracted. b) XPS Cu 2p region of Fe@Fe$_x$O$_y$ after sequestering copper from a "click" cycloaddition. The asymmetric 0 oxidation state fitting are highlighted in red and the sum of the fittings are highlighted in blue.

5.3.4 Challenges associated with strongly coordinating ligands

In Chapter 4, we showed that solutions of catalytic metals (100 ppm) could be sequestered with Fe@Fe_xO_y so that > 99% of the metal ions are removed.[7] In contrast, and not surprisingly, our experiments indicated that Fe@Fe_xO_y alone does not efficiently sequester catalytic metals (70-150 ppm in THF) in the presence of coordinating phosphines. Here we report sequestration studies of synthetically important tetrakistriphenylphosphine palladium(0) ($Pd(PPh_3)_4$), Grubbs' Catalyst 1st generation ($Ru(PCy_3)_2ClCH_2CH_3$), and Wilkinson's Catalyst ($Rh(PPh_3)_3Cl$). In addition, qualitative tests indicated the Fe@Fe_xO_y sequestration of palladium(II) acetate ($Pd(OAc)_2$) was progressively inhibited by increased concentrations of triphenylphosphine and to a lesser degree by tributylphosphine oxide (Appendix D). We propose bulky, tightly-binding phosphines hinder the necessary intimate contact between the solution-borne catalytic metal ions and the Fe@Fe_xO_y surface, which is a requirement for both surface coordination and reduction mechanisms of the present technique.

To address this problem, a series of amino acids and other small molecules were screened as potential competitive coordinating ligands as additives to the sequestration mixture. Candidate ligands were chosen (glycine (**2**), lysine (**3**), aspartic acid (**4**), cysteine (**5**), trithiocyanuric acid (**6**)) based on their capability to coordinate catalytic metals ions through free amine, thiol or carboxylic acid functional moieties and simultaneously interact with Fe@Fe_xO_y surfaces with free carboxylic acid groups. Trithiocyanuric acid was also chosen because of its known affinity to bind palladium yielding an insoluble solid.[37] Cysteine consistently proved among the most effective additive for sequestration in our initial experiments (Table 5-2). (Appendix D)

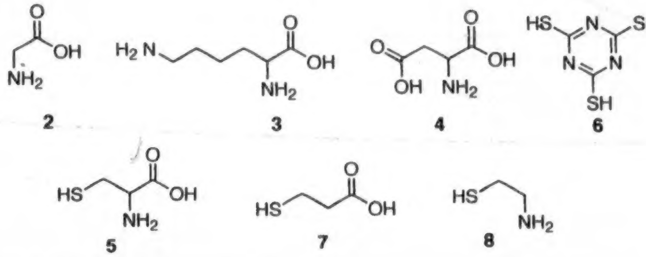

Scheme 5-2 Small molecule additives screened for aiding Fe@Fe$_x$O$_y$ sequestration of phosphine containing metal catalysts

Table 5-2 Sequestration of 40-150 ppm solutions of metal-phosphine catalysts using Fe@Fe$_x$O$_y$ and aided by small molecules[a]

Small molecule additive	Grubbs' Catalyst % Removed	Pd(PPh$_3$)$_4$ % Removed	Wilkinson's Catalyst % Removed
Fe@Fe$_x$O$_y$ only	35	12	43
Glycine (**2**)	46	35	54
Lysine (**3**)	46	82	54
Aspartic acid (**4**)	26	22	31
Cysteine (**5**)	64	99.6	91
Trithiocyanuric acid (**6**)	17	41	38
3-Mercaptopropionic acid (**7**)	98	99.5	77
Cysteamine (**8**)	96	90	32

[a] 5 mL of metal-catalyst THF solution, 20 mg of Fe@Fe$_x$O$_y$, 20 mmol of the small molecule, and 0.5 mL of 0.02 mM KOH.

The apparent efficiency with which the cysteine/Fe@Fe$_x$O$_y$ mixture sequestered metals raised questions regarding the interactions between cysteine, catalytic metal ions and the Fe@Fe$_x$O$_y$ surfaces. A series of blank experiments and sequestrations using structurally similar molecules to cysteine were performed; ligands were chosen to interrogate the role of functional groups on cysteine. Each ligand chosen was missing one of the cysteine functional groups: glycine (no thiol), 3-mercaptopropionic acid (**7**) (no amine) and cysteamine (**8**) (no carboxylic acid). The impact of these additive ligands on the ability of the Fe@Fe_xO_y to sequester Grubbs' Catalyst, $Pd(PPh_3)_4$, and Wilkinson's Catalyst are summarized in Table 5-2. Of particular note, and to put the following discussion in context, Fe@Fe_xO_y alone merely decreases Grubbs' Catalyst, $Pd(PPh_3)_4$, and Wilkinson's Catalyst concentrations by 35%, 12% and 43%, respectively.

The glycine/Fe@Fe_xO_y combination marginally increased the sequestration efficiency of Fe@Fe_xO_y alone, however fell short of the thiol-containing systems. These observations highlight the importance of the thiol moiety and are consistent with the relative thiophilic bonding characteristics of the Ru, Rh, and Pd predicted by Pearson's Hard-Soft acid base theory.[38]

3-Mercaptopropionic acid and cysteamine used in combination with Fe@Fe_xO_y met or exceeded the sequestration abilities of cysteine/Fe@Fe_xO_y mixtures (Table 5-2). Although both were effective, 3-mercaptopropionic acid was consistently more potent in facilitating the sequestration of phosphine containing metal catalysts by Fe@Fe_xO_y.

Cysteine, in the ~10:1 THF:water solvent system employed here, did not require iron particles to sequester the metal ions as a non-magnetic insoluble material. Typically, sequestrations using cysteine alone lowered the concentrations of Grubbs' Catalyst and $Pd(PPh_3)_4$ by 63% and 99.9%, respectively. This data is comparable to those obtained when the Fe@Fe_xO_y was present (Table 5-2) and are consistent with patent literature that report aqueous solutions of cysteine can extract catalytic metals from hydrophobic solutions.[37, 39] In these cases, the Fe@Fe_xO_y provided no added benefit presumably because the precipitation of the metal ions as a complex with cysteine prevented interaction with the Fe@Fe_xO_y.

In contrast to the cysteine case, a strong synergistic effect was observed when Fe@Fe_xO_y was employed in combination with 3-mercaptopropionic acid and cysteamine. Sequestration without Fe@Fe_xO_y, and only 3-mercaptopropionic acid or cysteamine provided 26% and 84% removal, respectively, for Grubbs' catalyst, and 45 and 85%, respectfully, for $Pd(PPh_3)_4$, and 21% for both for Wilkinson's catalyst. These results were strikingly improved when Fe@Fe_xO_y was also present (Table 5-2). Replacing Fe@Fe_xO_y with and equal mass of a common filtering agent such as celite or carbon black in the presence of cysteamine or 3-mercaptopropionic acid provided markedly inferior results (Table 5-3), further highlighting the importance of the synergistic influences of Fe@Fe_xO_y and thiol containing molecules.

Table 5-3 Percent removal of phosphine-coordinated metals using common filtering agents and small molecule additives [a]

		cysteamine	3-mercaptopropionic acid
Grubbs' Catalyst	Celite	75%	80%
	Carbon Black	77%	77%
$Pd(PPh_3)_4$	Celite	76%	99.93%
	Carbon Black	62%	99.95%

[a] Experiments were carried out as outlined in Section *5.2.4 Small molecule additive screening* with 20 mg of filtering agent replacing Fe@Fe_xO_y.

Further investigations indicated the addition of 1-2 equivalents (compared to the small molecule additive) of KOH to the reaction mixture increased the sequestration efficiency for 3-mercaptopropionic acid and cysteamine (Table 5-4). Usually, sequestration of cations by Fe@Fe_xO_y are preformed above the zeta potential (~ $pH_{zp} > 8$)

of the particles to induce negatively charged surfaces that have a higher infinity for metal cations.[40] Here, it has been demonstrated that aqueous sequestration of Ag^+ and Ru^{3+} can be performed in neutral conditions (*vide infra*) and pH dependant sequestration studies in aqueous media with simple metal salts have been performed elsewhere.[4] For the present case, the addition of base may have improved sequestration by deprotonating the small molecule thiol moiety, thereby increasing its affinity toward the catalytic metal ions. Similar sequestration abilities were not observed for cysteamine and 3-mercaptopropionic acid, which would have been consistent with this hypothesis. An alternative explanation for the observed improvement in sequestration efficiency lies in the basic media deprotonating carboxylic acid, thiol or ammonium cations of the additive molecules. In doing so, the affinity of additives to the $Fe@Fe_xO_y$ surfaces is increased. In turn, this makes the catalyst metals ligated to the additive molecules more amenable to immobilization on the $Fe@Fe_xO_y$ and increases sequestration efficiency. This hypothesis is consistent with the observation of differing sequestration abilities of 3-mercaptopropionic acid and cysteamine as different moieties have differing bonding strengths to iron oxide surfaces.[41, 42]

Table 5-4 Effect of pH on percent removal of phosphine-coordinated metals using $Fe@Fe_xO_y$ and small molecule additives.

	Wilkinson's Catalyst		$Pd(PPh_3)_4$		Grubbs' Catalyst	
[KOH][b]	cysteamine	3-mercapto-propionic acid	cysteamine	3-mercapto-propionic acid	Cysteamine	3-mercapto-propionic acid
Water			90%	99.20%	91%	96%
0.2 mM	32%	77%	91%	99.60%	96%	98%
0.4 M	53%	90%	92%	99.94%		98%
0.8 M			92%	99.30%		

[a] Experiments were carried out as outlined in Section *5.2.4 Small molecule additive screening.* [b] [KOH] is in reference to the concentration in the 0.5 mL water aliquot added to each reaction.

5.3.5 Application to homogeneous catalysis

Having established that 3-mercaptopropionic acid or cysteamine facilitates sequestration of catalytic metals in the presence of strongly binding ligands, it was important to apply the present methodology to the metals following a catalytic reaction. It is known that catalysts may undergo complicated degradation processes[22, 43] and a mixture of unidentified metal species of varying oxidation states is likely. For this reason, our approach was applied to the reaction mixtures resulting from synthetically relevant reactions including: a Heck coupling catalyzed by $Pd(PPh_3)_4$,[25] a ring closing metathesis catalyzed by Grubbs' catalyst,[11] a hydrogenation catalyzed by Wilkinson's catalyst,[24, 28] and Suzuki-Miyaura couplings catalyzed by either tris(dibenzylideneacetone)dipalladium(0) ($Pd_2(dba)_3$) or $Pd(PPh_3)_4$.[26] The sequestration of the residual metal impurities from the crude reaction mixtures were performed using a 10:1 THF to 0.4 M $KOH_{(aq)}$ ratio, and 18 mM in 3-mercaptopropionic acid or cysteamine.

(-)-Carveol (**9**) was hydrogenated using Wilkinson's catalyst[24, 28] and the resulting crude product mixture was contaminated with 4.98×10^3 ppm of rhodium. Sequestration of rhodium by $Fe@Fe_xO_y$ and aided by 3-mercaptopropionic acid (**7**) provided a 74% decrease in the concentration of rhodium. The addition of cysteamine (**8**) only allowed for a 6% decrease in rhodium concentration from the product mixture (Scheme 5-3a). This is consistent with the observations seen in the screening tests (*vide supra*). Prompted by the consistently poorer results obtained when adding cysteamine, it was decided to focus on the employment of 3-mercaptopropionic acid.

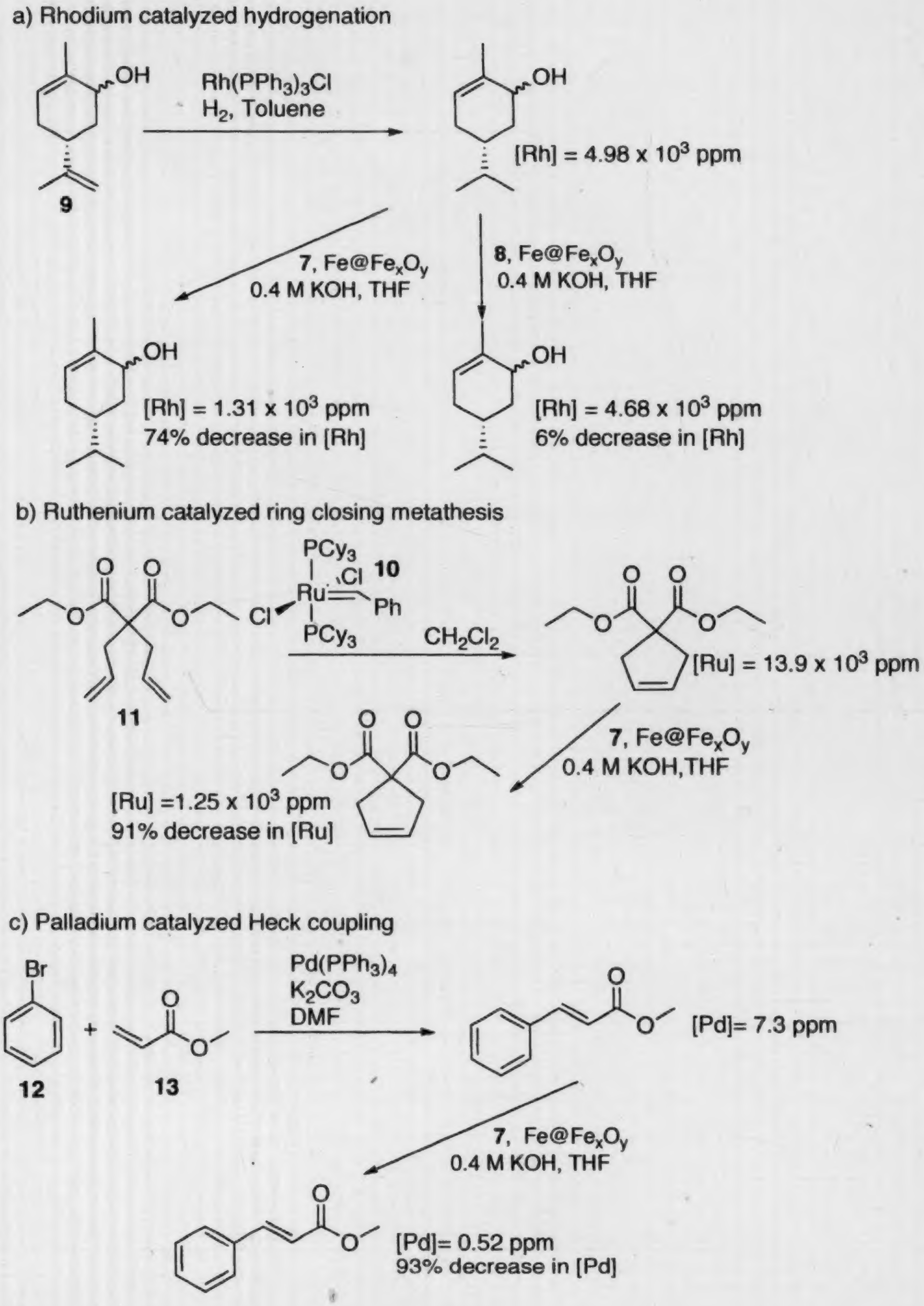

a) Rhodium catalyzed hydrogenation

b) Ruthenium catalyzed ring closing metathesis

c) Palladium catalyzed Heck coupling

9
OH
$Rh(PPh_3)_3Cl$
H_2, Toluene
[Rh] = 4.98 x 10^3 ppm
7, $Fe@Fe_xO_y$
0.4 M KOH, THF
8, $Fe@Fe_xO_y$
0.4 M KOH, THF
[Rh] = 1.31 x 10^3 ppm
74% decrease in [Rh]
[Rh] = 4.68 x 10^3 ppm
6% decrease in [Rh]
11
PCy_3
Cl
10
Ru
Ph
PCy_3
CH_2Cl_2
[Ru] = 13.9 x 10^3 ppm
7, $Fe@Fe_xO_y$
0.4 M KOH,THF
[Ru] =1.25 x 10^3 ppm
91% decrease in [Ru]
Br
12
13
$Pd(PPh_3)_4$
K_2CO_3
DMF
[Pd]= 7.3 ppm
7, $Fe@Fe_xO_y$
0.4 M KOH, THF
[Pd]= 0.52 ppm
93% decrease in [Pd]

Scheme 5-3 Phosphine-Metal Catalyst sequestration by $Fe@Fe_xO_y$ and 3-mercaptopropionic acid (7) or cysteamine (8).

A ring closing metathesis by Grubbs' catalyst (1st Generation) (**10**) of diethyl diallylmalonate (**11**) was performed according to a literature procedure[11] affording product containing 13.8 × 10^3 ppm of ruthenium. Sequestration of ruthenium from the product by Fe@Fe_xO_y and 3-mercaptopropionic acid provided a 91% decrease in the concentration of ruthenium (Scheme 5-3b). Furthermore, palladium in the product of a Heck coupling catalyzed by $Pd(PPh_3)_4$[25] was sequestered by similar conditions giving a 93% decrease in palladium content (Scheme 5-3c).

Lastly, residual palladium within the product mixture of the Suzuki-Miyaura coupling of 4-bromonitrobenzene (**12**) and phenylboronic acid (**13**) was sequestered (Scheme 5-4). When either $Pd_2(dba)_3$ or $Pd(PPh_3)_4$ were employed as catalysts, and after incidental palladium black was removed by filtration, the resulting products were contaminated with 12.8 ppm and 91.2 ppm respectively. $Pd_2(dba)_3$ was the more active catalyst (as evidenced by a greater yield and shorter reaction times) and also provided less palladium contamination in the product. Upon sequestration of the two product mixtures by Fe@Fe_xO_y, a 55% reduction in palladium concentration was observed for the $Pd_2(dba)_3$ catalyzed product and 37% reduction for the $Pd(PPh_3)_4$ catalyzed product mixture. This can be understood by dibenzylideneacetone being a weaker ligand than triphenylphosphine in highly ligated palladium[26] and therefore is more readily displaced by Fe-O^- functionalities on the iron surface. The product mixture achieved by $Pd(PPh_3)_4$ was also treated with Fe@Fe_xO_y and 3-mercaptopropionic acid. In this case, the result was excellent: a decrease of palladium concentration by 97%, leaving 2.3 ppm in the product mixture (Scheme 5-4). Of particular note, reduction of the product 4-nitrobiphenyl (**14**) to 4-aminobiphenyl,[44, 45] even after 20 h of exposure to the iron, was observed by GC-MS to be as low as 3%. Further prevention of the formation of the amine is possible by increasing the pH of the solution and by optimizing sequestration times.

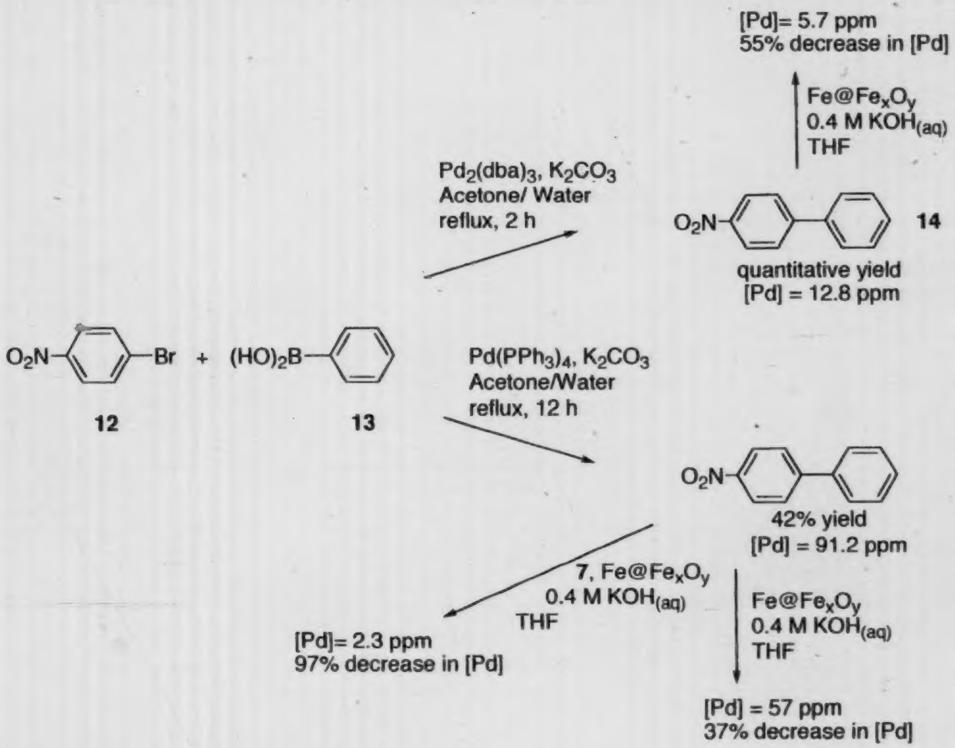
[Pd]= 5.7 ppm
55% decrease in [Pd]
Fe@Fe$_x$O$_y$
0.4 M KOH$_{(aq)}$
THF
Pd$_2$(dba)$_3$, K$_2$CO$_3$
Acetone/ Water
reflux, 2 h
O$_2$N
14
quantitative yield
[Pd] = 12.8 ppm
O$_2$N
Br
+
(HO)$_2$B
12
13
Pd(PPh$_3$)$_4$, K$_2$CO$_3$
Acetone/Water
reflux, 12 h
O$_2$N
42% yield
[Pd] = 91.2 ppm
7, Fe@Fe$_x$O$_y$
0.4 M KOH$_{(aq)}$
THF
[Pd]= 2.3 ppm
97% decrease in [Pd]
Fe@Fe$_x$O$_y$
0.4 M KOH$_{(aq)}$
THF
[Pd] = 57 ppm
37% decrease in [Pd]

Scheme 5-4 Application of Fe@Fe$_x$O$_y$ to the sequestration of Pd from Suzuki-Miyaura couplings.

5.3.6 XPS studies of $Fe@Fe_xO_y$ after sequestration of phosphine coordinated catalysts

Knowing the presence of 3-mercaptopropionic acid or cysteamine was necessary to achieve effective sequestration with $Fe@Fe_xO_y$, it was unknown if the additives allowed for reduction of the metals onto the particle surfaces. The bifunctional molecules were chosen on the premise that one functionality would bond to the catalytic metal and the other to the iron surface (*vide supra*). The specific role of the small thiol containing molecules had yet to be confirmed.

High resolution XPS spectra of $Fe@Fe_xO_y$ following sequestration were obtained for the appropriate regions for C, O, P, S, N, Fe and the catalytic metals. Consistent with literature reports, the Fe 2p spectra of the particles before sequestration showed evidence of Fe(0), Fe^{2+}, and Fe^{3+}; following sequestration, the Fe(0) peak was no longer present or greatly reduced in intensity (Figure 5-3). This may result from oxidation by metal cations or by extended exposure to air. [4]

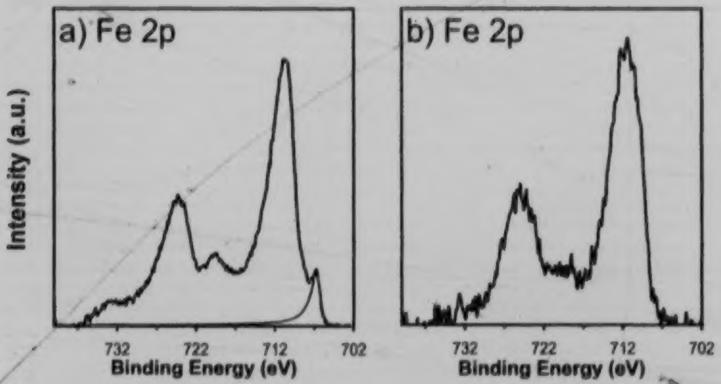

Figure 5-3 Representative XPS Fe 2p region of $Fe@Fe_xO_y$ a) before sequestration (with 0 oxidation state fitting highlighted in red) and b) after sequestration.

High resolution spectra of the P 1s region (128 -140 eV) did not give a signal above the background, consistent with the complete exchange of phosphine ligands on the metal catalysts sequestered.

Typical O 1s spectra of the Fe@Fe$_x$O$_y$ following sequestration present a broad peak containing several components (Figure 5-3). The emissions at 530.9 eV and 532.4 eV can be assigned to O^{2-} from the Fe$_x$O$_y$ and the surface Fe-OH functionalities, respectively.[46] The highest binding energy at 533.6 eV component is resultant from surface-adsorbed carboxylate[46] when 3-mercaptopropionic acid was present (Figure 5-4). This component is correspondingly absent when cysteamine was employed (Figure 5-4b). We did not closely examine the O 1s spectra from samples containing Pd as there is spectral overlap between the O 1s and Pd 3p spectral lines.[47] Other unidentified components may also be present. From the spectra we can conclude for Fe@Fe$_x$O$_y$ used with 3-mercaptopropionic acid, the carboxylate group is bound to the iron surface.

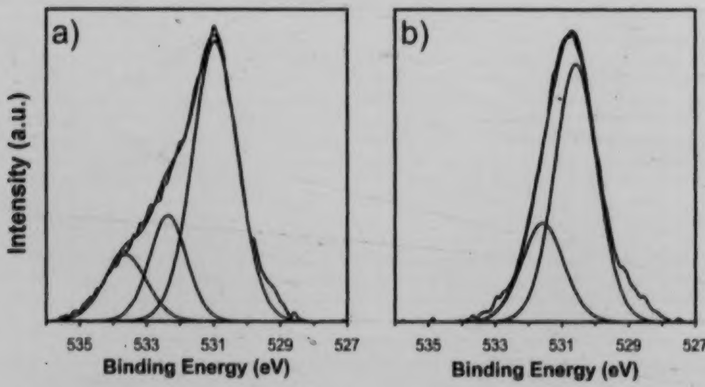

Figure 5-4 Representative XPS O 1s region of Fe@Fe$_x$O$_y$ following sequestration of catalytic metals aided by a) 3-mercaptopropionic acid and b) cysteamine. The sum of the fittings are highlighted in blue.

The N 1s emission of the Fe@Fe$_x$O$_y$ following sequestration in the presence of cysteamine shows a clear indication of the amine being bonded to the iron oxide surfaces under near neutral conditions, but not at higher pH. When sequestration was performed close to neutral conditions, two high binding energy peaks were fitted at 400.2 eV and 401.4 eV (Figure 5-5a). These values are consistent with two different binding modes of aliphatic amines with metal/metal oxide surfaces.[46] The lowest binding energy component at ~398.9 eV under near neutral conditions is also the only component observed when sequestration was performed with 1 equivalent of base (Figure 5-5b). This value is ~2 eV lower than literature values for protonated amines and ~1 eV lower than alkyl amines bonded to a surface.[46] This component is most likely caused by free amine with the binding energy lowered by induction effects arising from negatively charged thiolate nearby on the molecule. This shift to lower binding energy is similar to literature for EDTA and its salts.[48] The presence of free amine indicates, by deduction, some thiol of the cysteamine must be bonded to the surface at low pH and only thiol is bonded to the Fe@Fe$_x$O$_y$ surface at high pH. At low pH, there is also some coordination of the amine to the Fe@Fe$_x$O$_y$ surfaces. The addition of base deprotonates the thiol (RSH) to yield thiolate (RS$^-$) increasing its affinity for the Fe@Fe$_x$O$_y$ surfaces (*vide infra*) at high pH.

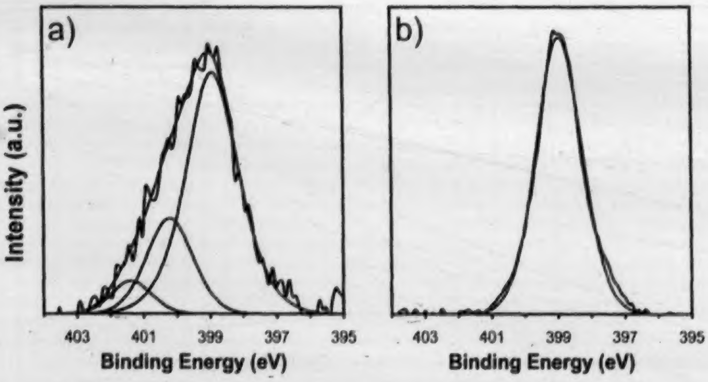

Figure 5-5 Representative XPS N 1s region of Fe@Fe$_x$O$_y$ following sequestration of catalytic metals aided by cysteamine at a) near neutral conditions b) 1 equivalent added KOH. The sum of the fittings are highlighted in blue.

The S 2p XPS is consistent with the conclusions drawn from the O 1s and N 1s spectra for Fe@Fe$_x$O$_y$ after sequestration with 3-mercaptopropionic acid and cysteamine, respectively. The dominant S 2p XPS emission arising from the Fe@Fe$_x$O$_y$ after a sequestration of a metal catalyst in the presence of cysteamine or 3-mercaptopropionic acid contained two broad peaks and were fit with spin-orbit couples (Figure 5-6). For Fe@Fe$_x$O$_y$ used with 3-mercaptopropionic acid for sequestration, four couples were fitted (Figure 5-6a). The binding energy of the lowest energy couple (162.0 and 163.2 eV) is shifted ~1.7 eV lower than what is reported for free thiol, indicating the presence of thiolate (RS$^-$).[49] The middle spin orbit couple fitted (163.2 and 164.4 eV) lies between free thiol and thiolate[49] and we propose is resultant from species bound to the particle surfaces or the catalytic metal cations. The emission couple at 163.7 and 164.9 eV agrees with literature values for free thiol.[49] Often another broad peak was observed at higher binding energy (166.7 and 167.80 eV) consistent with oxidation of thiolate to the sulfonate anion (RSO$_2$O$^-$).[29, 49, 50]

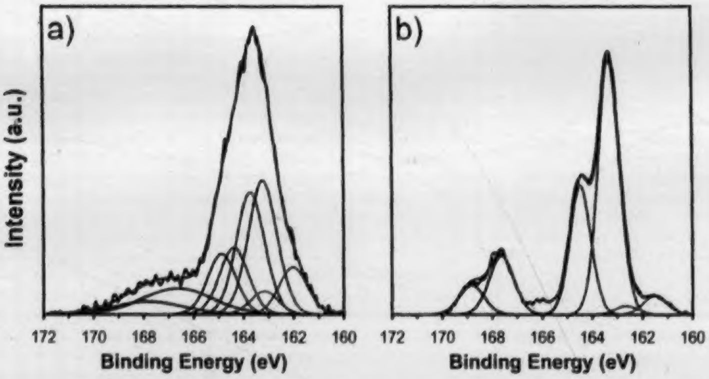

Figure 5-6 Representative XPS S 2p region of Fe@Fe$_x$O$_y$ following sequestration of catalytic metals aided by a) 3-mercaptopropionic acid and b) cysteamine. Spin-orbit couples are fitted and indicated by matching colour. Sums of the fittings are highlighted in blue.

The addition of base caused the relative intensities for the S 2p couples to be different for the cysteamine and 3-mercaptopropionic acid cases. For Fe@Fe$_x$O$_y$ used with cysteamine with 1 equivalent of KOH added, unlike 3-mercaptopropionic acid, the S 2p spectra did not include the emission couple designated for free thiol (Figure 5-6b). We postulate this change is due to the differing effects of the added KOH on cysteamine and 3-mercaptopropionic acid. (For reference, we note that cysteine has pKa =1.7 (-COOH), 8.3 (-SH), 10.8 (-NH$_3^+$))[51] For 3-mercaptopropionic acid, adding base will deprotonate the carboxylic acid before the thiol, leaving some free thiol. For cysteamine, because there is no carboxylic acid, the addition of base causes deprotonation of the thiol to thiolate. When base was not added, an emission couple for free thiol was observed for cysteamine.

Previously, it has been have shown that iron oxide particles preferentially bind to organic acids over thiol groups.[41] From this, we can infer the S 2p component of intermediate binding energy is due to the thiol bonded the catalytic metal ions for 3-mercaptopropionic acid and not to the Fe@Fe_xO_y surfaces. For cysteamine, the strong relative intensity of the S 2p bonded component compared to the lower binding energy free thiolate, indicates the thiol is bonding to the iron surface as well as to the catalytic metal cations. This is consistent with the N 1s spectra of Fe@Fe_xO_y recovered after sequestration with cysteamine (*vide supra*). At low pH, some amine is bonded to the Fe@Fe_xO_y surface, but at high pH, only free amine is observed.

From both the S 2p and N 1s spectra for cysteamine, we conclude the amine functionality is bonded to the particle surfaces at low pH and the thiol is bonded to the catalytic metal ions. At higher pH, the thiol may also bond to the iron surface (*vide supra*). These results are consistent with the poorer sequestration obtained when cysteamine is used instead of 3-mercaptopropionic acid; the literature has presented evidence for carboxylic acids binding more strongly to iron oxides than amines[42] and thiols.[41] This leads us to postulate sequestration is not limited by the replacement of the phosphines on the catalytic metals by thiol, but rather by how strongly the other functionality of the additive molecule binds to the Fe@Fe_xO_y surfaces enabling immobilization of the catalytic metal.

When Wilkinson's catalyst was sequestered by Fe@Fe_xO_y a contribution from Rh(0) was only seen for samples that were sonicated rather than stirred (Figure 5-7). This low binding energy component, if present, was a fraction of the total Rh $3d_{5/2}$ signal (<10%). This is in stark contrast to the Rh(0) component observed for aqueous remediation without coordinating ligands present (~25%) (Figure 5-1).

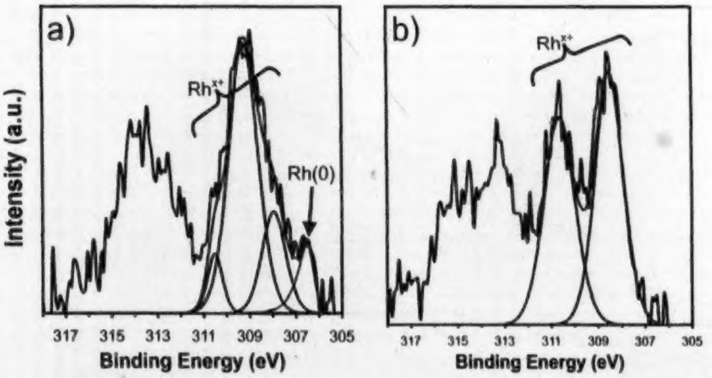

Figure 5-7 Example XPS Rh 3d region of Fe@Fe$_x$O$_y$ after sequestration of Wilkinson's catalyst aided by small thiol containing molecules a) by sonication b) by stirring. The sum of the fittings are in blue and the 0 oxidation sate fitting in a) is highlighted in red.

Unlike Wilkinson's catalyst, when Pd(PPh$_3$)$_4$ was sequestered by Fe@Fe$_x$O$_y$ and one of the thiol containing small molecules, regardless of sample handling, there was no evidence of Pd(0) on the iron particles by XPS. Only the higher oxidation states were observed (Figure 5-8). These results suggest 3-mercaptopropionic acid and cysteamine, like phosphines, prevent intimate contact between the particle surface and catalytic metal, thus inhibiting reduction of the catalytic metal by the iron particles. We propose the high energies associated with sonication provided sufficient lability of the thiol-Rh bonds for the iron oxide surfaces to bind the catalytic metals and allow for reduction.

Figure 5-8 Example XPS Pd 3d region of Fe@Fe$_x$O$_y$ after sequestration of Pd(PPh$_3$)$_4$ catalyst aided by small thiol containing molecules. The sum of the fittings are highlighted in blue.

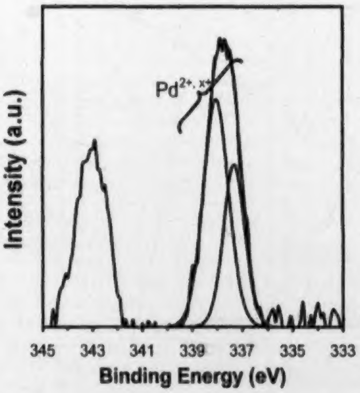

5.4 Conclusions

Coordinating environments for contaminant metals, such as phosphine stabilized ruthenium, rhodium, palladium, have a drastic effect on the sequestration capabilities of $Fe@Fe_xO_y$. The problem can be overcome by the addition of some thiol-containing small molecules such as cysteamine and, more effectively, 3-mercaptopropionic acid. The inclusion of a thiol group was imperative to displace the phosphines on the catalyst metals and promote sequestration by $Fe@Fe_xO_y$.

In the sequestration of simple metal salts from aqueous media and organic reaction products, some reduction of cobalt, copper, nickel, rhodium, palladium, silver and platinum was observed (results were inconclusive for ruthenium). The amount of metal sequestered per mass of $Fe@Fe_xO_y$ was shown to increase with increasing electrochemical half-cell potential of the cation in question. This phenomenon is understood by an electrochemical explanation where sequestration is limited by ion immobility in the oxide shell and a build up of charge in the iron core.

However, for systems containing phosphines in the remediation of metals by $Fe@Fe_xO_y$ and small thiol containing molecules, redox behaviour was less dominant. Reduction to the metallic oxidation state was only observed for Wilkinson's catalyst and only when the sample was exposed to sonication. In all other similar cases studied, inhibition of the reduction mechanism was observed.

The modified sequestration technique, where $Fe@Fe_xO_y$ is added in conjunction with 3-mercaptopropionic acid, was applied successfully to the product mixtures of a Heck coupling catalyzed by $Pd(PPh_3)_4$, ring closing metathesis catalyzed by Grubbs' catalyst (1st generation), hydrogenation catalyzed by Wilkinson's Catalyst, and Suzuki-Miyaura couplings catalyzed by $Pd(PPh_3)_4$ and $Pd_2(dba)_3$.

5.5 References

1 This body of work often refers to these materials as "zero valent" iron.

2 X. Q. Li, D. W. Elliott and W. X. Zhang, *Critical Reviews in Analytical Chemistry,* 2006, **31**, 111-122.

3 X. Q. Li and W. X. Zhang, *Langmuir,* 2006, **22**, 4638-4642.

4 X. Q. Li and W. X. Zhang, *Journal of Physical Chemistry C,* 2007, **111**, 6939-6946.

5 S. M. Ponder, J. G. Darab and T. E. Mallouk, *Environmental Science & Technology,* 2000, **34**, 2564-2569.

6 S. M. Ponder, J. G. Darab, J. Bucher, D. Caulder, I. Craig, L. Davis, N. Edelstein, W. Lukens, H. Nitsche, L. F. Rao, D. K. Shuh and T. E. Mallouk, *Chemistry of Materials,* 2001, **13**, 479-486.

7 J. E. Macdonald, J. A. Kelly and J. G. C. Veinot, *Langmuir,* 2007, **23**, 9543-9545.

8 H. S. Cao and W. X. Zhang, *Journal of Hazardous Materials,* 2006, **132**, 213-219.

9 J. G. Darab, A. B. Amonette, D. S. D. Burke, R. D. Orr, S. M. Ponder, B. Schrick, T. E. Mallouk, W. W. Lukens, D. L. Caulder and D. K. Shuh, *Chemistry of Materials,* 2007, **19**, 5703-5713.

10 P. B. Kettler, *Organic Process Research and Development,* 2003, **7**, 342-354.

11 K. McEleney, D. P. Allen, A. E. Holliday and C. M. Crudden, *Organic Letters,* 2006, **8**, 2663-2666.

12 S. H. Hong and R. H. Grubbs, *Organic Letters,* 2007, **9**, 1955-1957.

13 K. T. Nielsen, K. Bechgaard and F. C. Krebs, *Synthesis-Stuttgart,* 2006, 1639-1644.

14 Committee for Proprietary Medicinal Products Note for guidance on specific limits for residues of metal catalysts, **2002**. The European Agency for the Evaluation of Medicinal Products. www.emea.europa.eu/pdfs/human/swp/444600en.pdf (accessed January 25, 2008).

15 F. M. M. Morel, *Principals of Aquatic Chemistry*, John Wiley & Sons, Inc., New York, 1983, p. 446.

16 W. Yantasee, C. L. Warner, T. Sangvanich, R. S. Addleman, T. G. Carter, R. J. Wiacek, G. E. Fryxell, C. Timchalk and M. G. Warner, *Environmental Science & Technology,* 2007, **41**, 5114-5119.

17 C. M. Crudden, K. McEleney, S. L. MacQuarrie, A. Blanc, M. Sateesh and J. D. Webb, *Pure and Applied Chemistry,* 2007, **79**, 247-260.

18 A. B. M. Giasuddin, S. R. Kanel and H. Choi, *Environmental Science & Technology,* 2007, **41**, 2022-2027.

19 S. R. Kanel, B. Manning, L. Charlet and H. Choi, *Environmental Science & Technology,* 2005, **39**, 1291-1298.

20 K. Tyrovola, N. P. Nikolaidis, N. Veranis, N. Kallithrakas-Kontos and P. E. Koulouridakis, *Water Research,* 2006, **40**, 2375-2386.

21 R. Rangsivek and M. R. Jekel, *Water Research,* 2005, **39**, 4153-4163.

22 C. Amatore, A. Jutand and M. A. Mbarki, *Organometallics,* 1992, **11**, 3009-3013.

23 J. A. Schreifels, P. C. Maybury and W. E. Swartz, *Journal of Organic Chemistry,* 1981, **46**, 1263-1269.
24 A. J. Birch and K. A. M. Walker, *Journal of the Chemical Society C-Organic,* 1966, 1894-1896.
25 R. F. Heck and J. P. Nolley, *Journal of Organic Chemistry,* 1972, **37**, 2320-2322.
26 C. Amatore, A. Jutand, F. Khalil, M. A. Mbarki and L. Mottier, *Organometallics,* 1993, **12**, 3168-3178.
27 F. A. Cotton and F. Wilkinson, *Advanced Inorganic Chemistry*, Wiley, Toronto, 1988, pp. 871, 878, 942.
28 L. F. Kelly and G. J. Deeble, *Journal of Chemical Education,* 1986, **63**, 1107-1108.
29 P. E. Laibinis and G. M. Whitesides, *Journal of the American Chemical Society,* 1992, **114**, 9022-9028.
30 Y. P. Sun, X. Q. Li, J. S. Cao, W. X. Zhang and H. P. Wang, *Advances in Colloid and Interface Science,* 2006, **120**, 47-56.
31 Y. Abe, T. Hasegawa, M. Kawamura and K. Sasaki, *Vacuum,* 2004, **76**, 1-6.
32 M. Erdemoğlu and M. Sarikaya, *Journal of Colloid and Interface Science,* 2006, **300**, 795-804.
33 *CRC Handbook of Chemistry and Physics*, 70th edn., CRC Press, Inc., Boca Raton, 1989-1990, pp. D151-D158.
34 B. L. Maschhoff and N. R. Armstrong, *Langmuir,* 1991, **7**, 693-703.
35 A. P. Grosvenor, B. A. Kobe and N. S. McIntyre, *Surface and Interface Analysis,* 2004, **36**, 1637-1641.
36 J. H. Barkalow, J. Breting, B. J. Gaede, A. R. Haight, R. Henry, B. Kotecki, J. Mei, K. B. Pearl, J. S. Tedrow and S. K. Viswanath, *Organic Process Ressearch & Development,* 2007, **11**, 693-698.
37 C. E. Garrett and K. Prasad, *Advanced Synthesis & Catalysis,* 2004, **346**, 889-900.
38 R. G. Pearson, *Journal of the American Chemical Society,* 1963, **85**, 3533-3539.
39 M. Villa, V. Cannata, A. Rosi and P. Allegrini Process for the Removal of Heavy Metals. *U.S. Patent 6,239,301, B1,* 2001.
40 Y. P. Sun, X. Q. Li, W. X. Zhang and H. P. Wang, *Colloids and Surfaces A,* 2007, **308**, 60-66.
41 Q. Liu and Z. Xu, *Langmuir,* 1995, **11**, 4617-4622.
42 O. Margeat, F. Dumestre, C. Amiens, B. Chaudret, P. Lecante and M. Respaud, *Progress in Solid State Chemistry,* 2005, **33**, 71-79.
43 S. H. Hong, A. G. Wenzel, T. T. Salguero, M. W. Day and R. H. Grubbs, *Journal of the American Chemical Society,* 2007, **129**, 7961-7968.
44 S. E. Hazlet and C. A. Dornfeld, *Journal of the American Chemical Society,* 1944, **66**, 1781-1782.
45 Y. S. Keum and Q. X. Li, *Chemosphere,* 2004, **54**, 255-263.
46 J. Wielant, T. Hauffman, O. Blajiev, R. Hausbrand and H. Terryn, *Journal of Physical Chemistry C,* 2007, **111**, 13177-13184.
47 M. C. Militello and S. J. Simko, *Surface Science Spectra,* 1997, **3**, 395-401.
48 K. L. Cheng, J. C. Carver and T. A. Carlson, *Inorganic Chemistry,* 1973, **12**, 1702-1704.

49 P. E. Laibinis, G. M. Whitesides, D. L. Allara, Y. T. Tao, A. N. Parikh and R. G. Nuzzo, *Journal of the American Chemical Society,* 1991, **113**, 7152-7167.
50 M. Volmeruebing and M. Stratmann, *Applied Surface Science,* 1992, **55**, 19-35.
51 M. J. Jones, *Organic Chemistry*, W.W. Norton & Company, New York, 1997, p. 1346.

Chapter 6: Conclusions and Future Work

This thesis has covered several diverse areas of research united by the theme of synthesis and applications of iron containing nanoparticles. This chapter will present a summary of the conclusions and some recommended future work for each research area outlined herein. Finally, a broad perspective of how this research ties into the greater scientific field of nanoparticle research is presented.

6.1 Preparation of FeTi nanoparticles (Chapter 2)

6.1.1 Conclusions

Using the co-reduction technique, the preparation of FeTi nanoparticles was attempted. Solutions of iron(III) and titanium(IV) chlorides were reduced with alkali naphthalides and potassium triethylborohydride. An amorphous material was obtained that contained both iron and titanium with inconsistent stoichiometric ratios between samples. The thermal decomposition of $Fe(CO)_5$ in the presence of either preformed Ti clusters or $Cp_2Ti(CO)_2$ was also attempted. These reactions also did not give the desired FeTi product. Instead, crystalline magnetite/maghemite was identified in a matrix of (likely) amorphous titania.

In none of the syntheses attempted were separated FeTi particles observed. It is likely that the crystal structure mismatch between bcc iron and hcp titanium prevents one metal from growing epitaxially on the other thus hindering the formation of FeTi intermetallic and core-shell nanoparticles.

6.1.2 Future Work

Of the alloy particles reported in the literature so far, almost all have one constituent of the coinage or noble metals.[1] To our knowledge, there are no reported solution synthesis of alloys nanoparticles containing the early transition metals. The reason for this is unclear. The oxophilicity of early main group metals may make characterization difficult but it appears, at least in the current case, the very preparation of the alloy as nanoparticles is hampered. This is strange considering intermetallics between early and late transition metals tend to be some of the most stable known.[2, 3]

The question remains, is facile crystal structure matching truly necessary for alloy and intermetallic nanoparticle formation? To address this, the synthesis of nanoparticle alloys of the early transition metals should be attempted. A wide spanning, detailed and systematic exploration of which alloys can be easily formed and which do not, along with a detailed examination of their phase diagrams may illuminate determining factors. This will require the fearless publication of "failed" experiments. Perhaps the scientific community's reluctance to do so to date has hindered progress in this area.

For titanium alloys and intermetallics specifically, a first step may be to attempt the preparation of RuTi nanoparticles. The phase diagram of this system has key similarities to that of FeTi;[4] Ru and Ti metals have different crystal structures and there is a CsCl structured intermetallic of RuTi. Unlike iron, small amounts of Ru will induce the titanium to adopt the bcc structure *below 200 °C*.[5] For iron-titanium, this only happens at temperatures above 568 °C (see Figure 2-1).[4] Inducing structural changes at temperatures relevant to the solution chemist will make the RuTi system easier to study before returning to FeTi.

Should this prove successful, the preparation of ternary alloy particles of RuFeTi may prove to provide a back door route to the formation of FeTi nanoparticles.

6.2 Size control of iron and iron oxide nanoparticles (Chapter 3)

6.2.1 Conclusions

The solution decomposition of $Fe(CO)_5$ was studied in order to achieve particles smaller than the 4 nm particles already observed in the literature.[6, 7] The use of surfactants was found to inhibit growth and prevent nucleation of particles. Therefore, surfactant choice was not found to be an efficient way to achieve very small particles.

The presence of water was found to increase nucleation events by lowering the activation energy for decomposition through water-gas-shift chemistry. The average particle size was varied from 5.6 nm down to 2.2 nm by changing the initial water concentration in the solution.[8]

Introduction of $Fe(CO)_5$ directly into hot solvents and surfactant mixtures also saw particle below 4 nm, however safety became a concern in some reaction procedures and yields were small for others.

Decomposition of $Fe(CO)_5$ by sonication of solutions also showed promise for particles below 4 nm. To avoid surfactant lability and the sintering of particles, very short reaction times were required which also greatly reduced the yields.

Significant headway was made in determining and isolating the factors which control particle size.

6.2.1 Future Work

Many factors have been identified to influence particle size in the $Fe(CO)_5$ system both by our research group and others.[8-14] Isolation and control of these factors makes experimental reproducibility a major problem. It is likely variable water concentrations have been influencing the consistency of results in other laboratories. Water concentration should be controlled or monitored and reported in the future if batch-to-batch reproducibility is to be realized. The use of statistics to prove a trend is underemployed in our field and will prove a very useful tool for identifying trends between particle size and less obvious factors.

The best yields and smallest particles were achieved by the highest water concentrations in our solutions, which gave particles with an average diameter of 2.2 nm. The water concentration was limited by the solubility of water in the reaction mixture. The choice of a more hydrophilic solvent and optimization of surfactant concentrations may yield even smaller particles. This may give size control of iron particles of sizes below 2.2 nm.

6.3 The use of Iron oxide capped iron nanoparticles for the removal of catalytic metals (Chapters 4 and 5)

6.3.1 Conclusions

Iron oxide capped iron nanoparticles (Fe@Fe_xO_y) can be used to sequester trace catalytic metals from reaction products in aqueous and polar organic solvents.[15, 16] In cases where there are no strongly coordinating ligands present, the mechanism of remediation is two fold. Metal ions are coordinated to surface hydroxyl groups of the iron oxide particle surfaces and can also be reduced to the zero oxidation state by the iron metal core.[15, 16] Since part of the sequestration depends on reduction, there is a trend between electrochemical potential of the metal being sequestered and the remediation capacity; metal ions with much higher electrochemical potentials than that of iron are sequestered more effectively.[16]

The presence of coordinating phosphines hinders straightforward sequestration of catalytic metals by Fe@Fe_xO_y. Sequestration can be efficient when it is performed in the presence of 3-mercaptopropionic acid. Spectroscopic analysis indicates the carboxylic acid group bonds to the iron surface and the thiol group competitively bonds to the catalytic metals. Under these situations, sequestration is dominated by the adsorption mechanism rather than the reduction.[16]

These techniques were successfully applied to a hydrogenation over Raney nickel,[16] a copper catalyzed "click" reaction,[15] Heck couplings,[15, 16] a Suzuki-Miyaura coupling, hydrogenation over Wilkinson's catalyst and a ring closing metathesis by Grubbs' Catalyst.[16]

6.3.2 Future Work

Chapters 4 and 5 only scrape the surface of the potential for this technique. The use of additives other than 3-mercaptopropionic acid may provide enhanced sequestration. For example, dimercaptosuccinic acid has two carboxylic acid groups and two thiol groups and is already FDA-approved for heavy metal poisoning.[17] Also, the addition of an aliphatic chain to the additive may allow for sequestration in non-polar solvents.

In all, the next step for this technique is application-based development. Each known sequestration technique and material has advantages and disadvantages which are weighted for each individual trace metal problem.[18, 19] Further development of this technique will be most effective by targeted development to a specific industrial reaction, substrate, solvent, etc.

Examining the situation in another light, very inexpensive and magnetic particles have been capped with small amounts of expensive catalytic metals. These provide interesting catalytic materials in and of themselves with the potential of very facile catalyst recycling due to the magnetic properties of the iron. What chemical transformations can be performed? Is the reactivity different than the same catalytic metals on other supports? Can we add two different materials to the surface? How does this change the reactivity? Does the presence of the iron core change the reactivity? These questions are currently under examination in our laboratory.

6.4 Answering questions and discovering more questions

Studies were performed examining three fundamental questions posed in the introduction that nag and drive the nanoparticle chemist. These questions apply generally to nanoparticles and are being answered by the broader community. We have responded to these questions in the context of iron containing nanoparticle systems.

1) Can we control the composition of these particles?

In Chapter 2 possible syntheses for FeTi nanoparticles were examined, which were ultimately unsuccessful. Indeed the formation of alloy nanoparticles is not straightforward and requires much more extensive study to achieve desired compositions.

In Chapters 4 and 5, Fe@Fe_xO_y were used to remove catalytic metals from solutions. Although not a direct goal, the surface of these particles were covered with a wide variety of different metals and are now providing possibilities as catalytic materials.

2) What controls the size of particles?

In Chapter 3, a detailed exploration of one nanoparticle forming system was discussed: the decomposition of $Fe(CO)_5$ in solvent/surfactant systems. It was found that the counter-productive balance of nucleation and growth inhibition as controlled by surfactants dictated particle sizes. It was also discovered that trace water in the reactions decreased particle size by promoting the decomposition of $Fe(CO)_5$. Nanoparticles as small as 2.2 nm were achieved and are some of the smallest in the literature. The different factors determining particle size have not been identified, and size control below 2.2 nm remains a brass ring for which we can reach.

3) How can the chemical properties of the materials be exploited?

Chapter 4 and 5 focused on the use of iron oxide capped nanoparticles to remove trace catalytic metal impurities from reaction products. This technique is ready for further development for a specific industrial problem.

By no means are our answers to these broad questions complete – even for iron specifically. Some of our responses have wide-ranging applicability and others have provided surprises and exceptions. Like most science, this exploratory research into iron containing nanoparticles has birthed more questions, providing a challenge and a call to battle for further experimentation. Iron containing nanoparticles are intriguing materials to study and very promising for some areas of application. Their future development will be worth following.

6.5 References

1 R. Ferrando, J. Jellinek and R. L. Johnston, *Chemical Reviews*, 2008, **108**, 845-910.

2 G. N. Kamm, *Physical Review B*, 1975, **12**, 3013-3022.

3 Mar, A. personal communication, 2008.

4 H. Okamoto, *Journal of Phase Equilibria*, 1996, **17**, 369-369.

5 N. G. Boriskina and Kornilov, II, *Russian Metallurgy*, 1976, 162-165.

6 T. Hyeon, *Chemical Communications*, 2003, 927-934.

7 D. L. Huber, *Small*, 2005, **1**, 482-501.

8 J. E. Macdonald, C. J. Brooks and J. G. C. Veinot, *Chemical Communications*, 2008, 3777 - 3779.

9 M. V. Kovalenko, M. I. Bodnarchuk, R. T. Lechner, G. Hesser, F. Schaffler and W. Heiss, *Journal of the American Chemical Society*, 2007, **129**, 6352-6353.

10 X. W. Teng and H. Yang, *Journal of Materials Chemistry*, 2004, **14**, 774-779.

11 T. W. Smith and D. Wychick, *Journal of Physical Chemistry*, 1980, **84**, 1621-1629.

12 M. F. Casula, Y. W. Jun, D. J. Zaziski, E. M. Chan, A. Corrias and A. P. Alivisatos, *Journal of the American Chemical Society*, 2006, **128**, 1675-1682.

13 A. Cabot, V. F. Puntes, E. Shevchenko, Y. Yin, L. Balcells, M. A. Marcus, S. M. Hughes and A. P. Alivisatos, *Journal of the American Chemical Society*, 2007, **129**, 10358-10360.

14 T. Hyeon, S. S. Lee, J. Park, Y. Chung and H. Bin Na, *Journal of the American Chemical Society*, 2001, **123**, 12798-12801.

15 J. E. Macdonald, J. A. Kelly and J. G. C. Veinot, *Langmuir*, 2007, **23**, 9543-9545.

16 J. E. Macdonald and J. G. C. Veinot, *Langmuir*, 2008, **24**, 7169-7177.

17 W. Yantasee, C. L. Warner, T. Sangvanich, R. S. Addleman, T. G. Carter, R. J. Wiacek, G. E. Fryxell, C. Timchalk and M. G. Warner, *Environmental Science & Technology*, 2007, **41**, 5114-5119.

18 A. Thayer, *Chemical and Engineering News*, 2005, **83**, 55-58.

19 C. E. Garrett and K. Prasad, *Advanced Synthesis & Catalysis*, 2004, **346**, 889-900.

Appendix A: EDS spectra (Sections 2.3.2-5)

Figure App. A-1: Example EDS spectrum of a reduction of iron(III) and titanium(IV) chlorides*

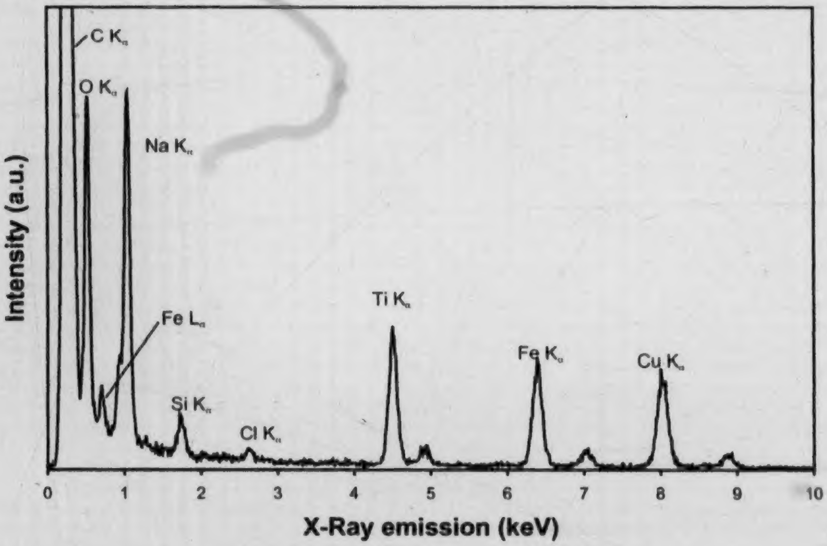

* Si is background from the drifted silicon detector, Cu from the copper TEM grid. The strong C peak is partially a result of the carbon coated TEM grid

Figure App. A-2: Example EDS spectrum of a reduction of iron(III) and titanium(IV) chlorides

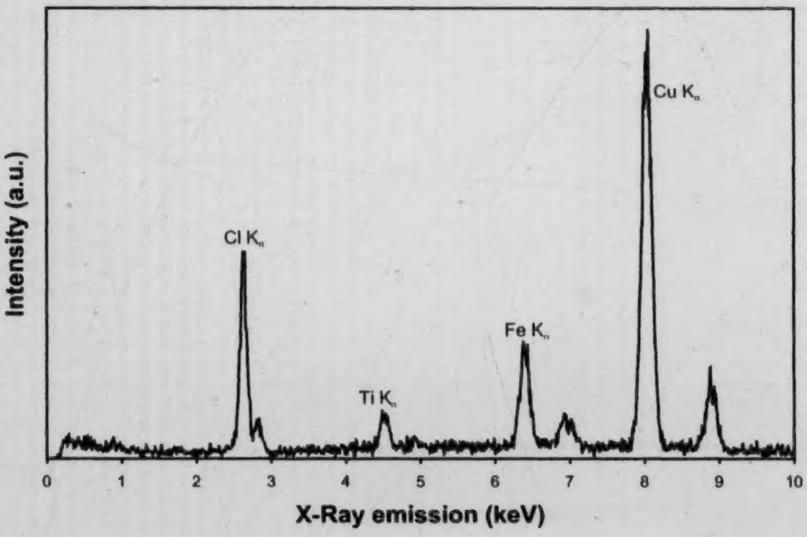

Figure App. A-3: EDS spectrum of particles resultant from the high temperature reduction of iron(III) and titanium(IV) chlorides

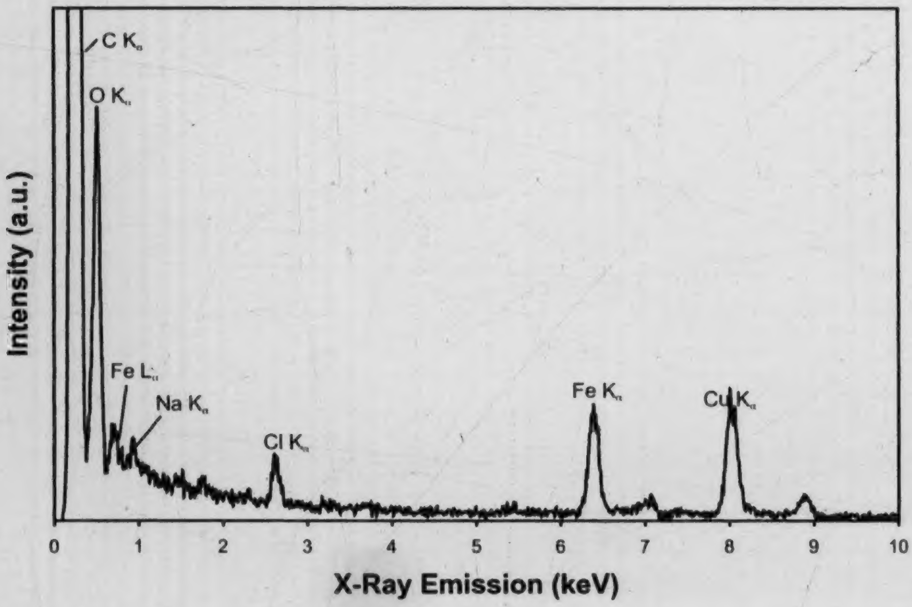

Figure App. A-4: EDS spectrum of amorphous material from the thermal decomposition of $Fe(CO)_5$ and $Cp_2Ti(CO)_2$

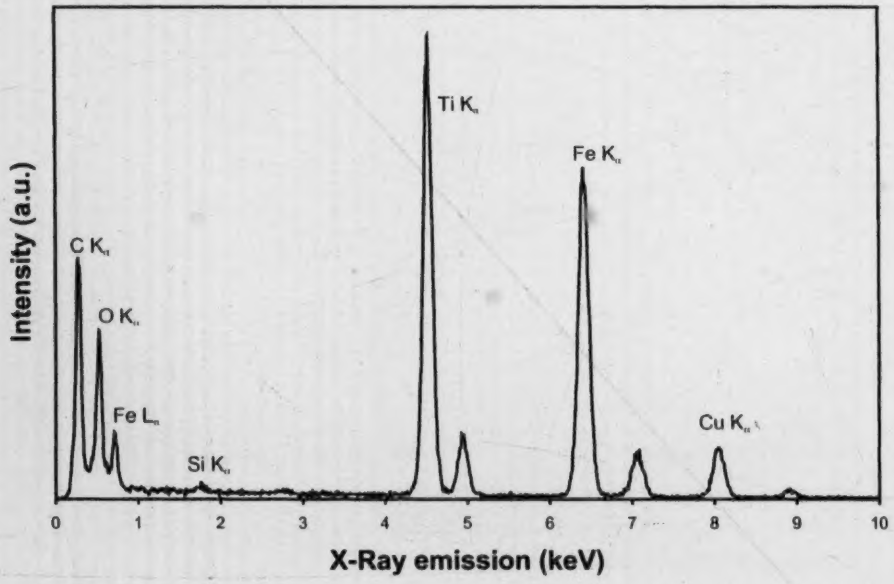

Figure App. A-5: EDS spectrum of cube-like structures resultant from the thermal decomposition of $Fe(CO)_5$ and $Cp_2Ti(CO)_2$

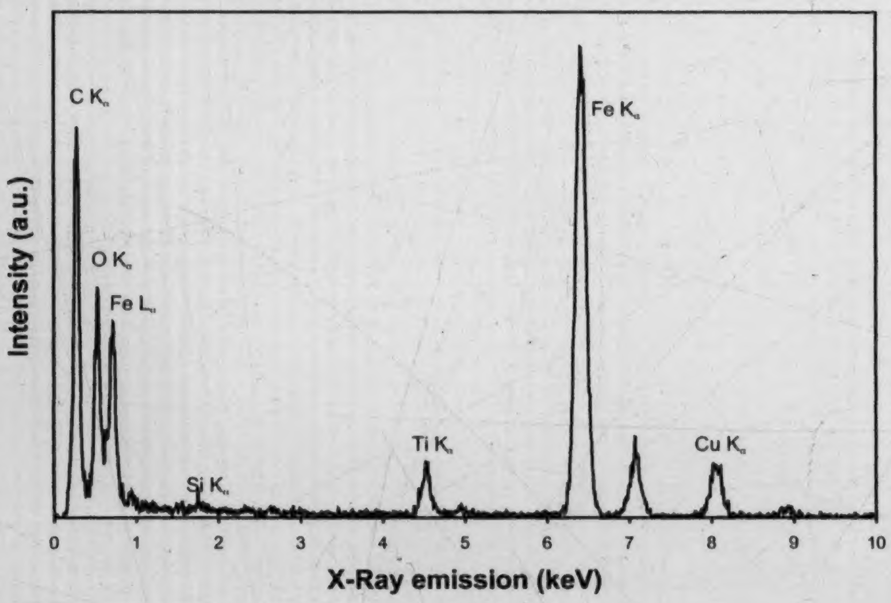

Figure App. A-6: EDS spectrum of material resultant from the decomposition of $Fe(CO)_5$ in the presence of Ti clusters (formed *in situ*)

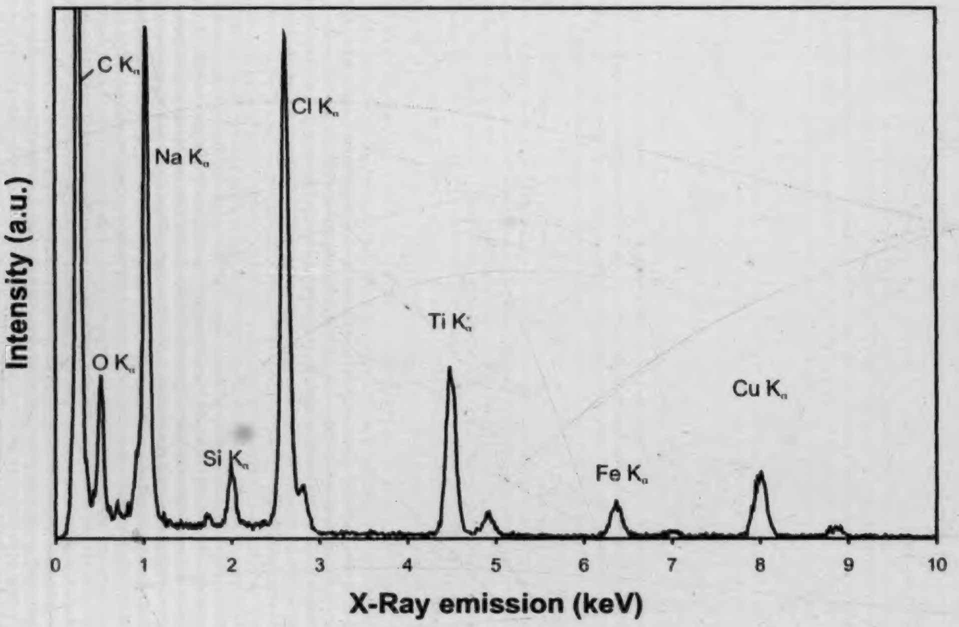

Appendix B: Additional statistical details

Size distributions (section) 3.3.1

Size distribution of oleic acid capped particles

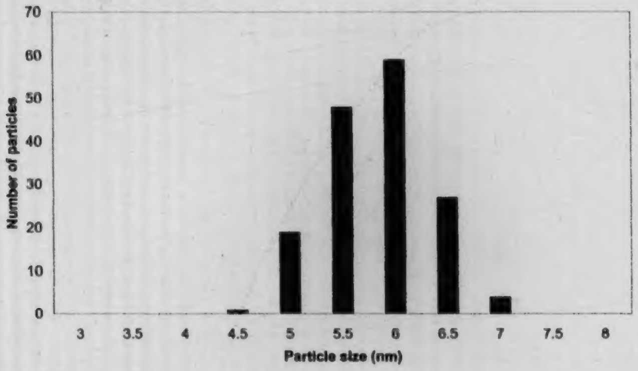

Size distribution of oleyl amine capped particles

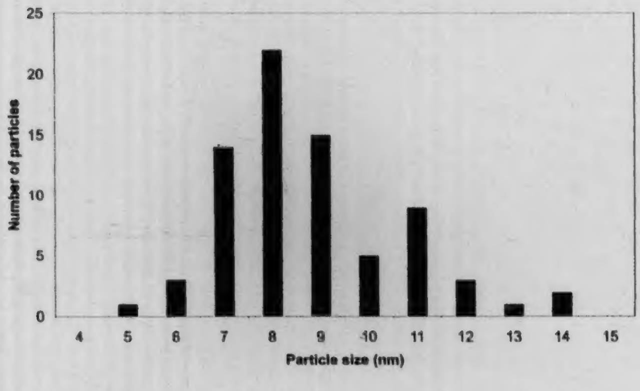

Size distributions of TOPO capped particles

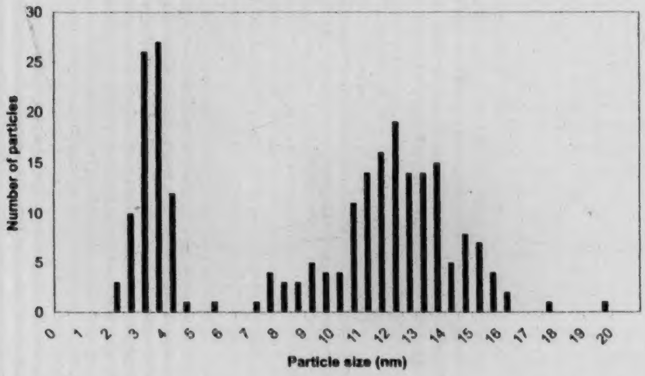

Statistical analysis for the promotion of decomposition by water (Section 3.3.3)

The Count of the number of particles measured, their Average diameter and their Standard Deviations are reported for each sample. ANOVA (single factor) was conducted on sets of samples at the same concentration giving an F value. F-critical is the value above which the null hypothesis (that the data sets are from the same probability distribution) is rejected at α =0.05.

Table App. B-1: Statistical analysis of particle diameter.

$[H_2O]$ (ppm)		Count	Average (nm)	St. Dev. (nm)	F	F-critical
101	A	158	5.58	0.50	23.9	2.6
	B	147	5.52	0.44		
	C	85	5.06	0.46		
	D	120	5.59	0.59		
181	A	141	4.68	0.65	6.2	2.6
	B	133	4.67	0.59		
	C	112	4.92	0.56		
	D	126	4.84	0.40		
234	A	134	3.11	0.51	490.2	3.9
	B	134	4.54	0.55		
479	A	181	4.23	0.59	449.7	3.9
	B	145	3.01	0.42		
657	A	96	2.54	0.49	276.0	3.0
	B	133	2.42	0.39		
	C	154	3.53	0.43		
1073	A	150	3.47	0.45	242.1	3.9
	B	198	2.80	0.36		
1590	A	134	2.47	0.40	30.8	3.9
	B	128	2.20	0.38		

ANOVA was then performed between groups and a Tukey Post Test to examine the statistical differences between pairs of groups. Prism 5.0 software was employed.

Table App. B-2: Analysis between concentration groups

One Way ANOVA between groups

P value	< 0.0001
Are means signif. different (*i.e.*, P < 0.05)?	Yes

Tukey's Multiple Comparison Test

Water concentration (ppm) groups	Mean Difference	Significant? *i.e.*, P < 0.05?
101 vs 181	0.66	No
101 vs 234	1.613	Yes
101 vs 479	1.818	Yes
101 vs 657	2.608	Yes
101 vs 1073	2.303	Yes
101 vs 1590	3.103	Yes
181 vs 234	0.9525	No
181 vs 479	1.158	No
181 vs 657	1.948	Yes
181 vs 1073	1.643	Yes
181 vs 1590	2.443	Yes
234 vs 479	0.205	No
234 vs 657	0.995	No
234 vs 1073	0.69	No
234 vs 1590	1.49	No
479 vs 657	0.79	No
479 vs 1073	0.485	No
479 vs 1590	1.285	No
657 vs 1073	-0.305	No
657 vs 1590	0.495	No
1073 vs 1590	0.8	No

Appendix C: XPS of Fe@ Fe_xO_y after Sequestration (Section 4.3.1)

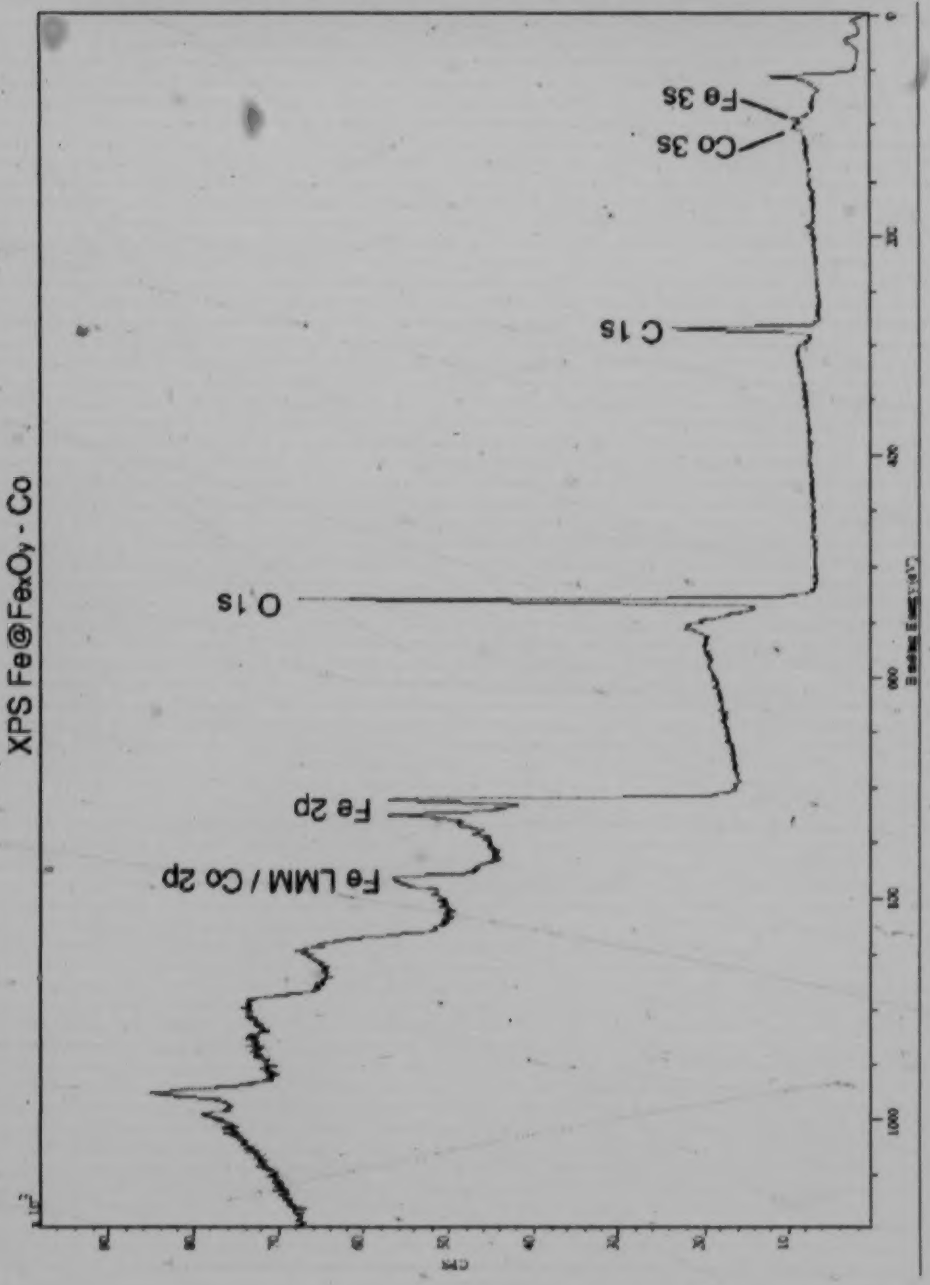

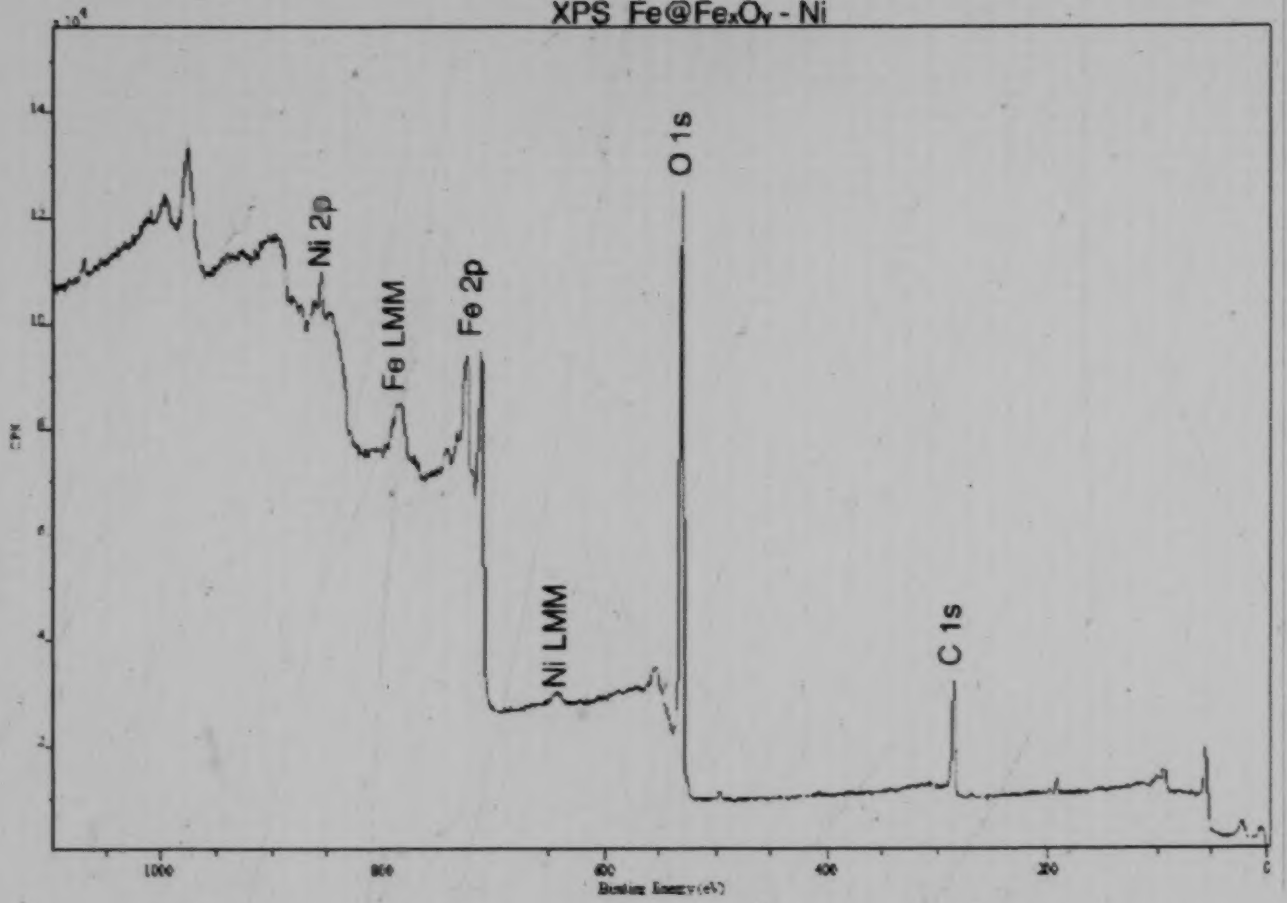
XPS Fe@FexOy - Ni
x10^4
14
12
10
8
6
4
2
CPS
Ni 2p
Fe LMM
Fe 2p
Ni LMM
O 1s
C 1s
1000
800
600
400
200
0
Binding Energy(eV)

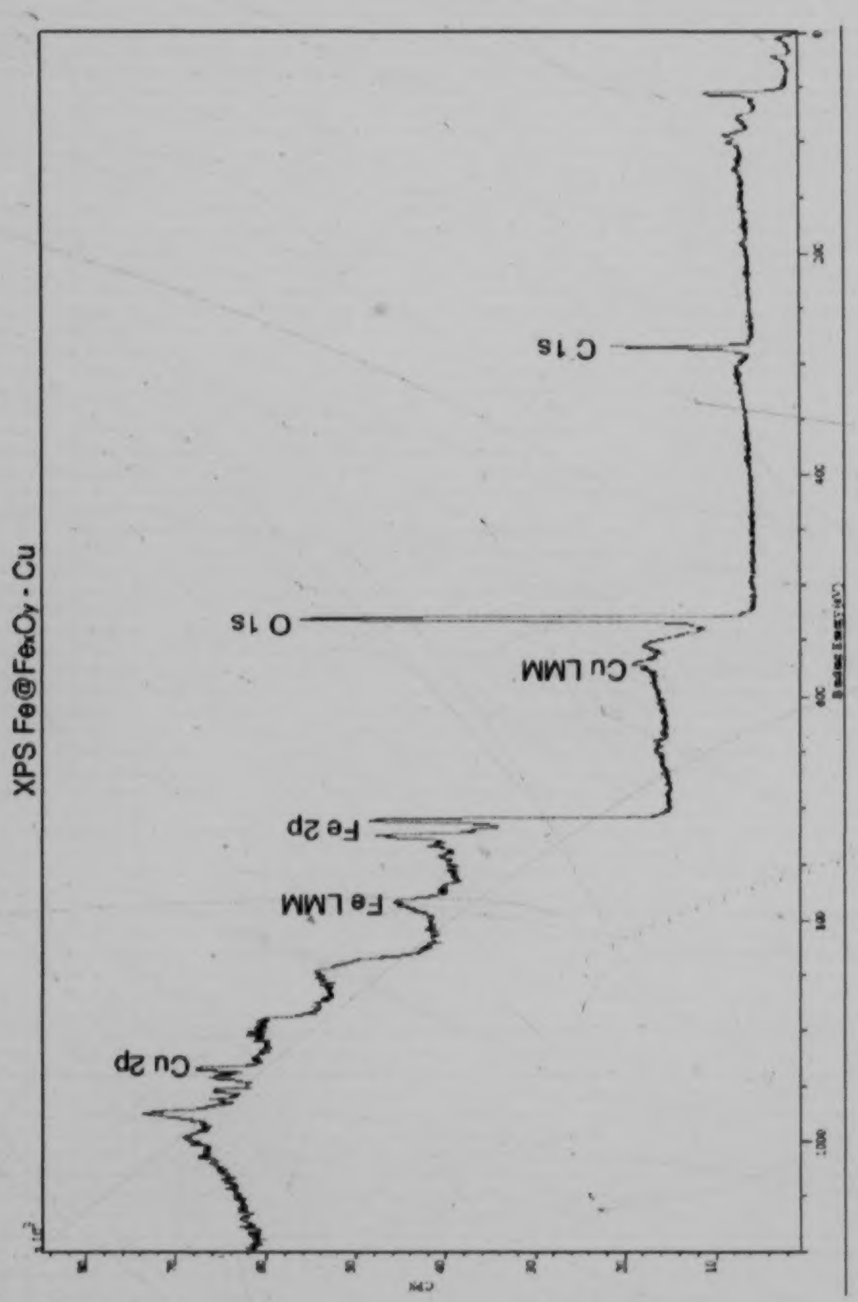
XPS Fe@Fe$_x$O$_y$ - Cu

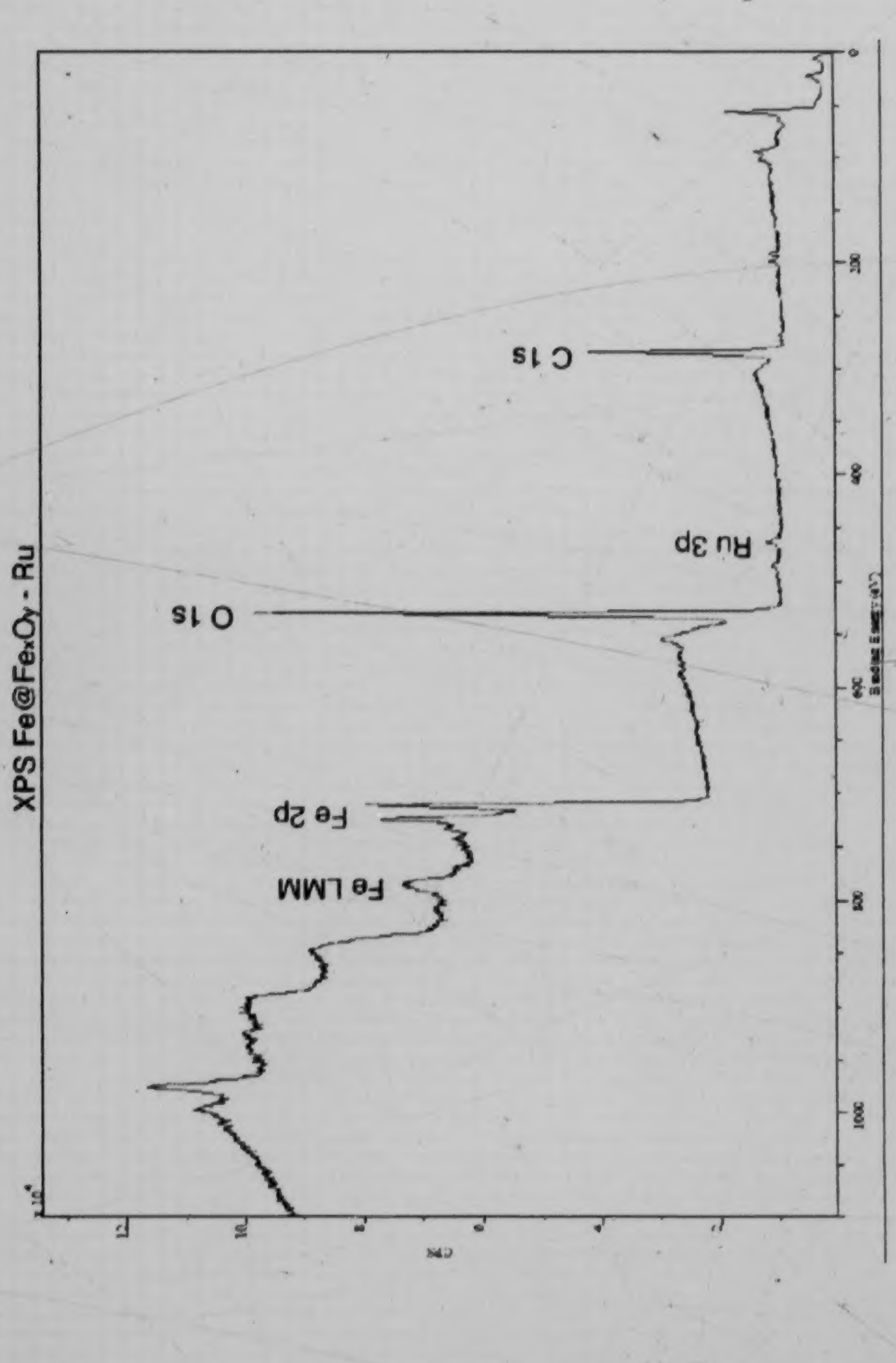
XPS Fe@FexOy - Ru
C 1s
Ru 3p
O 1s
Fe 2p
Fe LMM
x 10^4
12
10
8
6
4
2
CPS
0
200
400
600
800
1000
Binding Energy (eV)

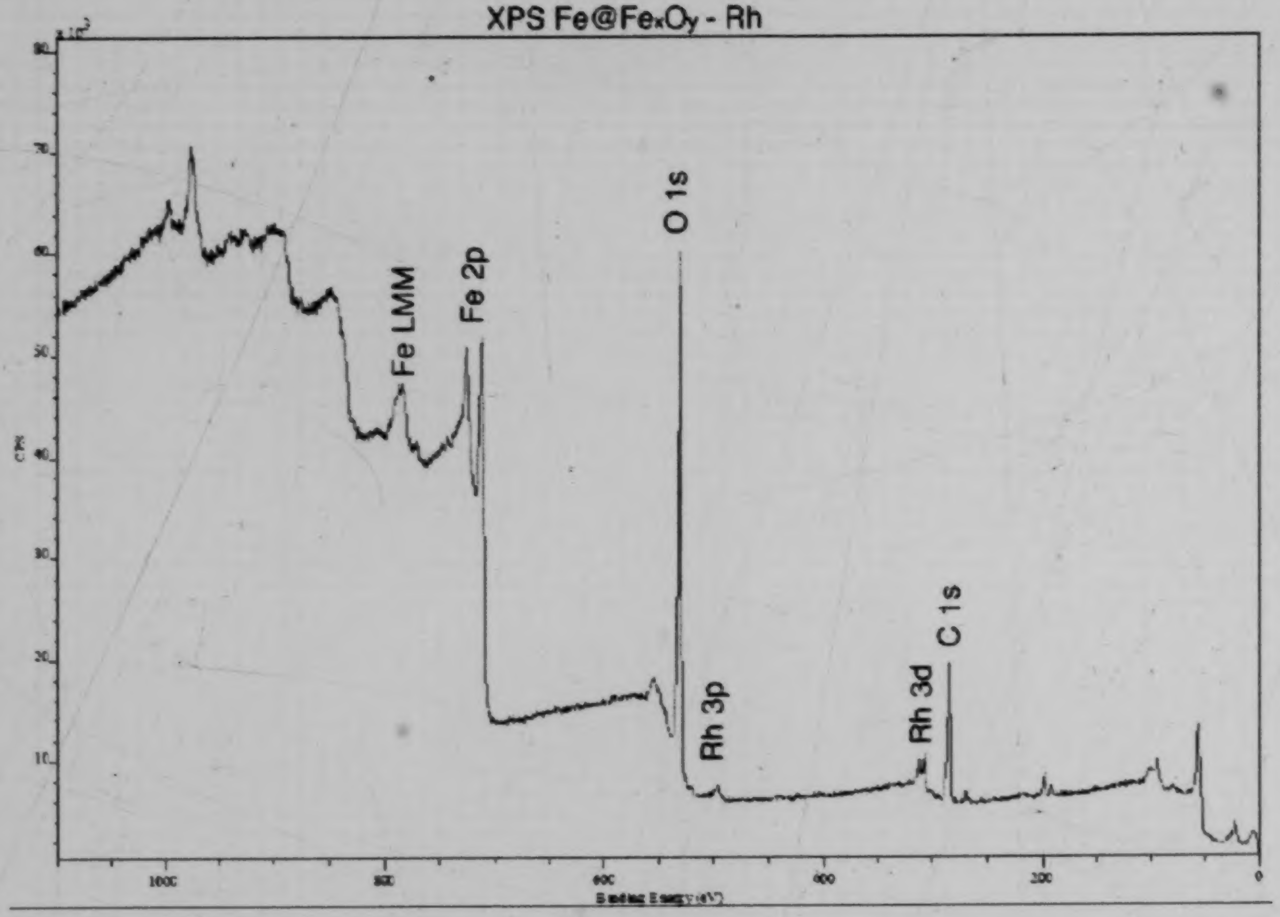
XPS Fe@FexOy - Rh

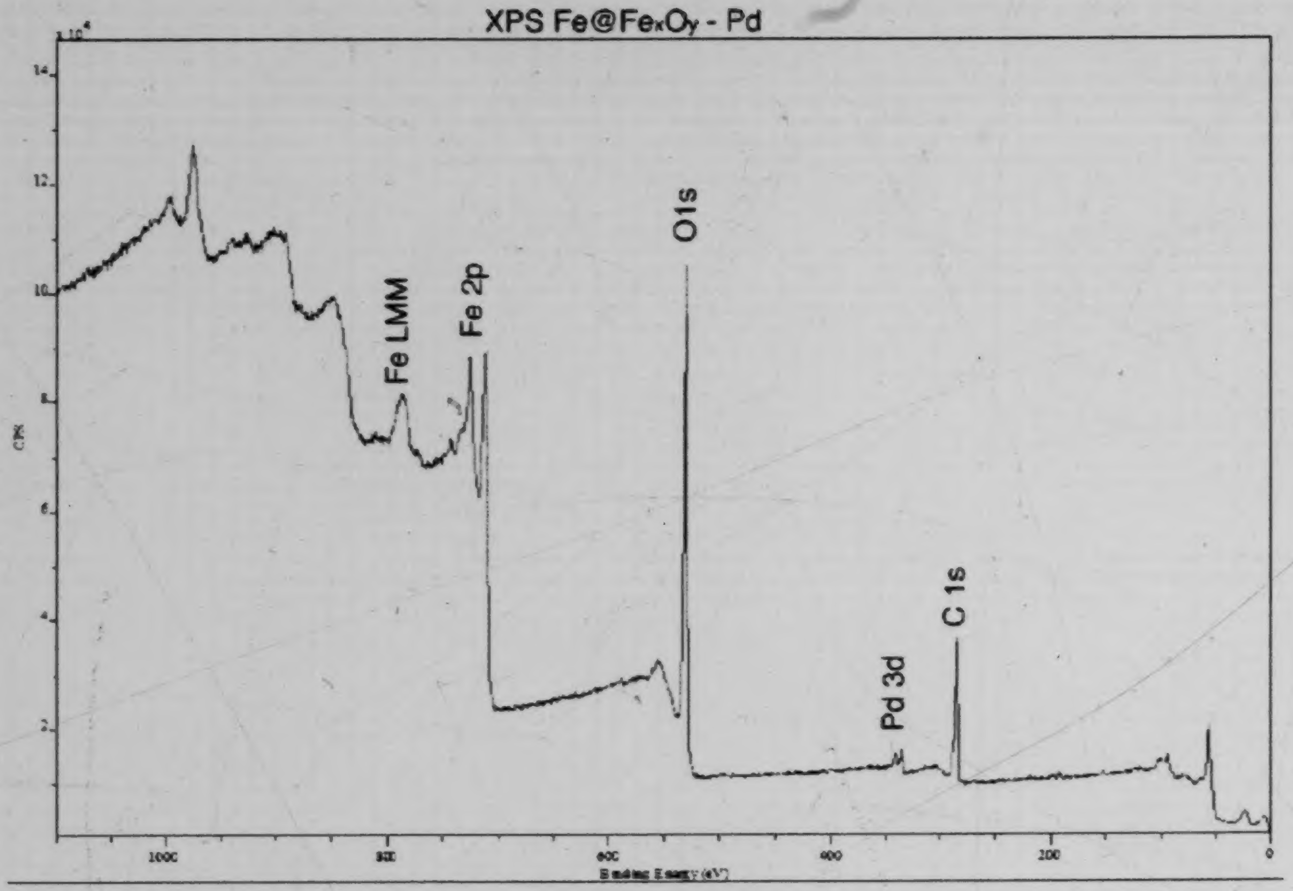
XPS Fe@FexOy - Pd
x 10^4
14
12
10
8
6
4
2
CPS
Fe LMM
Fe 2p
O1s
Pd 3d
C 1s
1000
800
600
400
200
0
Binding Energy (eV)

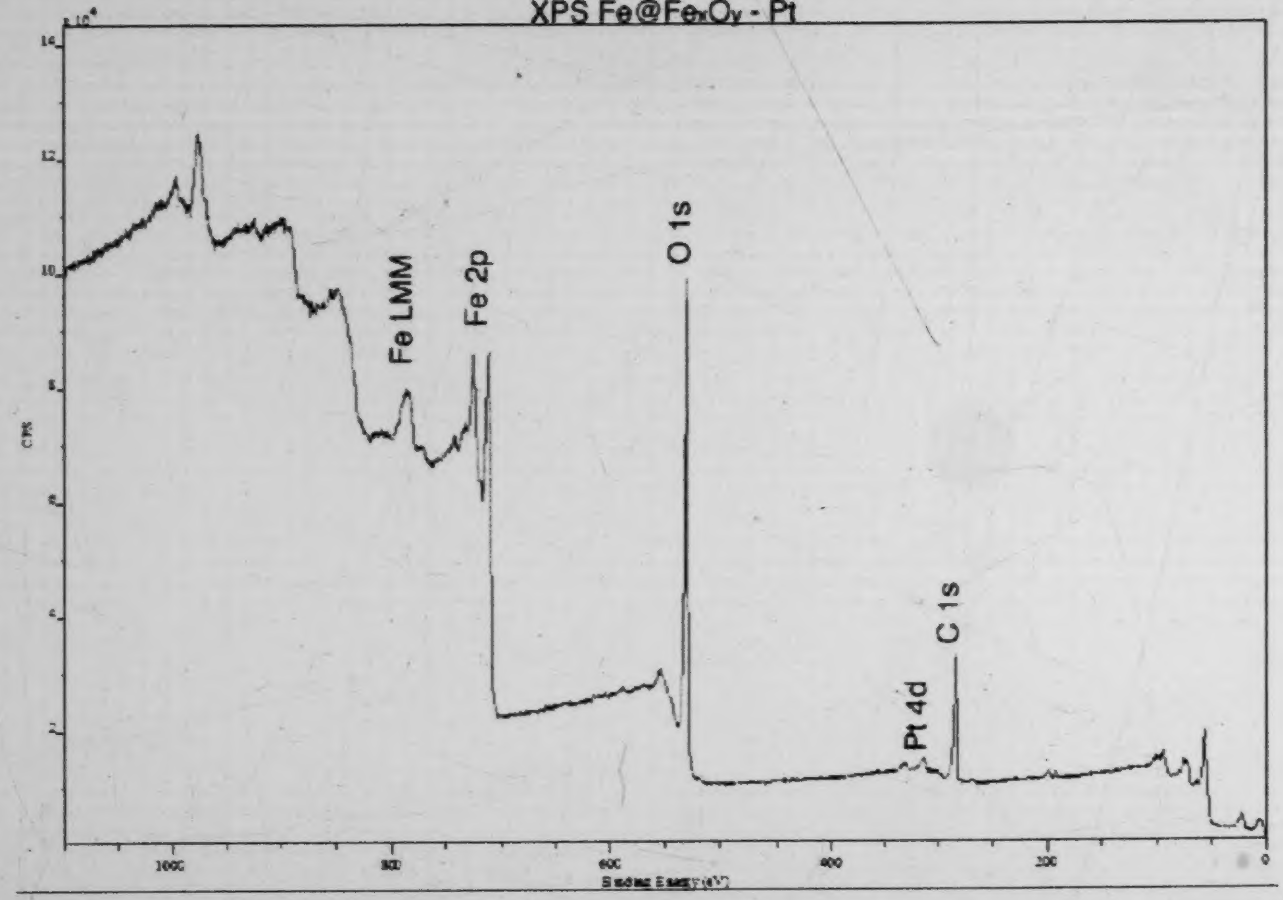
XPS Fe@Fe$_x$O$_y$ - Pt
x 10^4
CPS
14
12
10
8
6
4
2
Fe LMM
Fe 2p
O 1s
Pt 4d
C 1s
1000
800
600
400
200
0
Binding Energy (eV)

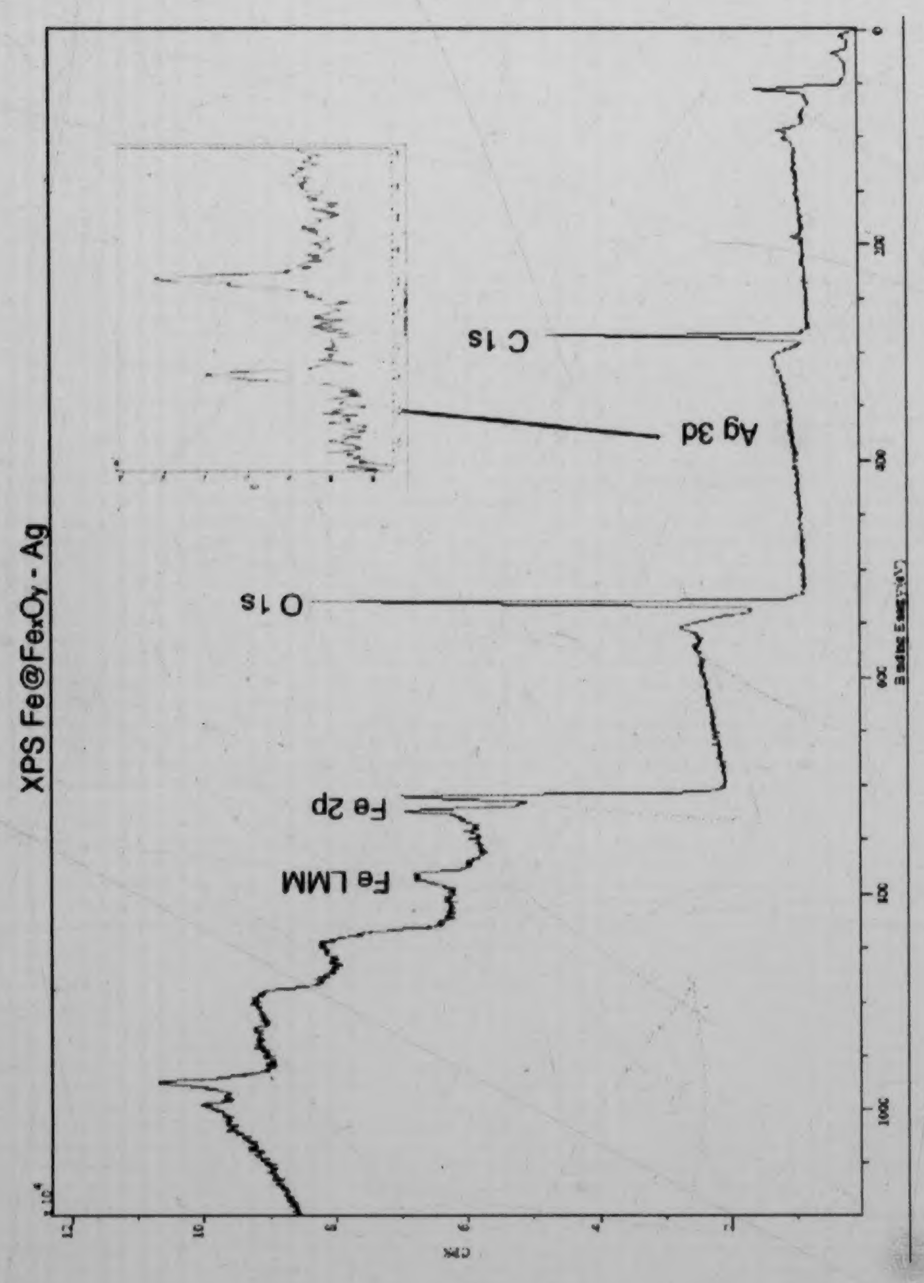
XPS Fe@FexOy - Ag
Fe LMM
Fe 2p
O 1s
Ag 3d
C 1s
Binding Energy (eV)
c/s
$\times 10^4$
12
10
8
6
4
2
1000
800
600
400
200
0

Appendix D: Small molecule additive screening experiments for metal sequestration using Fe@Fe$_x$O$_y$ (Sections 5.2.4 and 5.3.4)

Legend

ASP	Aspartic acid
CYS	Cystiene
CYA	Cysteamine
GLY	Glysine
LYS	Lysine
MEA	3-mercaptopropionic acid
TUA	Trithiocyanuric acid

Table App. D-1: Qualitative tests into the sequestration of phosphine inhibited metals by Fe@Fe$_x$O$_y$

	Ligand or small molecule additive	Aqueous KOH (0.2 mM)	Metal source in THF	~[M] (ppm)	Intial solution colour	Sequestration Material	reaction conditions under static argon	soultion colour after sequestration
Qualitative tests into the role of phosphines and phosphine oxides								
A	$(Bu)_3PO$, 2 eq	0.25 mL	$Pd(OAc)_2$ (5.0 mL)	180	yellow	Fe@Fe$_x$O$_y$, 10 mg	18h	clear colourless
B	$(Bu)_3PO$, 2 eq	0.25 mL		180	colourless	Fe@Fe$_x$O$_y$, 10 mg	18h	clear colourless
C	$(Bu)_3PO$, 2 eq	0.25 mL	$Pd(OAc)_2$ (5.0 mL)	180	yellow		18h	yellow
D	PPh_3, 3 eq	0.25 mL	$Pd(OAc)_2$ (5.0 mL)	180	dark brown	Fe@Fe$_x$O$_y$, 10 mg	18h	dark brown
E	PPh_3, 3 eq	0.25 mL		180	colourless	Fe@Fe$_x$O$_y$, 10 mg	18h	clear colourless
F	PPh_3, 1.5 eq	0.25 mL	$Pd(OAc)_2$ (5.0 mL)	180	yellow		18h	yellow
G	$(Bu)_3PO$, 3 eq	0.25 mL	$Pd(OAc)_2$ (5.0 mL)	180	yellow	Fe@Fe$_x$O$_y$, 10 mg	heated 50 C, 3 min	clear colourless
H	$(Bu)_3P$, 20 eq		$Pd(OAc)_2$ (5.0 mL)	180	yellow	Fe@Fe$_x$O$_y$, 10 mg	heated 60 C, 30 min	yellow
I	$(Bu)_3P$, 20 eq	0.25 mL	$Pd(OAc)_2$ (5.0 mL)	180	yellow	Fe@Fe$_x$O$_y$, 10 mg	heated 60 C, 30 min	orange
J	$(Bu)_3P$, 20 eq	0.25 mL	$Pd(OAc)_2$ (5.0 mL)	180	yellow	Fe@Fe$_x$O$_y$, 10 mg	heated 60 C, 30 min	orange
Qualitative tests with amino acid additives								
A	GLY, 0.08 mmol	0.5 mL	$Ru(PCy_3)_2Cl_2C_7H_6$ (3mL)	80	peach	Fe@Fe$_x$O$_y$, 10 mg	sonnocated, 2 min	yellow
B	LYS, 0.07 mmol	0.5 mL	$Ru(PCy_3)_2Cl_2C_7H_6$ (3mL)	80	green	Fe@Fe$_x$O$_y$, 10 mg	sonnocated, 2 min	yellow
C	CYS, 0.07 mmo	0.5 mL	$Ru(PCy_3)_2Cl_2C_7H_6$ (3mL)	80	purple	Fe@Fe$_x$O$_y$, 10 mg	sonnocated, 2 min	colourless
D	ASP, 0.06 mmol	0.5 mL	$Ru(PCy_3)_2Cl_2C_7H_6$ (3mL)	80	pink	Fe@Fe$_x$O$_y$, 10 mg	sonnocated, 2 min	faint yellow
E		0.5 mL	$Ru(PCy_3)_2Cl_2C_7H_6$ (3mL)	80	yellow-brown	Fe@Fe$_x$O$_y$, 10 mg	sonnocated, 2 min	yellow-brown
F		0.5 mL	$Ru(PCy_3)_2Cl_2C_7H_6$ (3mL)	80	yellow		sonnocated, 2 min	yellow-brown
G	CYS, 0.07 mmol	0.5 mL	$Ru(PCy_3)_2Cl_2C_7H_6$ (3mL)	80	purple		sonnocated, 2 min	purple

Table App. D-2: The effect of amino acids and trithiocyanuric acid (TUA) on sequestration

	Small molecule additive	Aqueous KOH (0.2 mM)	Metal source in 5.0 mL THF	Initial Solution Colour	$Fe@Fe_2O_3$	Final solution Colour	Initial [M] (ppm)	Final [M] (ppm)	% Removed	Final [Fe] (ppm)
A	GLY, 20 mmol	0.5 mL	$Ru(PCy_3)_2Cl_2C_7H_6$	yellow	20 mg	pink-orange	75.2	48.3	35.8	7.21
B	LYS, 20 mmol	0.5 mL	$Ru(PCy_3)_2Cl_2C_7H_6$	yellow	20 mg	yellow	75.2	50.0	33.5	27.7
C	ASP, 20 mmol	0.5 mL	$Ru(PCy_3)_2Cl_2C_7H_6$		20 mg	pink-orange	75.2	50.6	32.7	8.74
D	CYS, 20 mmol	0.5 mL	$Ru(PCy_3)_2Cl_2C_7H_6$	purple	20 mg	pink-orange	75.2	44.4	41.0	4.85
E	TUA, 20 mmol	0.5 mL	$Ru(PCy_3)_2Cl_2C_7H_6$	yellow	20 mg	pink-orange	75.2	13.7	81.8	11.5
F		0.5 mL	$Ru(PCy_3)_2Cl_2C_7H_6$	purple	20 mg	yellow	75.2	48.0	36.2	5.98
G	GLY, 20 mmol	0.5 mL	$Ru(PCy_3)_2Cl_2C_7H_6$	peach	20 mg	green	63.8	34.5	45.9	4.79
H	LYS, 20 mmol	0.5 mL	$Ru(PCy_3)_2Cl_2C_7H_6$	green	20 mg	orange	63.8	38.3	40.0	3.81
I	ASP, 20 mmol	0.5 mL	$Ru(PCy_3)_2Cl_2C_7H_6$	pink	20 mg	green	63.8	46.9	26.5	7.33
J	CYS, 20 mmol	0.5 mL	$Ru(PCy_3)_2Cl_2C_7H_6$	purple	20 mg	orange	63.8	22.8	64.3	16.3
K	TUA, 20 mmol	0.5 mL	$Ru(PCy_3)_2Cl_2C_7H_6$	red	20 mg	orange	63.8	52.6	17.6	76.8
L		0.5 mL	$Ru(PCy_3)_2Cl_2C_7H_6$	peach	20 mg	yellow	63.8	41.3	35.3	3.81
M	GLY, 20 mmol	0.5 mL	$Rh(PPh_3)_3Cl$	yellow-orange cloudy	20 mg	yellow	85.8	39.5	54.0	3.64
N	LYS, 20 mmol	0.5 mL	$Rh(PPh_3)_3Cl$	yellow-orange	20 mg	yellow	85.8	39.1	54.4	14.3
O	ASP, 20 mmol	0.5 mL	$Rh(PPh_3)_3Cl$	yellow-orange cloudy	20 mg	yellow	85.8	58.9	31.4	7.05
P	CYS, 20 mmol	0.5 mL	$Rh(PPh_3)_3Cl$	yellow-orange cloudy	20 mg	yellow	85.8	8.12	90.5	5.08
Q	TUA, 20 mmol	0.5 mL	$Rh(PPh_3)_3Cl$	yellow-orange	20 mg	orange	85.8	53.6	37.5	13.3
R		0.5 mL	$Rh(PPh_3)_3Cl$	yellow-orange	20 mg	orange	85.8	49.1	42.8	4.25
S	GLY, 20 mmol	0.5 mL	$Pd(PPh_3)_4$	faint yellow	20 mg	orange	125.5	86.9	30.8	3.88
T	LYS, 20 mmol	0.5 mL	$Pd(PPh_3)_4$	faint yellow	20 mg	yellow	125.5	23.8	81.0	2.66
U	ASP, 20 mmol	0.5 mL	$Pd(PPh_3)_4$	faint yellow	20 mg	brown	125.5	104	17.1	2.53
V	CYS, 20 mmol	0.5 mL	$Pd(PPh_3)_4$	orange, cloudy	20 mg	clear colourless	125.5	0.515	99.6	3.26
W	TUA, 20 mmol	0.5 mL	$Pd(PPh_3)_4$	yellow	20 mg	yellow	125.5	74.9	40.3	3.81
X		0.5 mL	$Pd(PPh_3)_4$	orange-yellow	20 mg	brown	125.5	118	6.0	2.56
Y	GLY, 20 mmol	0.5 mL	$Pd(OAc)_2$, PPh_3, 2.6 eq	brown solut. tan ppt.brown	20 mg		133.5	62.8	53.0	6.17
Z	LYS, 20 mmol	0.5 mL	$Pd(OAc)_2$, PPh_3, 2.6 eq	brown solut. Brown ppt	20 mg		133.5	56.5	57.7	2.86
AA	ASP, 20 mmol	0.5 mL	$Pd(OAc)_2$, PPh_3, 2.6 eq	yellow solut. Brown ppt.	20 mg		133.5	77.5	41.9	7.30
AB	CYS, 20 mmol	0.5 mL	$Pd(OAc)_2$, PPh_3, 2.6 eq	yellow solut. Brown ppt.	20 mg		133.5	5.13	96.2	7.52
AC	TUA, 20 mmol	0.5 mL	$Pd(OAc)_2$, PPh_3, 2.6 eq	dark orange solut.	20 mg		133.5	35.6	73.3	32.4
AD		0.5 mL	$Pd(OAc)_2$, PPh_3, 2.6 eq	dark orange solut.	20 mg		133.5	22.1	83.4	2.53

Table App. D-3: A closer look at the additive cysteine and the roles of functional groups

	Small molecule additive	Aqueous KOH (0.2 mM)	Metal source in 5.0 mL THF	Initial Solution Colour	Fe@Fe$_x$O$_y$	Final solution Colour	Initial [M] (ppm)	Final [M] (ppm)	% Removed	Final [Fe] (ppm)
A	CYS, 10 mmol	0.5 mL	Ru(PCy$_3$)$_2$Cl$_2$C$_7$H$_6$	purple	20 mg	peach, cloudy	85.4	18.1	78.8	17.2
B	CYS, 0.1 mmol	0.5 mL	Ru(PCy$_3$)$_2$Cl$_2$C$_7$H$_6$	pink	20 mg	yellow/orange	85.4	43.6	48.9	18.0
C	CYS, 20 mmol	0.5 mL	Ru(PCy$_3$)$_2$Cl$_2$C$_7$H$_6$	purple	20 mg	peach, cloudy	85.4	16.1	81.1	17.0
D	CYS, 10mmo	0.5 mL	Ru(PCy$_3$)$_2$Cl$_2$C$_7$H$_6$	purple	40 mg	peach, cloudy	85.4	17.6	79.4	19.2
E	CYS, 10 mmol	0.5 mL	Ru(PCy$_3$)$_2$Cl$_2$C$_7$H$_6$	purple	10 mg	peach, cloudy	85.4	19.2	77.5	18.4
F	MEA, 20 mmol	0.5 mL	Ru(PCy$_3$)$_2$Cl$_2$C$_7$H$_6$	brown	20 mg	peach	75.6	1.37	98.2	16.7
G	CYA, 20 mmol	0.5 mL	Ru(PCy$_3$)$_2$Cl$_2$C$_7$H$_6$	green	20 mg	brown grey	75.6	3.21	95.8	1.54
H	CYS, 20 mmol	0.5 mL	Ru(PCy$_3$)$_2$Cl$_2$C$_7$H$_6$	purple cloudy	20 mg	cloudy	75.6	18.3	75.8	12.7
I	CYS, 20 mmol	1.0 mL	Ru(PCy$_3$)$_2$Cl$_2$C$_7$H$_6$	purple	20 mg	cloudy colourless	75.6	18.8	75.1	29.6
J	CYS, 20 mmol	water, 1.0 mL	Ru(PCy$_3$)$_2$Cl$_2$C$_7$H$_6$	purple	20 mg	cloudy colourless	75.6	17.8	76.5	32.1
K	CYS, 20 mmol	0.5 mL	Ru(PCy$_3$)$_2$Cl$_2$C$_7$H$_6$	purple		pink	75.6	12.6	83.3	1.75
L	MEA, 20 mmol	0.5 mL	Pd(PPh$_3$)$_4$	orange	20 mg	faint yellow	135	0.648	99.5	34.8
M	CYA, 20 mmol	0.5 mL	Pd(PPh$_3$)$_4$	pale yellow	20 mg	faint yellow	135	13.8	90	3.84
N	CYS, 20 mmol	0.5 mL	Pd(PPh$_3$)$_4$	cloudy orange	20 mg	clear colourless	135	0.191	99.86	2.29
O	CYS, 20 mmol	1.0 mL	Pd(PPh$_3$)$_4$	yellow	20 mg	clear colourless	135	1.20	99.1	8.57
P	CYS, 20 mmol	water, 1.0 mL	Pd(PPh$_3$)$_4$	yellow	20 mg	clear colourless	135	0.0800	99.94	7.70
Q	CYS, 20 mmol	0.5 mL	Pd(PPh$_3$)$_4$	cloudy orange		clear colourless	135	0.0900	99.93	2.74
R	CYS, 20 mmol	1.0 mL	Pd(PPh$_3$)$_4$	yellow		clear colourless	135	0.0549	99.96	2.81

Table App. D-4: The roles of pH and functional groups

	Additive (20 mmol)	Base added	Metal source in 5.0 mL THF	Initial solution colour	Fe@Fe_xO_y	Final solution colour	Initial [M] (ppm)	Final [M] (ppm)	% Removed	Final [Fe] (ppm)
A	MEA	KOH, 0.2 mM, 0.5 mL	$Pd(PPh_3)_4$	orange	20 mg	pale yellow	138	0.537	99.6	24.6
B	MEA	water, 0.5 mL	$Pd(PPh_3)_4$	orange	20 mg	pale yellow	138	1.09	99.2	33
C	MEA	KOH, 0.2 mM, 0.5 mL	$Pd(PPh_3)_4$	orange		orange, orange ppt	138	74.2	46	2.66
D	CYA	KOH, 0.2 mM, 0.5 mL	$Pd(PPh_3)_4$	pale yellow	20 mg	yellow	138	12.5	91	3.32
E	CYA	water, 0.5 mL	$Pd(PPh_3)_4$	pale yellow	20 mg	pale yellow	138	13.5	90	3.46
F	CYA	KOH, 0.2 mM, 0.5 mL	$Pd(PPh_3)_4$	pale yellow		pale yellow, yellow ppt	138	19.6	86	3.06
G	LYS	KOH, 0.2 mM, 0.5 mL	$Pd(PPh_3)_4$	pale yellow	20 mg	pale yellow	138	26.5	81	2.86
H	LYS	water, 0.5 mL	$Pd(PPh_3)_4$	pale yellow	20 mg	pale yellow	138	13.4	90	2.82
I	LYS	KOH, 0.2 mM, 0.5 mL	$Pd(PPh_3)_4$	pale yellow		pale yellow	138	1.6	98.8	2.69
J	MEA	water, 0.5 mL	$Pd(PPh_3)_4$	orange	20 mg	pale yellow	134.5	2.23	98	22.8
K	MEA	KOH, 0.4 M, 0.5 mL	$Pd(PPh_3)_4$	yellow	20 mg	clear colourless	134.5	0.079	99.94	2.44
L	MEA	KOH, 0.8 M, 0.5 mL	$Pd(PPh_3)_4$	cloudy yellow	20 mg	pale yellow	134.5	0.941	99.3	3.12
M	CYA	water, 0.5 mL	$Pd(PPh_3)_4$	pale yellow	20 mg	pale yellow, orange oil	134.5	30.8	77	5.75
N	CYA	KOH, 0.4 M, 0.5 mL	$Pd(PPh_3)_4$	pale yellow	20 mg	very pale yellow	134.5	11.4	92	4.55
O	CYA	KOH, 0.8 M, 0.5 mL	$Pd(PPh_3)_4$	pale yellow	20 mg	very pale yellow	134.5	10.3	92	5.86
P	GLY	water, 0.5 mL	$Pd(PPh_3)_4$	very pale yellow	20 mg	brown	134.5	75.4	44	6.89
Q	GLY	KOH, 0.4 M, 0.5 mL	$Pd(PPh_3)_4$	yellow	20 mg	dark yellow	134.5	87.6	35	7.57
R	GLY	KOH, 0.8 M, 0.5 mL	$Pd(PPh_3)_4$	very pale yellow	20 mg	dark yellow	134.5	98.9	26	8.88
S	GLY	KOH, 0.2 mM, 0.5 mL	$Pd(PPh_3)_4$	very pale yellow	20 mg	brown	134.5	81.8	39	13.6
T	GLY	KOH, 0.2 mM, 0.5 mL	$Pd(PPh_3)_4$	very pale yellow		brown	134.5	77.0	43	14.6
U	GLY	KOH, 0.2 mM, 0.5 mL	$Pd(PPh_3)_4$	very pale yellow		pale yellow	134.5	53.6	60	13.2

Table App. D-5: The role of base and functional groups with Rh and Ru catalysts

	Additive (20 mmol)	Base added	Metal source in 5.0 mL THF	Initial solution colour	Fe@Fe$_x$O$_y$	Final solution colour	Initial [M] (ppm)	Final [M] (ppm)	% Removed	Final [Fe] (ppm)
A	MEA	KOH, 0.2 mM, 0.5 mL	Ru(PCy$_3$)$_2$Cl$_2$C$_7$H$_6$	orange	20mg	pale yellow	75.6	1.62	98	32.6
B	MEA	water, 0.5 mL	Ru(PCy$_3$)$_2$Cl$_2$C$_7$H$_6$	orange	20 mg	yellow	75.6	3.31	96	22
C	MEA	KOH, 0.2 mM, 0.5 mL	Ru(PCy$_3$)$_2$Cl$_2$C$_7$H$_6$	orange		dark orange	75.6	55.9	26	2.84
D	CYA	KOH, 0.2 mM, 0.5 mL	Ru(PCy$_3$)$_2$Cl$_2$C$_7$H$_6$	green	20 mg	cloudy orange	75.6	7.45	90	4.45
E	CYA	water, 0.5 mL	Ru(PCy$_3$)$_2$Cl$_2$C$_7$H$_6$	green	20 mg	cloudy orange	75.6	6.74	91	5.07
F	CYA	KOH, 0.2 mM, 0.5 mL	Ru(PCy$_3$)$_2$Cl$_2$C$_7$H$_6$	green		faint yellow	75.6	12.1	84	2.88
G	LYS	KOH, 0.2 mM, 0.5 mL	Ru(PCy$_3$)$_2$Cl$_2$C$_7$H$_6$	pale green	20 mg	orange	75.6	41.1	46	9.73
H	LYS	water, 0.5 mL	Ru(PCy$_3$)$_2$Cl$_2$C$_7$H$_6$	pale green	20 mg	orange	75.6	41.8	45	8.18
I	LYS	KOH, 0.2 mM, 0.5 mL	Ru(PCy$_3$)$_2$Cl$_2$C$_7$H$_6$	pale green		orange	75.6	35.6	2.8	2.69
J	MEA	KOH, 0.2 mM, 0.5 mL	Rh(PPh$_3$)$_3$Cl		20 mg		44.4	10.2	77	60.9
K	MEA	KOH, 0.4 M, 0.5 mL	Rh(PPh$_3$)$_3$Cl		20 mg		44.4	4.6	90	4.74
L	MEA	KOH, 0.2 mM, 0.5 mL	Rh(PPh$_3$)$_3$Cl				44.4	35	21	3.98
M	CYA	KOH, 0.2 mM, 0.5 mL	Rh(PPh$_3$)$_3$Cl		20 mg		44.4	30.4	32	16.1
N	CYA	KOH, 0.4 M, 0.5 mL	Rh(PPh$_3$)$_3$Cl		20 mg		44.4	20.8	53	5.97
O	CYA	KOH, 0.2 mM, 0.5 mL	Rh(PPh$_3$)$_3$Cl				44.4	35.1	21	4.32
P		KOH, 0.2 mM, 0.5 mL	Rh(PPh$_3$)$_3$Cl		20 mg		44.4	36.1	19	8.16

Table App. D-6: Sequestration with filtering agents

	Additive (20 mmol)	Base added (0.4 M)	Metal source in 5.0 mL THF	Initial solution colour	Filtering agent (20 mg)	Final solution colour	Initial [M] (ppm)	Final [M] (ppm)	% Removed	Final [Fe] (ppm)
A	CYA	0.5 mL	$Pd(PPh_3)_4$	yellow	Celite	pale yellow	144	34.1	76	1.28
B	CYA	0.5 mL	$Pd(PPh_3)_4$	yellow	Carbon Black	pale yellow	144	55.3	62	1.23
C	CYA	0.5 mL	$Ru(PCy_3)_2Cl_2C_7H_6$	brown	Celite	faint orange	71.3	17.9	75	1.27
D	CYA	0.5 mL	$Ru(PCy_3)_2Cl_2C_7H_6$	brown	Carbon Black	faint orange	71.3	16.2	77	1.14
E	CYA	0.5 mL	$Ru(PCy_3)_2Cl_2C_7H_6$	brown	$Fe@Fe_xO_y$	faint orange	71.3	25.6	64	4.65
F	MEA	0.5 mL	$Pd(PPh_3)_4$	orange	Celite	no colour	144	0.102	99.93	1.35
G	MEA	0.5 mL	$Pd(PPh_3)_4$	orange	Carbon Black	no colour	144	0.0758	99.95	1.40
H	MEA	0.5 mL	$Ru(PCy_3)_2Cl_2C_7H_6$	orange-brown	Celite	orange	71.3	14.6	80	1.33
I	MEA	0.5 mL	$Ru(PCy_3)_2Cl_2C_7H_6$	orange-brown	Carbon Black	orange	71.3	16.2	77	1.36
J	MEA	0.5 mL	$Ru(PCy_3)_2Cl_2C_7H_6$	orange-brown	$Fe@Fe_xO_y$	green	71.3	1.47	98	5.10